Dissertation

Study on Steering Mode Variation Control Methods for High Performance Four Single-Gimbal Control Moment Gyros

高性能4シングルジンバル コントロールモーメントジャイロ実現のための 駆動部変更制御法に関する研究

Shinya Kasai

Department of Aerospace Engineering

Graduate School of System Design

Tokyo Metropolitan University

Contents

List of Figures

List of Tables

Chapter 1

Introduction

1.1 Background

Satellite attitude control is crucial for smooth, effective execution of space missions. Thrusters, spin stabilization, momentum wheels, reaction wheels (RWs), control moment gyros (CMGs), solar sails, magnetic torques, gravity gradient stabilization, and other mechanisms have been designed for this purpose.

In spin stabilization, the satellite is rotated about one axis to generate a gyroscopic effect, stabilize the other two axes, and prevent attitude deviation. In a bias momentum mechanism such as a momentum wheel for three-axis stabilization, a large momentum wheel is rotated about one axis to obtain gyro rigidity for one axis without rotating the entire satellite, and a separate attitude control mechanism is then necessary for the other two axes. For three-axis attitude control in a satellite, it is therefore desirable to use a zero-momentum three-axis stabilization system. The most typical system of this type in satellites is thruster attitude control. Most systems of this type are monopropellant thrusters, in which the liquid propellant is released from a pressurized tank by a regulator valve and expelled via a nozzle, or fuel is sprayed from a pressurized tank onto a catalyst for decomposition followed by ejection from a nozzle, thus generating a reaction force on the satellite. As an alternative, attitude control may employ bipropellant thrusters, in

which the reaction product of fuel and an oxidizer are ejected from a nozzle. These fuel- and propellant-based thrusters can exert high torque, but the finite quantity of available fuel or propellant limits the number of times they can be fired without replenishment, and inevitably curtails missions involving their periodic firing where replenishment is difficult given the absence of gas stations in space.

Unlike thruster actuators, RWs, CMGs, and other angular momentum exchange actuators cannot induce translational motion and therefore cannot be used for orbit control. Even for rotational motion, their output torque is much smaller than that of thrusters. On the other hand, they are powered by electrical energy, which can be constantly replenished by generation from sunlight as long as the satellite's solar cell panels do not degrade or fail, making it possible for them to operate for years on end. This allows long-term satellite missions, and plays an essential role in achieving high satellite cost-performance.

A CMG generates torque by moving a gimbal about an axis perpendicular to the angular momentum vector of a flywheel rotating at a given speed. Both CMGs and RWs are angular exchange actuators, but a CMG can generate higher output torques than an RW because it uses separate motors for exchanging and maintaining angular momentum. CMGs can be classified into single-gimbal CMGs (SGCMGs) or double-gimbal CMGs (DGCMGs), based on the number of steering gimbals per gyro. By the turn of the century, many basic studies on SGCMGs [1–8] and DGSMGs [9–16] had shown that singularities presented a major problem for operational attitude control by both types of CMG systems. If a CMG system enters a state of singularity, the required torque can no longer be generated and attitude control fails. Various means of solving this problem have been considered. One, which is analogous to RW unloading, involves the use of different attitude control devices. The other is to increase the number of attitude control units, and thus increase the number of operating CMGs, until it is sufficient to prevent the occurrence of any singularities. It was found that the problem could be resolved by using six SGCMGs or four DGCMGS [17], and this solution was adopted for CMG operation on spacecraft with missions requiring high agility, such as the Hubble Space Telescope,

and on large space structures such as the International Space Station (ISS) and the MIR. For SGCMGs in particular, however, the large number required to avoid singularities in satellite attitude control translates to a significant reduction in the satellite's maximum payload capacity. Many studies have therefore focused on new methods of singularity avoidance in SGCMGs [18–25], and since the year 2000 or so, this has led to the proposal of new CMG system, based on variable-speed control moment gyros (VSCMGs), in which flywheel rotation can be varied as needed, in contrast to classical fixed-speed flywheels. VSCMGs therefore became a focus of interest for Prof. Schaub and his group, and many other researchers, and were the subject of many studies [26–32].

Research on CMGs began relatively late in Japan, with studies first by Kurokawa [33–35] and then by Omagari and Matunaga [36], Nanamori et al. [37, 38], Yamada et al. [39–42], Takada and Kojima [43], Takada et al. [44], Nanamori and Takahashi [45], and others, and have begun to yield important advances in concepts, methods and analysis. At present, however, organizations in other countries still retain a substantial lead over those in Japan with regard to CMG research. For Japan, as a late starter, the area of concentration that is most promising for research and development with respect to CMG technology in the time ahead is SGCMG attitude-control systems, for two following reasons. The first is the higher level of torque that can be generated by SGCMGs than by DGCMGs such as those on the ISS, due to the absence of torque loss in an outer or inner gimbal. The second is the lower complexity and weight of a four-SGCMG array than a four DBCMG array, which can avoid singularities and other problems and thus provide high stability, but at the cost of a substantial increase in mechanism complexity and weight.

However, with a focus on attitude control using SGCMGs, simply increasing the number of SGCMGs in the array to a level sufficient to render the singularity problem negligible would increase the weight of the array and thus lower the maximum payload capacity of the satellite.

It is therefore desirable to obtain reliable three-axis satellite attitude control with the smallest possible number of SGCMGs. Placing each of four SGCMGs at an angle of

54.73 deg from the apex of a common pyramid results in a spherical envelope of maximum angular momentum for the CMG system, thereby maintaining three-dimensional angular momentum isotropy, and is therefore desirable for the three-axis attitude control system. This configuration of four SGCMGs in a pyramidal array (a 4-SGCMG pyramid array) can provide the high torque needed for rapid changes in attitude with a relatively small number of CMGs in large satellites, while reducing system weight and yielding a corresponding increase in satellite payload capacity. The increase in payload capacity represents an increase in the permissible range of size and weight of onboard observational instruments and other equipment, and thus in their capabilities and functionality. The 4-SGCMG pyramid-array configuration therefore holds the potential to enable missions with large instrument payloads requiring high agility, and can play a key role in the advancement of space exploration and development.

Another subject of growing interest in recent years is the H_∞ (robust) control theory that was developed and finalized in the 1980s by Francis [46], Glover and Doyle [47], Doyle et al. [48], and others, and its application to CMGs [49–51]. Until its advent, modern control theory had simply presumed precise models, and thus precluded guarantees relating to model error. With H_∞ control, it became possible to guarantee control performance even if the model was not precisely identified. It has now become a focus of interest as a practical robust-control theory. Beginning in the 1990s, many studies have emerged on both linear H_∞ [52–55] control and nonlinear [56–59] H_∞ control, and its application to CMGs may lead to new advances in control performance.

Vibration control is also crucial. Studies drawing on the findings of longstanding research on attitude control in satellites with flexible structures [60–63] have recently focused on the application of CMGs to vibration control in flexible structures [64–66] and related considerations. Extension of this research to four-gimbal CMG pyramid arrays can be expected to open the way for important new advances in space exploration and development.

1.2 Related Studies

1.2.1 Studies on singularities

Wie's research group proposed a gimbal steering control law for a singularity-robust method of resolving the singularity problem [20–23]. It avoids states of singularity by imposing a small torque error on the control torque whenever the current state is near a singularity until the state has escaped from that region. Schaub and Junkins [24] and MacMahon and Schaub [25] proposed a local-gradient method based on a null-motion gimbal steering control law to resolve the singularity problem. To avoid states of singularity, it determines the appropriate gimbal steering for diversion from singularities without generating torque, based on the gradient of a local evaluation function. Both are excellent methods for singularity avoidance, and these studies have formed a major foundation for more recent research on the singularity problem in SGCMGs [67–69].

1.2.2 CMG steering mechanism

Two-SGCMG steering

Past studies [70–77] on RWs concerning the two-torque problem in three-RW systems showed that if one of the three RWs failed, attitude control could still be accomplished using just the two torques of the remaining RWs. For four-SGCMG systems, moreover, Kwon et al. considered the two-torque problem with just two normally steering CMGs, and investigated the performance of three-axis control using two of four parallel GMGs [78].

Variable-speed CMGs

McMahon and Schaub studied pyramid arrays of four variable-speed SGCMGs (VS-SGCMGs) [25], proposed a steering control law that transitioned from a CMG mode to an RW mode to avoid singularities and return to the target state more quickly than classical CMGs, and showed the effectiveness of this steering control law using numerical

simulations.

Yoon and Tsiotras studied VSCMGs [28, 32] with power tracking [79]. The power tracking method is based a form of energy recycling with a variable flywheel, in which excess power is used to increase the RW rotational speed and thus store energy, which is then released when power is insufficient.

Scissored-pair CMGs

Steyn investigated a control law for transition between CMG and RW systems using scissored-pair CMGs [80], and proposed a gimbal steering law for control that attains the target state in near-minimum time by transition between a CMG system that outputs a large torque and an RW system that outputs a small torque in accordance with the circumstances.

1.2.3 H_∞ control for CMGs and vibration control

Yamamoto and Shimomura studied H_∞ control of an RW system using a linear parameter-varying (LPV) model [49], used that study as the basis for a study [51] on H_∞ control of a variable-speed DGCMG again using an LPV model, and performed numerical simulation that showed the proposed controller was superior to existing controllers based on Lyapunov functions.

Abbas et al. [48] conducted a study on a controller with H_∞ control using an LPV model for a DGCMG(s), and showed experimentally that the proposed LPV controller was superior to existing linear time-invariant controllers.

Ford and Hall [64] conducted a study on vibration control with three SGCGMs, proposed a controller based on Lyapunov functions for this purpose, and showed its effectiveness by numerical simulations.

Edo et al. [65, 66] performed studies on active vibration control for hung structures with a double-gimbal CMG, constructed a multi-input multi-output control system using H_2/H_∞ control by H_2 control and LMI optimization, proposed a DGCMG controller,

and showed its effectiveness experimentally.

1.2.4 Problems with prior results and research objectives of this study

This subsection describes three problems to resolve for application of the results of prior studies to advancement of 4-SGCMG pyramid-array systems technology in Japan, together with the research objectives of the present study.

Increasing the fault tolerance of CMG systems

CMGs can output higher torque than RWs because separate motors are used for exchange and maintenance of the CMG angular momentum. This means, however, that more mechanical parts are required in CMG systems than in RW systems, which in turn means there are more sites of potential failure. If a CMG component fails in space it cannot be immediately repaired and its role in the mission would be finished. CMG failure is a high-risk event that may directly lead to mission failure. For a pyramid array of four SGCMGs as the minimum number required for stable three-axis attitude control, it is therefore essential to provide for cases in which not all four are functioning normally.

Kwon et al. [78] investigated three-axis control using two parallel CMGs in a 4-SGCMG array, but no studies have been reported on three-axis attitude control using two CMGs that are in a pyramid array and therefore cannot provide direct torque output in a single axial direction.

Further increasing high-torque output to reach target attitude in minimum time

The singularity-robust [20–23] and null motion-based local-gradient [24,25] methods, as described above, can both provide effective singularity avoidance and therefore may be considered for application to the 4-SGCMG pyramid-array configuration, in which the CMG singularity problem must always be confronted. Neither of these methods, however,

is conducive to attaining the target state in the minimum time. In the singularity-robust method, the need for continuous generation of the perturbation torque in order to avoid a singularity state in effect excludes application of a control torque for direct attainment of the target state and thereby tends to prevent its attainment in the minimum time. The local-gradient method based on null motion harbors the risk of entry into an even graver singularity state if the gimbal steering itself is controlled by the gradient method. For Japan, as a latecomer, the imperative in CMG technology advancement is to develop a gimbal steering control method for 4-SGCMG pyramid-array systems that resolves these problems and enables minimum-time target attainment while ensuring singularity avoidance, rather than continuing to focus on the proposal of explicit methods for singularity-avoidance gimbal steering control.

In contrast to classical CMGs, in which the skew angle is fixed at 54.73 deg in order to obtain a spherical angular-momentum envelope and thus facilitate three-dimensionally isotropic angular momentum, the variable skew angle of adaptive-skew CMGs (ASCMGs) enables departure from the spherical envelope by its expansion or contraction in the desired direction, so as to obtain high output torque and rapid attitude control. In this sense, ASCMG systems may be regarded as intermediate between SGCMG and DGCMG systems. The greatest advantage of ASCMG systems is that they can generate torque that is higher than previously possible with essentially the same components as classical fixed-skew angle CMG systems simply by incorporating a variable steering unit, with no need to adopt high-performance motors or raise the maximum gimbal angular velocity to increase flywheel angular momentum.

To bring ASCMG systems to reality, it will be necessary to design appropriate mechanisms and steering control laws that address the limitations specific to those systems.

Vibration control for flexible structures

With the achievement of high output torque, thus resolving the second of the three problems, the 4-SGCMG pyramid array will become capable of providing attitude control in larger-scale spacecraft, and vibration control, which is the third problem, will then

take on new importance. With increasing satellite size, the flexible component structures increase in weight and number. Excitation of vibration in these structures by attitude control maneuvers would then become too substantial to be disregarded, and effective vibration control is therefore essential.

A 4-SGCMG pyramid array composed of single-gimbal VSCMGs, in which constant-speed SGCMG flywheels have been converted to variable-speed flywheels, may be used for this purpose. Unlike the use of a variable-speed flywheel for energy recovery as proposed by Yoon and Tsiotras [79] or for singularity avoidance as proposed by McMahon and Schaub [25], the VSCMGs in this pyramid array enable its use as a classical CMG system capable of high torque output when distant from the target state and as an RW system with low torque output when near the target state, with a gimbal steering law that selects the degree of output torque in accordance with the relevant conditions. Simply using VSCMGs for the four SGCMGs in the pyramid array, however, will not in itself enable effective control of vibration of the satellite's flexible structures. It will also be necessary to formulate the relevant properties of these structures, design the controller on that basis, determine the extent of vibrational modes to be targeted, and guarantee a level of robustness with that degree of control. In all of this, the performance in regard to attaining the target satellite attitude must be borne in mind. This requires not only VSCMG control and but also the design of a controller that can determine the command torque that simultaneously meets multiple control objectives. A controller design incorporating H_∞ control theory is therefore desirable.

The studies noted until now that are relevant to this objective include those by Prof. Shimomura and his group [49, 51] and Abbas et al. [50] for the design of controllers using H_∞ control theory for CMG systems that do not address the question of flexible structures, and by Ford and Hall [64] for vibration control using three SGCMGs with a controller based on Lyapunov functions. The previously noted studies by Edo et al. [65, 66] on controller design incorporate H_∞ control theory for one-DGCMG systems that include consideration of flexible structures, rather than for control of the 4-SGCMG pyramid arrays that are the focus of the present research. In short, no prior studies have

considered a 4-SGCMG pyramid array composed of VSCMGs that incorporates H_∞ control theory for vibration control.

1.3 Research Objectives

The objectives of this research are to establish a method of CMG system control that varies the control components of a 4-SGCMG pyramid-array system, and to achieve the concomitant objectives of designing the following three control laws to resolve the three problems considered particularly important at the present stage of 4-SGCMG system development. The design of these laws and the effectiveness of the control law for transition between control components are described in this dissertation.

- A steering control law for a 4-SGCMG pyramid-array system that enables three-axis attitude control with just two of its opposing CMGs and thereby increasing its fault tolerance.

- A steering control law for ASCMGs, in which the skew angle is variable, to achieve a shorter time to settling and stabilization at the target attitude in comparison with classical fixed-skew CMGs.

- A steering control law incorporating H_∞ control theory for a VSCMG pyramid array with variable wheel speed, that includes consideration of uncertainty in wheel speed variation and vibration of flexible structures, allowing this SCMG system to provide effective vibration control for large flexible space structures.

1.4 Thesis Organization

Achievement of the research objectives is described in the following order.

Chapter 2 Spacecraft Attitude Maneuver using Two Single-Gimbal Control Moment Gyros

This chapter describes the achievement of increased fault tolerance in the 4-SGCMG pyramid-array system through solution of the two-torque problem using CMGs with variable gimbal angles in the steering component. A gimbal steering control law is also proposed for three-axis control by two of the four pyramid-array CMGs, as illustrated by the case of failure in the other two CMGs, and the effectiveness of the control law is verified by numerical simulations.

Chapter 3 Gain-Scheduled Steering Control Law for Adaptive Skew Pyramid-type CMG

Chapter 3 describes the achievement of a further increase in torque output in the 4-SGCMG pyramid-array system for attainment of the target state in the minimum time through adoption of a variable skew angle, rather than the fixed skew angle of classical configurations. This enables expansion or contraction of the angular momentum envelope in the desired direction. In addition, a gimbal/skew steering control law is proposed that considers the skew angle as part of the steering unit to obtain CMGs capable of high output torque, and its validity is verified by numerical simulations.

Chapter 4 LMI-based Control Law for Variable-Speed Control Moment Gyros in Flexible Spacecraft

Chapter 4 describes the control of vibration-inducing excitation of flexible structures by the high-torque output of the 4-SGCMG pyramid-array system. A gimbal-wheel steering control law is proposed for selection between high and low torque output in accordance with the relevant conditions. The adoption of high-torque CMGs as attitude-control devices for large spacecraft is considered through incorporation of variable-speed rather than fixed-speed flywheels in the steering unit. In addition, an LMI-based controller is proposed to provide a torque command satisfying the performance requirements for both attitude control and vibration. The effectiveness of the proposed steering control law and controller is verified by numerical simulations.

Chapter 5 Conclusions Chapter 5 summarizes the research efforts and the results obtained.

In summary, the present chapter outlines the context of the research presented in this dissertation in terms of past progress in satellite attitude control methods and then considers the attitude control mechanisms proposed here for operation of the large satellites that will be required for further advances in space exploration, the need for CMGs that function as angular momentum exchange actuators, the problems remaining to be solved. It also describes the overall organization of this dissertation.

References

[1] Margulies, G., Aubrun, J. N. :Geometric Theory of Single-Gimbal Control Moment Gyro System, *Journal of the Astronautical Sciences*, **26**(1978), pp.159-191.

[2] Bedrossian, N. S., Paradiso, J., Bergmann, E. V., Rowell, D. :Steering Law Design for Redundant Single-Gimbal Control Moment Gyroscopes, *Journal of Guidance, Control and Dynamics*, **13**(1990), pp.1083-1089.

[3] Bedrossian, N. S., Paradiso, J., Bergmann, E. V., Rowell, D. :Redundant Single Gimbal Control Moment Gyroscope Singularity Analysis, *Journal of Guidance, Control and Dynamics*, **13**(1990), pp.1096-1101.

[4] Vadali, S. R., Oh, H. S., Walker, S. R. :Preferred Gimbal Angles for Single Gimbal Control Moment Gyros, *Journal of Guidance, Control, and Dynamics*, **13**(1990), pp.1090-1095.

[5] Oh, H. S., Vadali, S. R. :Feedback Control and Steering Laws for Spacecraft using Single Gimbal Control Moment Gyros, *Journal of the Astronautical Sciences*, **39**(1991), pp 183-203.

[6] Paradiso, J. A. :Global Steering of Single Gimbaled Control Moment Gyroscopes using a Directed Search, *Journal of Guidance, Control and Dynamics*, **15**(1992), pp.1236-1244.

[7] Hoelscher, Brian R., Vadali, Srinivas R. :Optimal Open-Loop and Feedback Control using Single Gimbal Control Moment Gyroscopes, *Journal of the Astronautical Sciences*, **42**(1994), pp.189-206.

[8] Vadali, S.R., Krishnan, S. :Suboptimal Command Generation for Control Moment Gyroscopes and Feedback Control of Spacecraft, *Journal of Guidance, Control, and Dynamics*, **18**(1995), pp. 1350-1354.

[9] Kennel, H. F. :Steering Law for Parallel Mounted Double-gimbaled Control Moment Gyros, NASA TM-X-64930, 1975.

[10] Colburn, B.K., White, L. R. :Computational Considerations for a Spacecraft Attitude Control System Employing Control Moment Gyro, *Journal of Spacecraft*, **14**(1977), pp.40-53.

[11] Kennel, H. F. :Steering Law for Parallel Mounted Double-gimbaled Control Moment Gyros Revision A, NASA TM-82390, 1981.

[12] Kennel, H. F. :Torque Command Steering Law for Double-gimbaled Control Moment Gyros Applied to Rotor Energy Storage, NASA Conference Publication, 1984, pp.407-426.

[13] Goldie, J. H., Avakian, K. M., Downer, J. R., Gondhalekar, V., Johnson, B. G. :Experimental Evaluation of a High Performance Superconducting Torquer, Proceedings of the Intersociety Energy Conversion Engineering Conference, Vol.4, 1991, pp.227-232.

[14] Boyarski, S., Ben-Asher, J. Z. :Minimum-time Reorientation of a Two-degree-of-freedom Gyroscope, *Journal of Guidance, Control, and Dynamics*, **18**(1995), pp.782-791.

[15] Bauer, R. J. :Kinematics and Dynamics of a Double-gimbaled Control Moment Gyroscope, Mechanism and Machine Theory, **37**(2002), pp.1513-1529.

[16] Ahmed, J., Bernstein, D. S. :Adaptive Control of Double-gimbal Control-moment Gyro with Unbalanced Rotor, *Journal of Guidance, Control, and Dynamics*, **25**(2002), pp. 105-115.

[17] Tokar, E. N., Platonov, V. N. :Singular Surfaces in Unsupported Gyrodyne System, Kosmicheskie Issledovaniya, **16**(1978), pp.675-685.

[18] Ford, K. A. and Hall, C. D. :Singular Direction Avoidance Steering for Control-moment Gyros, *Journal of Guidance, Control, and Dynamics*, **23**(2000), pp.648-656.

[19] Yoon, H. and Tsiotras, P. :Singularity Analysis and Avoidance of Variable-speed Control Moment Gyros, *Journal of Guidance, Control, and Dynamics*, **27**(2004), pp.374-386.

[20] Heiberg, C. J., Bailey, D., Wie, B. :Precision Spacecraft Pointing using Single-gimbal Control Moment Gyroscopes with Disturbance, *Journal of Guidance, Control, and Dynamics*, **23**(2000), pp. 77-85.

[21] Wie, B., Bailey, D., and Heiberg, C. J. :Singularity Robust Steering Logic for Redundant Single-gimbal Control Moment Gyros, *Journal of Guidance, Control, and Dynamics*, **24**(2001), pp.865-872.

[22] Wie, B. :Singularity Analysis and Visualization for Single-gimbal Control Moment Gyros Systems, *Journal of Guidance, Control, and Dynamics*, **27**(2004), pp.271-282.

[23] Wie, B. :Singularity Escape/Avoidance Steering Logic for Control Moment Gyro Systems, *Journal of Guidance, Control, and Dynamics*, **28**(2005), pp.948-956.

[24] Schaub, H. and Junkins, J. L. :Singularity Avoidance using Null Motion and Variable-speed Control Moment Gyros, *Journal of Guidance Control, and Dynamics*, **23**(2000), pp.11-16.

[25] McMahon, J. and Schaub, H. :Simplified Singularity Avoidance using Variable-speed Control Moment Gyroscope Null Motion, *Journal of Guidance, Control, and Dynamics*, **32**(2009), pp.1938-1943.

[26] Schaub, H., Vadali, S. R., Junkins, J. L. :Feedback Control Law for Variable Speed Control Moment Gyros, *Journal of the Astronautical Sciences*, **46**(1998), pp. 307-328.

[27] Fausz, J. L., Richie, D. J. :Flywheel Simultaneous Attitude Control and Energy Storage using a VSCMG Configuration, IEEE Conference on Control Applications Proceedings, Vol.1, 2000, pp.991-995.

[28] Yoon, H. and Tsiotras, P. :Spacecraft Adaptive Attitude and Power Tracking with Variable Speed Control Moment Gyro-scopes, *Journal of Guidance, Control, and Dynamics*, **25**(2002), pp.1081-1090.

[29] Romano, M., Agrawal, B. N. :Use of Variable Speed Control Moment Gyros for a Fine Pointing Dual Line-of-sight Spacecraft, *Advances in the Astronautical Sciences*, **113**(2003), pp.377-382.

[30] Agrawal, B. N., Romano, M., Martinez, T. :Three-axis Attitude Control Simulators for Bifocal Relay Mirror Spacecraft, *Advances in the Astronautical Sciences*, bf 115(2003), pp.168-181.

[31] Romano, M., Agrawal, B. N. :Attitude Dynamics/Control of Dual-body Spacecraft with Variable-speed Control Moment Gyros, *Journal of Guidance, Control, and Dynamics*, **27**(2004), pp.513-525.

[32] Yoon, H. and Tsiotras, P. :Spacecraft Line-of-sight Control using a Single Variable-speed Control Moment Gyro, *Journal of Guidance, Control, and Dynamics*, **29**(2006), pp.1295-1308.

[33] Kurokawa, H. :Constrained Steering Law of Pyramid-type Control Moment Gyros and Ground Tests, *Journal of Guidance, Control, and Dynamics*, **20**(1997), pp.445-449.

[34] Kurokawa, H. :A Geometric Study of Single Gimbal Control Moment Gyros Singularity Problems and Steering Law, Tech. Rep. Report, Mechanical Engineering Laboratory, Japan, No.175, 1998.

[35] Kurokawa, H. :Survey of Theory and Steering Laws of Single-gimbal Control Moment Gyros, *Journal of Guidance, Control, and Dynamics*, **30**(2007), pp.1331-1340.

[36] Omagari, K., Matunaga, S. :Micro Gravity Experiment of Variable Speed Control Moment Gyro at MG-LAB, Collection of Technical Papers - AIAA/AAS Astrodynamics Specialist Conference, **2**(2006), pp.1415-1424.

[37] Nanamori, Y., Takahashi, M., Taniwaki, S., Yoshida, K., and Ohkami, Y. :High Accuracy Multi Target Pointing Steering Law of Earth Observation Satellite using Variable-speed Control Moment Gyros, Proceeding of Dynamics and Design Conference, No.411, 2007, pp.1-6.

[38] Nanamori, Y., Takahashi, M., Taniwaki, S., Yoshida, K., Ohkami, Y. :Singularity Avoidance of Control Moment Gyros using Optimization of Initial Gimbal Angles and Application to Multi Target Pointing for Satellite Attitude Control, *Advances in the Astronautical Sciences*, **129**(2008), pp.2337-2352.

[39] Yamada, K., Takatsuka, N., Shima, T. :Spacecraft Pointing Control using a Variable-speed Control Moment Gyro, *Transactions of the Japan Society for Aeronautical and Space Sciences, Space Technology Japan*, **7**(2009), pp.Pd_1-Pd_6.

[40] Yamada, K., Takatsuka, N., Shima, T. :Spacecraft Pointing Control using a Double-gimbal Control Moment Gyro, *Transactions of the Japan Society for Aeronautical and Space Sciences, Space Technology Japan*, **8**(2011), pp.Pd_45-Pd_52.

[41] Yamada, K., Jikuya, I., Kwak, O. :Rate Damping of a Spacecraft using Two Single-gimbal Control Moment Gyros, *Journal of Guidance, Control, and Dynamics*, **36**(2013), pp.1606-1623.

[42] Yamada, K., Jikuya, I. :Directional Passability and Quadratic Steering Logic for Pyramid-type Single Gimbal Control Moment Gyros, *Acta Astronautica*, **102**(2014), pp.103-123.

[43] Takada, K. and Kojima, H. :Receding Horizon Control on Steering of Control Moment Gyro for Fast Attitude Maneuver, *Transactions of the Japan Society for Aeronautical and Space Sciences*, **52**(2009), pp.1-10.

[44] Takada, K., Kojima, H. and Matsuda, N. :Control Moment Gyro Singularity-avoidance Steering Control Based on Singular-surface Cost Function, *Journal of Guidance, Control, and Dynamics*, **33**(2010), pp.1442-1450.

[45] Nanamori, Y.and Takahashi, M. :Steering Law of Control Moment Gyros using Optimization of Initial Gimbal Angles for Satellite Attitude Control, *Journal of System Design and Dynamics*, **5**(2011), pp.30-41.

[46] Francis, A. B. :A Couse in H_∞ Control Theory, Springer, 1987.

[47] Glover, K., and Doyle, C. J. :State-space Formulae for All Stabilizing Controllers that Satisfy an H_∞ - Norm Bound and Relations to Risk Sensitivity, *Systems and Control Letters*, **11**(1988), pp.167-172.

[48] Doyle, C. J., Glover, K., Khargonekar, P. P., Francis, A. B. :State-space Solutions to Standard H_2 and H_∞ Control Problems, Proc.1988 American Control Conference, Atlanta, *IEEE Trans. on Automatic Control*, **34**(1989), pp.831-847.

[49] Yamamoto, Y. and Shimomura, T. :Attitude Control of Spacecraft through a Simple LPV Model with a Virtual State Variable, AIAA Guidance, Navigation, and Control Conference, AIAA Paper 2012-5005, 2012.

[50] Abbas, S. H., Ali, A., Hashemi, M. S., Werner, H. :LPV Gain-scheduled Control of a Control Moment Gyroscope, 2013 American Control Conference, Washington, DC, USA, June 17-19, 2013.

[51] Sasaki, T., Sakuramata, N., Shimomura, T. :Attitude Control of a Spacecraft with a DGVSCMG via LPV Control Theory, *Journal of the Japan Society for Aeronautical and Space Sciences*, **63**(2015), pp.77-82.

[52] Sampei, M., Mita, T., and Nakamichi, M. :An Algebraic Approach to H_∞ Output Feedback Control Problems, *Systems & Control Letters*, **14**(1990), pp.13-24.

[53] Doyle, C. J., Francis, A. B., Tannenbaum, R. A. :Feedback Control Theory, Macmillan, 1992.

[54] Zhou, K., Doyle, C. J., Glover, K. :Robust and Optimal Control, Prentice Hall, 1996

[55] Apkarian, P., Gahinet, P. :A Convex Characterization of Gain-scheduled H_∞ Controllers, *IEEE Transactions on Automatic Control*, **40**(1995), pp.853-864.

[56] Van der Schaft, A. J. :L_2-gain and Passivity Techniques in Nonlinear Control, Springer-Verlag, 1996.

[57] Wei-Mi Lu., and Doyle, C. J. :H_∞ Control of Non-linear SystemsH_∞ A Convex Characterization, Proc. American control Conference, 1994, pp.2098-2012.

[58] Patpong, L., Sampei, M., Koga, M., Shimuzu, E. :A Numerical Computational Approach of Hamilton-Jacobi-Isaacs Equation in Nonlinear H_∞ Control Problems, 35th Conference on Decision and Control, 1996, pp.3774-3779.

[59] Ohsaku S., Nakayama T., Kamimura I., Motozono, Y. :Nonlinear H_∞ State Feedback Controller for Semi-active Controlled Suspension, Proceedings of AVEC ' 98, 1998, pp. 63-68.

[60] Ohkami, A., Fujii, H. :Dynamic Modeling of Flexible Spacecraft Hybrid System and Truncation, *Transactions of the Japan Society for Aeronautical and Space Sciences*, **32**(1984), pp.263-274.

[61] Ohkami, A., Kida, T., Yamaguchi, I. :Dynamics, Modeling and Order Reduction of LSS, *Transactions of The Society of Instrument and Control Engineers*, **26**(1987), pp.845-854.

[62] Tsuchiya, K., Kashiwase, T. :Control of Large Space Structures, *Transactions of The Society of Instrument and Control Engineers*, **26**(1987), pp.855-862.

[63] Kida, T., Yamaguchi, I., Ikeda, M. :LSS Attitude Control Experiment – Application of LQ Loop-shaping Capability –, *Society of Instrument and Control Engineers Journal*, **28**(1992), pp.107-115.

[64] Ford, K. A., Hall, C. D. :Flexible Spacecraft Reorientations using Gimbaled Momentum Wheels, *Journal of the Astronautical Sciences*, **49**(2002), pp.421-441.

[65] Edo, K., Kanki, H., Kawanishi, M. :Active Jiggle Control for Hung Structure using Double Gimbals CMG, *Journal of the Japan Society of Mechanical Engineers*, **66**(2000), pp.3289-3296.

[66] Edo, K., Kanki, H., Kawanishi, M., Kagawa, R. :Dynamical Characteristics Analysis of Double Gimbal CMG and its Application to Vibration Control, *Journal of the Japan Society of Mechanical Engineers*, **67**(2001), pp.110-117.

[67] Leeghim, H., Bang, H., Park, J.-O. :Singularity Avoidance of Control Moment Gyros by One-step Ahead Singularity Index, *Acta Astronautica*, **64**(2009), pp.935-945.

[68] Kojima, H. :Singularity Analysis and Steering Control Laws for Adaptive-skew Pyramid-type Control Moment Gyros, *Acta Astronautica*, **85**(2013), pp.120-137.

[69] Kojima, H. :Calculation and Fitting of Boundaries between Elliptic and Hyperbolic Singularities of Pyramid-type Control Moment Gyros, *Acta Astronautica*, **101**(2014), pp.33-44.

[70] Brockett, R. W. :Asymptotic Stability and Feedback Stabilization, *Differential Geometric Control theory*, **27**(1983), pp.181-208.

[71] Crouch, P. E. :Spacecraft Attitude Control and StabilizationH_∞ Application of Geometric Control Theory to Rigid Body Model, *IEEE Transactions on Automatic Control*, **29**(1984), pp.321-331.

[72] Krishnan, H., McClamroch, Harris, N., Reyhanoglu, M. :Attitude Stabilization of a Rigid Spacecraft using Two Momentum Wheel Actuators, *Journal of Guidance, Control, and Dynamics*, **18**(1995), pp. 256-263.

[73] Morin, P., Samson, C., Pomet, J. B., Jiang, Z. P. :Time-varying Feedback Stabilization of the Attitude of a Rigid Spacecraft with Two Controls, *Systems & Control Letters*, **25**(1995), pp.375-385.

[74] Tsiotras, P. :Stabilization and Optimality Results for the Attitude Control Problem, *Journal of Guidance, Control, and Dynamics*, **19**(1996), pp.772-779

[75] Morin, P., Samson, C. :Time-varying Exponential Stabilization of a Rigid Spacecraft with Two Control Torques, *IEEE Transactions on Automatic Control*, **42**(1997), pp. 528-534.

[76] Yamada, K. and Yoshikawa, S. :Space Attitude Control using Two Reaction Wheels, *Transactions of the Society of Instrument and Control Engineers*, **34**(1998), pp.34-40.

[77] Kojima, H. :Stabilization of Angular Velocity of Asymmetrical Rigid Spacecraft using Two Constant Torques, *Journal of Guidance, Control, and Dynamics*, **30**(2007), pp.1163-1168.

[78] Kwon, S., Shimomura, T., Okubo,H. :Pointing Control of Spacecraft using Two SGCMGs via LPV Control Theory, *Acta Astronautica*, **68**(2011), pp.1168-1175.

[79] Tsiotras, P., Shen, H., Hall, C. :Satellite Attitude Control and Power Tracking with Energy/Momentum Wheels, *Journal of Guidance, Control, and Dynamics*, **24**(2001), pp. 23-34.

[80] Steyn, W. H. :A Dual-wheel Multi-mode Spacecraft Actuator for Near-minimum-time Large Angle Slew Maneuvers, *Aerospace Science and Technology*, **12**(2008), pp.545-554.

Chapter 2

Spacecraft Attitude Maneuver using Two Single-Gimbal Control Moment Gyros

In this chapter, arbitrary rest-to-rest attitude maneuver problems for a satellite using two single-gimbal control moment gyros (2SGCMGs) are considered. Although single-gimbal control moment gyros are configured in the same manner as the traditional pyramid-array CMG, only two CMGs are assumed to be available. Attitude maneuver problems are similar to problems involving two reaction wheels (RWs) from the viewpoint of the number of actuators. In other words, the problem treated herein is a kind of underactuated problem. Although 2SGCMGs can generate torques around all axes, they cannot generate torques around each axis independently. Therefore, control methods designed for a satellite using two reaction wheels cannot be applied to 3-axis attitude maneuver problems for a satellite using 2SGCMGs. In this chapter, for simplicity, maneuvers around the x and z axes are first considered, and then a maneuver around the y axis due to the corning effect resulting from the maneuver around the x and z axes is considered. Since maneuvers around each axis are established by the proposed method, arbitrary attitude maneuvers can be achieved using 2SGCMGs. In

addition, the maneuvering angles around the z and x axes, which are required in order to maneuver around the y axis, are analytically determined, and the total time required for maneuvering around the y axis is then analyzed numerically.

Nomenclature

$\boldsymbol{C}$	=	Jacobian matrix of the CMG system associated with the gimbal angles
$\boldsymbol{g}_i$	=	the i^{th} gimbal axis vector
$\boldsymbol{h}$	=	angular momentum vector of the CMG
$\boldsymbol{h}_s$	=	singular momentum vector of the CMG
H	=	angular momentum magnitude of the CMG, Nms
$\boldsymbol{H}_i$	=	angular momentum vector of the i^{th} CMG
J_x, J_z	=	moments of inertia about the x and z axes, respectively
$\boldsymbol{u}_s$	=	singular vector
xyz	=	satellite body frame
XYZ	=	CMG system reference frame
β	=	skew angle = 54.73 deg
$\boldsymbol{\delta}$	=	gimbal angle vector $(= (\delta_1, \delta_2, \delta_3, \delta_4)^T)$
δ_i	=	gimbal angle of the i^{th} CMG
ε_i	=	the i^{th} signum of the singular surface
τ_x, τ_y, τ_z	=	attitude control torque vector generated by the CMGs
ϕ, θ, ψ	=	roll, pitch, yaw Euler angle

2.1 Introduction

Control moment gyros (CMGs) are momentum-exchange torque generators, which are often used on large spacecraft, such as MIR, Skylab, and ISS, because these systems have the advantages of high torque output and rapid response compared to reaction

wheels (RWs). Control moment gyro systems can be classified into two types based on the number of degrees of freedom for each CMG: single-gimbal CMGs (SGCMGs) and double-gimbal CMGs (DGCMGs). DGCMGs are mechanically more complex than SGCMGs, but the additional gimbal can be used to produce torque more easily. SGCMG systems are mechanically simpler than DGCMGs, but producing torque around an arbitrary direction requires at least three SGCMGs. There are several CMG array configurations. The pyramid-array CMG system is a typical configuration. Even though more than three SGCMGs are used, SGCMG systems have a more critical singularity problem than DGCMG systems. The angular momentum of pyramid-array CMG systems in the singularity state was studied in [1], and a number of control schemes have been proposed [2–15] to overcome the singularity problem of SGCMGs.

On the other hand, methods by which to stabilize the angular velocity and/or the three-axis attitude of a spacecraft using less than three controls have been widely studied [16–20]. This is a kind of underactuated control problem, and is well known as a two-control torque problem. From Brockett's theorem [18], no smooth time invariant control methods exist for this problem, and time-varying or non-smooth control methods have been proposed. In the two-control torque problem, it is usually assumed that two independent thrusters, or two RWs, are used for attitude control. However, only a few studies have been carried out that assume the use of fewer than three single-gimbal CMGs for attitude control. Kwon et al. [21] have studied a pointing control problem using two single-gimbal CMGs, in which the gimbal axes of the two SCMGs are paralled to the z axis of the body frame.

From the viewpoint of fault tolerance, it is desirable to develop a backup control method as a redundancy against the failure of CMG units. In this chapter, arbitrary rest-to-rest attitude maneuver problems for a satellite using two single-gimbal control moment gyros (2SGCMGs) are considered under the assumptions that SGCMGs are configured in the same manner as the traditional pyramid-array CMGs, but that only two diagonal CMGs are available. Although 2SGCMGs in the pyramid array can generate torques around all axes, they cannot generate torques around each axis independently.

In this chapter, for simplicity, assuming that the CMG reference frame is coincident with the satellite body frame and the moment of inertia tensor for the satellite is diagonal, maneuvers around the x and z axes of the satellite body frame are first considered, and based on the resulting corning effect, maneuvering around the y axis of the satellite body frame is then evaluated. In addition, the maneuvering angles around the x and z axes, which are required in order to maneuver around the y axis, are analytically determined, and the total time required to maneuver around the y axis is then analyzed numerically. Even if only two CMGs are available for attitude control, minimizing the spacecraft maneuvering time is still desirable for space missions such as search and observation of gamma-ray bursts. Therefore, in this chapter, the minimum time required for a given maneuvering sequence is also discussed.

2.2 Pyramid-type CMG Systems

In this section, first a traditional pyramid-type CMGs system (Fig. 2.1) is addressed and then the two-CMG system treated herein is described.

Let XYZ be the CMG reference frame, as shown in Fig. 2.1. For simplicity, the following assumptions are made in this chapter. The moment of inertia tensor of the satellite is diagonal, the CMG reference frame XYZ is coincident with the satellite body frame xyz, and the moment of inertia tensor of the satellite with the CMG system does not depend on the rotation of the gimbals.

2.2.1 Pyramid-type four-CMG system

For a conventional pyramid mounting of four SGCMGs (Fig. 2.1), the total CMG angular momentum vector $\boldsymbol{h}$ is expressed in the spacecraft reference frame as

$$\boldsymbol{h} = \sum_{i=1}^{4} \boldsymbol{H}_i(\delta_i) = H \begin{bmatrix} -c\beta \sin\delta_1 \\ \cos\delta_1 \\ s\beta \sin\delta_1 \end{bmatrix} + H \begin{bmatrix} -\cos\delta_2 \\ -c\beta \sin\delta_2 \\ s\beta \sin\delta_2 \end{bmatrix} + H \begin{bmatrix} c\beta \sin\delta_3 \\ -\cos\delta_3 \\ s\beta \sin\delta_3 \end{bmatrix} + H \begin{bmatrix} \cos\delta_4 \\ c\beta \sin\delta_4 \\ s\beta \sin\delta_4 \end{bmatrix} \tag{2.1}$$

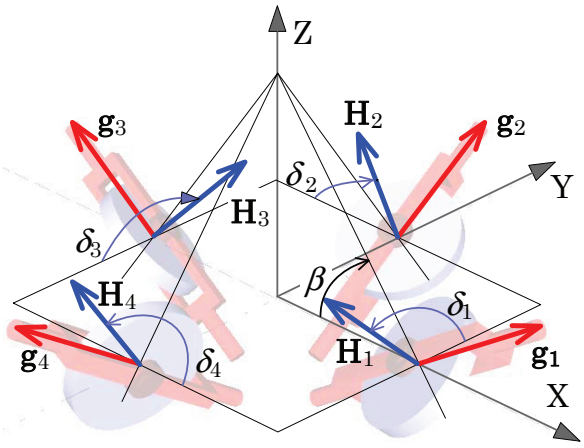

Figure 2.1: Pyramid-type four-CMG system.

where $c\beta \equiv \cos\beta$, $s\beta \equiv \sin\beta$, δ_i is the gimbal angle of the i^{th} CMG unit, and β is the pyramid skew angle. For simplicity, the momentum magnitude for each CMG, H, is sometimes assumed to be constant and equal to one without loss of generality, and the wheel momentum is assumed to be dominated by the momentum about the spin axis. In ordinary pyramid-array systems, the skew angle is fixed at $\beta = \tan^{-1}\sqrt{2}$ rad (= 54.73 deg) because, in this case, the shape of the momentum envelope approaches a sphere, and the system can easily cover an arbitrary direction.

The time derivative of the angular momentum vector for a typical CMG can be written as

$$\dot{\boldsymbol{h}} = \sum_{i=1}^{4} \frac{\partial \boldsymbol{H}_i}{\partial \delta_i}\dot{\delta}_i = H\boldsymbol{C}\dot{\boldsymbol{\delta}} \tag{2.2}$$

where

$$\boldsymbol{C} = \begin{bmatrix} -c\beta\cos\delta_1 & \sin\delta_2 & c\beta\cos\delta_3 & -\sin\delta_4 \\ -\sin\delta_1 & -c\beta\cos\delta_2 & \sin\delta_3 & c\beta\cos\delta_4 \\ s\beta\cos\delta_1 & s\beta\cos\delta_2 & s\beta\cos\delta_3 & s\beta\cos\delta_4 \end{bmatrix} \tag{2.3}$$

There exists a singular direction $\boldsymbol{u}$ perpendicular to the plane of $\dot{\boldsymbol{h}}$ such that $\dot{\boldsymbol{h}}\cdot\boldsymbol{u} = 0$. The CMG array cannot produce torque around the direction of the vector $\boldsymbol{u}$, regardless of the gimbal rate. This situation is referred to as a singularity. The corresponding gimbal

angles are called singular gimbal angles, and the corresponding momentum vector is called the singular momentum vector. In addition, the corresponding vector $\boldsymbol{u}$ is the singular vector. Because the torques generated by CMGs are always orthogonal to the gimbal vector, the singular momentum vector $\boldsymbol{h}_s$ is expressed using the gimbal vector $\boldsymbol{g}_i$ and the unit sphere vector $\boldsymbol{u}_s$ as

$$\boldsymbol{h}_s = \sum_{i=1}^{4} \frac{\varepsilon_i \left(\boldsymbol{g}_i \times \boldsymbol{u}_s\right) \times \boldsymbol{g}_i}{|\boldsymbol{g}_i \times \boldsymbol{u}_s|} \tag{2.4}$$

where $\varepsilon_i = \text{sign}(e_i) = \text{sign}\left(\boldsymbol{H}_i \cdot \boldsymbol{u}_s\right) = \pm 1$. When $\varepsilon_i = 1$, the resulting singular surface is the 4H singularity, and when some of ε_i is 1 and others are -1, the resulting singular surfaces are the internal singularities.

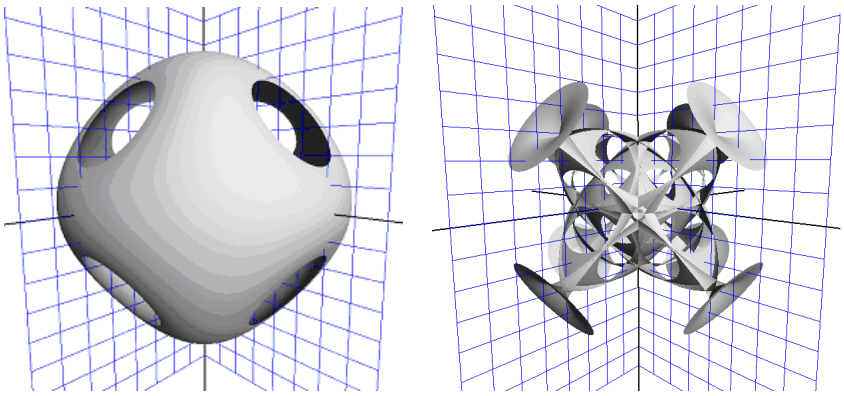

(a) (b)

Figure 2.2: (a) 4H singular surfaces, and (b) some internal singularities of pyramid-type CMG system .

Figures 2.2(a) and 2.2(b) show the 4H singular surface and some of the internal singular surfaces of a pyramid-type CMG system, respectively. Although 4H singularities can be easily obtained and avoided, they are sometimes actively used to achieve fast attitude maneuvering. On other hand, internal singularities cannot be easily predicted or avoided during attitude maneuver control. For this reason, singularity avoidance control methods are strongly required for CMG systems.

2.2.2 Pyramid-type Two-CMG system

In this chapter, it is assumed that the second and fourth gimbal angles are fixed at zero, but the first and third gimbals are available to generate the attitude control torques. This assumption corresponds to a situation in which the two diagonal units of the CMG system are malfunctioning, but attitude maneuvering is still required using the operational CMG gimbals. Although it is also possible that the first and second gimbals are available, but the third and fourth are not, such a case is not treated in this chapter. Attitude maneuver problems for such a 2SGCMG configuration will be a subject for the future study. Figure 2.3 shows a schematic diagram of the pyramid-type two-CMG system considered in this chapter. Under the above assumption, the angular moments possessed by the second and fourth CMG units are opposite to each other. As such, it is unnecessary to consider these angular moments. Hereafter, only the first and third CMG units are considered. In this case, the total angular moment vector possessed by the 2SGCMG system is expressed by

$$\boldsymbol{h} = H \begin{bmatrix} -c\beta \sin\delta_1 \\ \cos\delta_1 \\ s\beta \sin\delta_1 \end{bmatrix} + H \begin{bmatrix} c\beta \sin\delta_3 \\ -\cos\delta_3 \\ s\beta \sin\delta_3 \end{bmatrix} . \tag{2.5}$$

The time derivative of the angular momentum vector for the 2SGCMG system can be written as

$$\dot{\boldsymbol{h}} = H \begin{bmatrix} -c\beta \cos\delta_1 & c\beta \cos\delta_3 \\ -\sin\delta_1 & \sin\delta_3 \\ s\beta \cos\delta_1 & s\beta \cos\delta_3 \end{bmatrix} \begin{bmatrix} \dot{\delta}_1 \\ \dot{\delta}_3 \end{bmatrix} . \tag{2.6}$$

In contrast to the traditional pyramid-type four-CMG system, the two-CMG system has only two degrees of freedom (DOF) with respect to the gimbal angles. Therefore, all of the gimbal angles correspond to singular gimbal angles, and singularity avoidance does not make sense for the two-CMG system. The singular surface for the 2SGCMG system is shown in Fig. 2.4(a). Similar to the four-CMG system, hollows are observed in the direction of the gimbal vector. These hollows are the internal singularities that

correspond to the trumpet-like parts of the four-CMG system. To visualize the inner structure of the singular surface, cross sections at $Y = 0$ and $Z = 0$ are shown in Figs. 2.4(b) and (c), respectively. From Figs. 2.4(b) and (c), it can be seen that the singular surface of the 2SGCMG exists along the X and Z axes, but not along the Y axis.

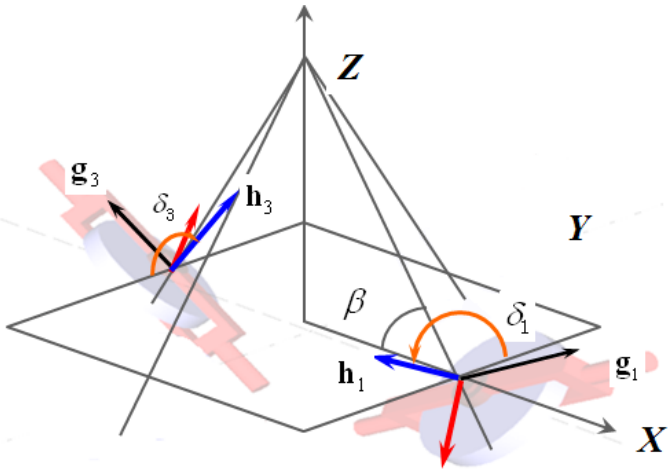

Figure 2.3: Pyramid-type two-CMG system.

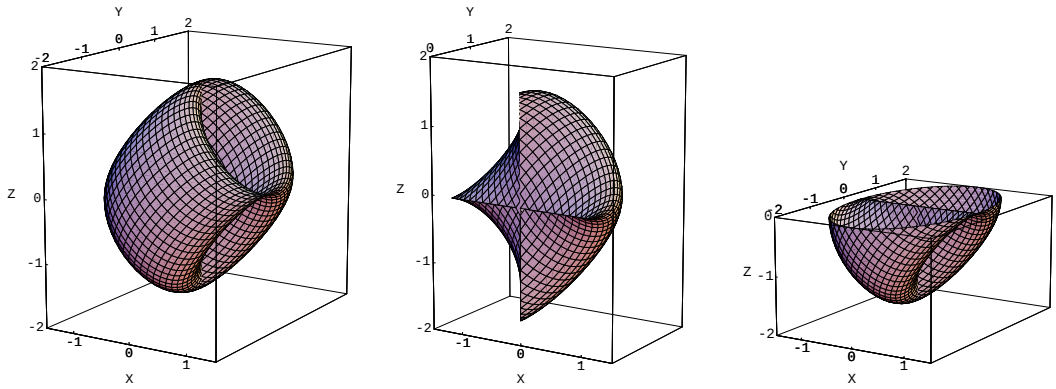

(a) (b) (c)

Figure 2.4: Singular surface of pyramid-type two-CMG system.

2.3 Attitude Maneuver by 2SGCMG System

The singular surfaces of the 2SGCMG system were described in the previous section. Unlike the case in which two RWs are used for three-axis attitude maneuver, because the 2SGCMG system can possess an angular moment along arbitrary directions other than the direction of the gimbal vectors, three-axes maneuver using the 2SGCMG system may be easier than that using two RWs. However, since the 2SGCMG system cannot generate independent torque around the x and z axes simultaneously, control methods that are used for the two-RW system are not directly applicable to the 2SGCMG system.

In this section, a method for attitude maneuver around each axis is considered. Then, the attitude change sequences and switching times of the gimbal steering sequences are considered in order to minimize the maneuvering time.

2.3.1 Attitude maneuver around the x or z Axis

In this subsection, attitude maneuvering around the x and z axes is discussed.

Torque generation

Attitude control torque around the x axis can be generated by changing gimbal angles δ_1 and δ_3 in the opposite directions, that is, $\delta_1 = \delta, \delta_3 = -\delta, \dot{\delta}_1 = \dot{\delta}, \dot{\delta}_3 = -\dot{\delta}$, as follows:

$$\begin{bmatrix} \tau_x \\ \tau_y \\ \tau_z \end{bmatrix} = -\dot{\boldsymbol{h}} = -H \begin{bmatrix} -c\beta\cos\delta & c\beta\cos(-\delta) \\ -\sin\delta & \sin(-\delta) \\ s\beta\cos\delta & s\beta\cos(-\delta) \end{bmatrix} \begin{bmatrix} \dot{\delta} \\ -\dot{\delta} \end{bmatrix} = \begin{bmatrix} 2H\dot{\delta}c\beta\cos\delta \\ 0 \\ 0 \end{bmatrix}. \tag{2.7}$$

Similarly, attitude control torque around the z axis can be generated by changing gimbal angles δ_1 and δ_3 in the same direction, that is, $\delta_1 = \delta_3 = -\delta, \dot{\delta}_1 = \dot{\delta}_3 = -\dot{\delta}$, as follows:

$$\begin{bmatrix} \tau_x \\ \tau_y \\ \tau_z \end{bmatrix} = -\dot{\boldsymbol{h}} = -H \begin{bmatrix} -c\beta\cos(-\delta) & c\beta\cos(-\delta) \\ -\sin(-\delta) & \sin(-\delta) \\ s\beta\cos(-\delta) & s\beta\cos(-\delta) \end{bmatrix} \begin{bmatrix} -\dot{\delta} \\ -\dot{\delta} \end{bmatrix} = \begin{bmatrix} 0 \\ 0 \\ 2H\dot{\delta}s\beta\cos\delta \end{bmatrix}. \tag{2.8}$$

Maneuvering time and switching timings of gimbal steering

From the viewpoint of minimizing the maneuvering time, as Pontryagin's principle suggests, optimal controllers are usually switching-type controllers, such as bang-bang controllers. Therefore, in order to generate control torque around the x axis or z axis, let us assume that the gimbal rate is constant at $\dot{\delta}$. Moreover, it is assumed that the gimbal angles are initially zero. In this case, the time required for the gimbal angle to change from zero to $\pi/2$ rad is given by

$$t^* = (\pi/2)/\dot{\delta} \ . \tag{2.9}$$

Under the above assumptions, first a rest-to-rest maneuver around the x axis is considered. Because the torque generated around the x axis is given by $2H\dot{\delta}c\beta\cos\delta$, as shown in Eq. (2.7), the angular velocity and attitude maneuver angle resulting from the above torque around the x axis, ω_x and θ_x, can be respectively expressed for the time range of $t \in [0, t^*]$ by

$$\omega_x(t) = \int_0^t \tau_x/J_x dt = (2H\dot{\delta}c\beta/J_x)\int_0^t \cos(\dot{\delta}t)dt = \frac{2Hc\beta}{J_x}\sin(\dot{\delta}t) \ , \tag{2.10}$$

$$\theta_x(t) = \int_0^t \omega_x(t)dt = (2Hc\beta/J_x)\int_0^t \sin(\dot{\delta}t)dt = \frac{2Hc\beta}{J_x\dot{\delta}}\left[1-\cos(\dot{\delta}t)\right] \ . \tag{2.11}$$

In order to nullify the angular velocity resulting from the gimbal steering described above, the gimbal steering rates must be reversed and the gimbals must stop at angles of zero. If the magnitude of the reverse steering rate is the same as that of the forward steering rate, then to return the gimbal angles to zero, the same time is required for both steering processes. During the reverse process, the spacecraft maneuvers through the same angle as in the forward steering process. In short, if the gimbal rates are set to $(\dot{\delta}_1, \dot{\delta}_3) = (\dot{\delta}, -\dot{\delta})$ from $t = 0$ to $t = t^*$, and set to $(\dot{\delta}_1, \dot{\delta}_3) = (-\dot{\delta}, \dot{\delta})$ from $t = t^*$ to $t = 2t^*$, then the total maneuver angle around the x axis is obtained as

$$\theta_x^* = \frac{4Hc\beta}{J_x\dot{\delta}} \ . \tag{2.12}$$

For the case in which the required maneuver angle θ_{xf} is less than θ_x^*, the gimbals must be reversed before reaching $\pi/2$ rad. Taking Eq. (2.11) into consideration, the

reverse steering time t_{x1} is given by

$$t_{x1} = \frac{1}{\dot{\delta}} \cos^{-1}\left(1 - \frac{J_x \dot{\delta} \theta_{xf}}{4Hc\beta}\right) . \tag{2.13}$$

The total maneuvering time to achieve θ_{xf} for the case of $\theta_{xf} \leq \theta_x^*$ is given by

$$t_x = 2t_{1x} = \frac{2}{\dot{\delta}} \cos^{-1}\left(1 - \frac{J_x \dot{\delta} \theta_{xf}}{4Hc\beta}\right) . \tag{2.14}$$

On the other hand, for the case in which θ_{xf} is greater than θ_x^*, the gimbal angles should remain at $\pm\pi/2$ so that the spacecraft can obtain the maximum angular velocity $\omega_x = 2Hc\beta/J_x$ for the x-axis maneuver, and this angular velocity should be maintained in order to minimize the maneuvering time. The duration of coursing t_{x2} needed to cover the gap between θ_{xf} and θ_x^* resulting from the bang-bang steering rate is given by

$$t_{x2} = \frac{J_x(\theta_{xf} - \theta_x^*)}{2Hc\beta} . \tag{2.15}$$

The total maneuvering time for achieving θ_{xf} for the case of $\theta_{xf} > \theta_x^*$ is given by

$$t_x = 2t^* + t_{x2} = \frac{\pi}{\dot{\delta}} + \frac{J_x(\theta_{xf} - \theta_x^*)}{2Hc\beta} . \tag{2.16}$$

Next, a rest-to-rest maneuver around the z axis is considered. Because the torque generated around the z axis is given by $2H\dot{\delta}s\beta\cos\delta$, as shown in Eq. (2.8), the angular velocity and attitude maneuver angle resulting from the torque around the z axis, ω_z and θ_z, respectively, for the time range of $t \in [0, t^*]$ can be written as

$$\omega_z(t) = \int_0^t \tau_z/J_z dt = (2H\dot{\delta}s\beta/J_z)\int_0^t \cos(\dot{\delta}t)dt = \frac{2Hs\beta}{J_z}\sin(\dot{\delta}t) , \tag{2.17}$$

$$\theta_z(t) = \int_0^t \omega_z(t)dt = (2Hs\beta/J_z)\int_0^t \sin(\dot{\delta}t)dt = \frac{2Hs\beta}{J_z\dot{\delta}}\left[1 - \cos(\dot{\delta}t)\right] . \tag{2.18}$$

The total maneuver angle around the z axis resulting from the bang-bang steering rate control is

$$\theta_z^* = \frac{4Hs\beta}{J_z\dot{\delta}} . \tag{2.19}$$

For the case in which θ_{zf} is less than θ_z^*, the gimbal angles must be reversed before reaching $\pi/2$ rad. Taking Eq. (2.18) into consideration, the reverse steering time t_{z1} is

obtained as

$$t_{z1} = \frac{1}{\dot{\delta}} \cos^{-1}\left(1 - \frac{J_z \dot{\delta} \theta_{zf}}{4Hs\beta}\right) . \tag{2.20}$$

The total maneuvering time for achieving θ_{zf} for the case of $\theta_{zf} \leq \theta_z^*$ is

$$t_z = 2t_{z1} = \frac{2}{\dot{\delta}} \cos^{-1}\left(1 - \frac{J_z \dot{\delta} \theta_{zf}}{4Hs\beta}\right) . \tag{2.21}$$

On the other hand, for the case in which θ_{zf} is greater than θ_z^*, the gimbal angles should remain at $\pm\pi/2$ so that the spacecraft can obtain the maximum angular velocity $\omega_z = 2Hs\beta/J_z$ for the z-axis maneuver, and this angular velocity should be maintained in order to minimize the maneuvering time. The duration of coasting t_{z2} needed to cover the gap between θ_{zf} and θ_z^* resulting from the bang-bang steering rate is given by

$$t_{z2} = \frac{J_z(\theta_{zf} - \theta_z^*)}{2Hs\beta} . \tag{2.22}$$

The total maneuvering time for achieving θ_{zf} for the case of $\theta_{zf} > \theta_z^*$ is

$$t_z = 2t^* + t_{z2} = \frac{\pi}{\dot{\delta}} + \frac{J_z(\theta_{zf} - \theta_z^*)}{2Hs\beta} . \tag{2.23}$$

Figure 2.5 shows a schematic diagram summarizing the relationship among the gimbal rate, gimbal angle, maneuvering angle, and timing of the steering switching, where the solid, broken and dashed lines correspond to the cases of $\theta_f > \theta^*$, $\theta_f = \theta^*$, and $\theta_f < \theta^*$, respectively.

2.3.2 Maneuver around the y Axis

When a torque around the y axis is generated using the 2SGCMG system, torques are also generated around the x and z axes. In other words, a torque around the y axis cannot be generated independently of torques around the x and z axes. It might be possible to achieve the y axis maneuver without an attitude shift around the x and z axes by canceling the latter two shifts using the torques around the x and z axes. However, it is difficult to devise such a continuous smooth steering control law for the y axis maneuver using the 2SGCMG system.

Attitude maneuver sequence and trigonometry

In this chapter, to achieve the y-axis maneuver, discontinuous steering control laws are considered, which use the corning effect resulting from alternate maneuvers around the x and z axes. There are four candidate procedures, which are hereinafter referred to as methods-1 through 4.

A schematic diagram of the procedure of method-1 is shown in Fig. 2.6(a). Method-1 consists of the following four steps:

1. maneuver a rad around the z axis,
2. maneuver b rad around the x axis of the body frame,
3. maneuver $-c$ rad around the z axis of the body frame, and
4. maneuver $-d$ rad around the x axis of the body frame.

It should be noted that the angles (a, b, c, d) cannot be chosen independently, but must be appropriately chosen to achieve the required maneuver around the y axis α without causing any residual attitude shift around the x and z axes at the end of the maneuver. By taking the final attitude and spherical trigonometry into consideration, the maneuver angle parameters b, c, and d can be expressed in terms of α and a as follows:

$$b = \tan^{-1}(\tan\alpha / \sin a) , \tag{2.24}$$

$$c = \cos^{-1}(\cos\alpha \cdot \cos a) , \tag{2.25}$$

$$d = \tan^{-1}(\sin\alpha / \tan a) . \tag{2.26}$$

Selection of these three maneuver angles results in the required attitude change around the y axis of the spacecraft body frame, α.

A schematic diagram of the procedure of method-2 is shown in Fig. 2.6(b). It should be noted that method-2 is a special case of method-1, because setting a to $\pi/2$ results in $b = \alpha$, $c = \pi/2$, and $d = 0$ rad. This method consists of the following three steps:

1. maneuver $\pi/2$ rad around the z axis, and then make the x axis of the spacecraft coincident with the y axis of the inertial frame,

2. maneuver the required angle α around the y axis of the inertial frame, that is, around the x axis of the spacecraft body frame, and

3. maneuver $-\pi/2$ rad around the z axis of the spacecraft body frame.

The maneuver procedure of method-3, which consists of the following four steps, is shown in Fig. 2.6(c).

1. maneuver d rad around the x axis,

2. maneuver $-c$ rad around the z axis of the body frame,

3. maneuver $-b$ rad around the x axis of the body frame, and

4. maneuver a rad around the z axis of the body frame.

Method-4 consists of the following three steps, as shown in Fig. 2.6(d).

1. maneuver $\pi/2$ rad around the x axis,

2. maneuver the required angle α around the y axis of the inertial frame, that is, around the $-z$ axis of the spacecraft body frame, and

3. maneuver $-\pi/2$ rad around the x axis of the spacecraft body frame.

Similar to the relationship between method-1 and method-2, method-4 is a special case of method-3, in which d is set to $\pi/2$. It should be noted that the difference between method-1 and method-3, or between method-2 and method-4, is the order of the maneuver axes, x and z.

The choice of which of the four methods to use depends on the objectives or requirements of the maneuver. For example, method-2 or method-4 should be chosen for the case in which fewer maneuvers are desired. On the other hand, considering an example in which a star sensor is installed on the x axis of a spacecraft body frame and the Sun is located along the y axis of the inertial frame, then the method-2 should be avoided, and method-1 or method-3 should be chosen so as to prevent the star sensor from pointing

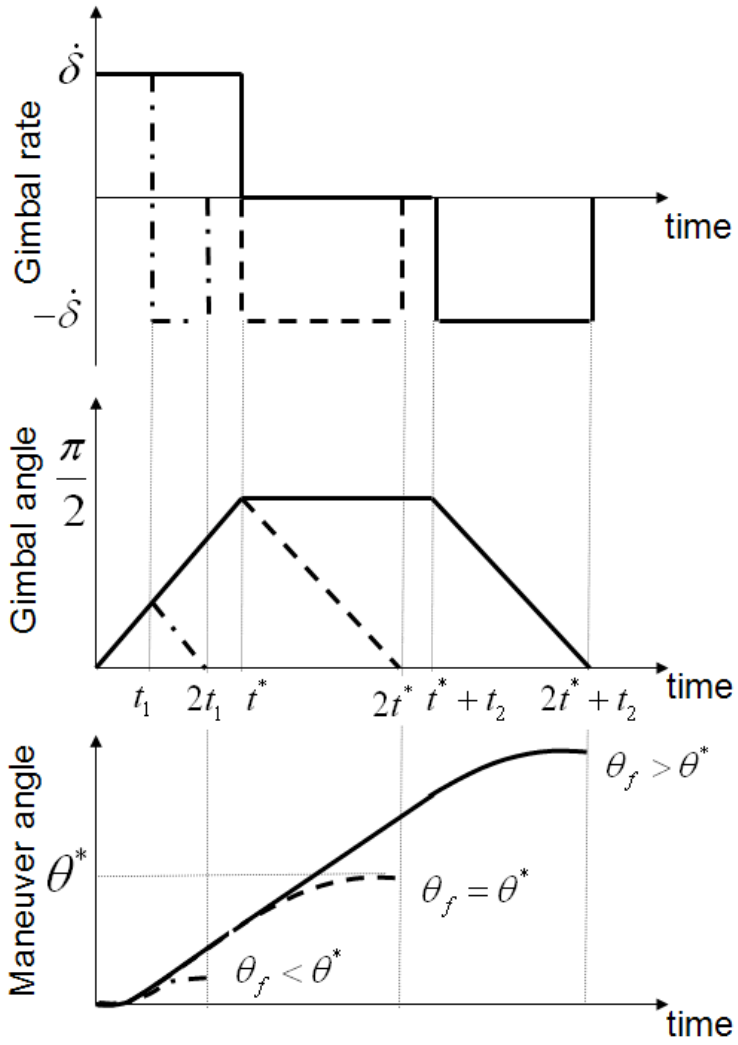

Figure 2.5: Schematic representation of the relationship among the gimbal rate, gimbal angle, maneuver angle, timing of steering switching.

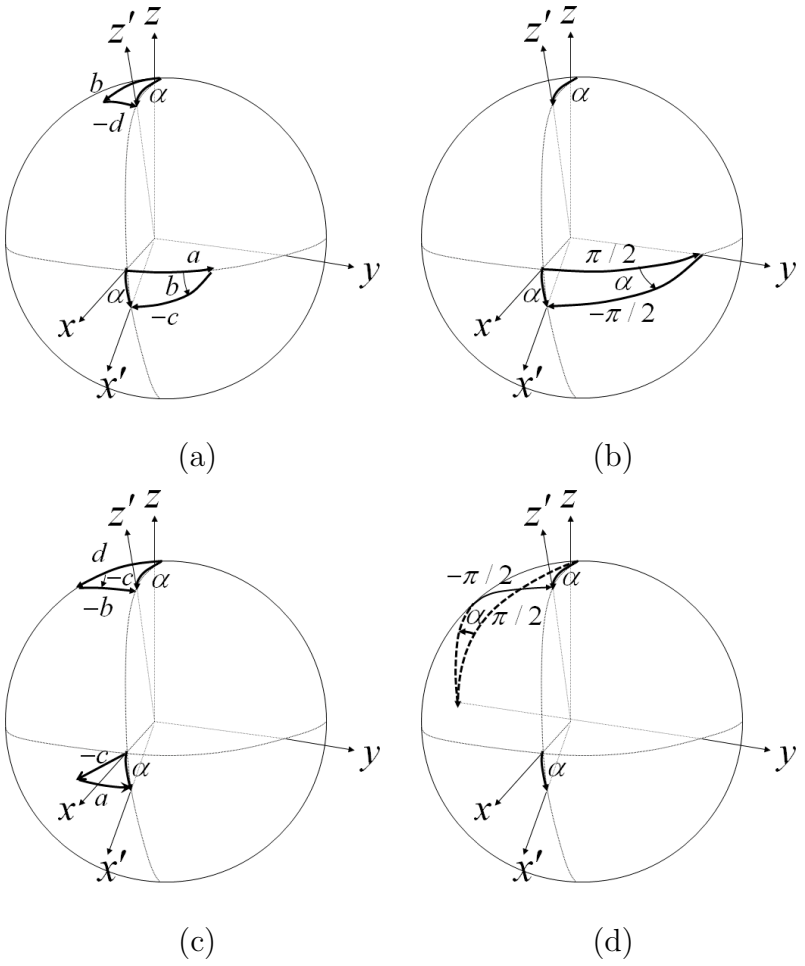

Figure 2.6: Procedures for maneuver around the y axis.

toward the Sun. Even if the required maneuver angle cannot be achieved around the y axis by carrying out method-1 or method-3 a single time, it can still be achieved by repeating the method multiple times.

Maneuvering time

The total maneuvering time for each method can be obtained by calculating the time for each maneuver and summing these times. As mentioned earlier, the maneuver angles b, c, and d are expressed in terms of α and a. Therefore, the total maneuvering time is a function of α and a, and can be represented in the form of a three-dimensional surface, the x, y and z axes of which are the parameters α, a, and the total maneuvering time, respectively. In addition, a minimum maneuvering time and the optimal maneuver angle a exist for α.

Let $a_i, (i = a, b, c, d)$ denote a boundary angle at which the expression of the time for each step switches in accordance with necessity of coasting in each maneuvering step. By comparing the angles a and c with θ_z^*, and comparing the angles b and d with θ_x^*, equations to determine the angles a_a, a_b, a_c and a_d can be given by

$$a(\alpha, a) = a_a(\alpha) = \theta_z^* \ , \tag{2.27}$$

$$b(\alpha, a) = \tan^{-1}\left(\frac{\tan\alpha}{\sin a_b(\alpha)}\right) = \theta_x^* \ , \tag{2.28}$$

$$c(\alpha, a) = \cos^{-1}\left(\cos\alpha \cdot \cos a_c(\alpha)\right) = \theta_z^* \ , \tag{2.29}$$

$$d(\alpha, a) = \tan^{-1}\left(\frac{\sin\alpha}{\tan a_d(\alpha)}\right) = \theta_x^* \ . \tag{2.30}$$

Note that a_a, a_b, a_c and a_d are expressed in the form of a function of α, because they depend on α except for a_a. In this chapter, the functions $a_a(\alpha)$, $a_b(\alpha)$, $a_c(\alpha)$ and $a_d(\alpha)$ will be shown in Fig. 2.7.

Replacing θ_{xf} with the angle b or d, replacing θ_{zf} with the angle a or c, substituting Eq.(2.12) into θ_x^*, substituting Eq.(2.19) into θ_z^*, and using Eqs. (2.24), (2.25), and (2.26)

for b, c, and d, the time for each maneuvering step, t_a, t_b, t_c, and t_d, can be expressed as

$$t_a(\alpha, a) = \begin{cases} \dfrac{2}{\dot{\delta}} \cos^{-1}\left(1 - \dfrac{J_z \dot{\delta} a}{4Hs\beta}\right) & \text{for } a \le \theta_z^* \quad (2.31a) \\ \dfrac{\pi}{\dot{\delta}} + \dfrac{J_z}{2Hs\beta}\left(a - \dfrac{4Hs\beta}{J_z\dot{\delta}}\right) & \text{for } a > \theta_z^* \quad (2.31b) \end{cases}$$

$$t_b(\alpha, a) = \begin{cases} \dfrac{2}{\dot{\delta}} \cos^{-1}\left(1 - \dfrac{J_x \dot{\delta}}{4Hc\beta} \tan^{-1}(\tan\alpha / \sin a)\right) & \text{for } b(\alpha, a) \le \theta_x^* \quad (2.32a) \\ \dfrac{\pi}{\dot{\delta}} + \dfrac{J_x}{2Hc\beta}\left(\tan^{-1}(\tan\alpha/\sin a) - \dfrac{4Hc\beta}{J_x\dot{\delta}}\right) & \text{for } b(\alpha, a) > \theta_x^* \quad (2.32b) \end{cases}$$

$$t_c(\alpha, a) = \begin{cases} \dfrac{2}{\dot{\delta}} \cos^{-1}\left(1 - \dfrac{J_z \dot{\delta}}{4Hs\beta} \cos^{-1}(\cos\alpha \cos a)\right) & \text{for } c(\alpha, a) \le \theta_z^* \quad (2.33a) \\ \dfrac{\pi}{\dot{\delta}} + \dfrac{J_z}{2Hs\beta}\left(\tan^{-1}(\cos\alpha\cos a) - \dfrac{4Hs\beta}{J_z\dot{\delta}}\right) & \text{for } c(\alpha, a) > \theta_z^* \quad (2.33b) \end{cases}$$

$$t_d(\alpha, a) = \begin{cases} \dfrac{2}{\dot{\delta}} \cos^{-1}\left(1 - \dfrac{J_x \dot{\delta}}{4Hc\beta} \tan^{-1}(\sin\alpha / \sin a)\right) & \text{for } d(\alpha, a) \le \theta_x^* \quad (2.34a) \\ \dfrac{\pi}{\dot{\delta}} + \dfrac{J_x}{2Hc\beta}\left(\tan^{-1}(\sin\alpha/\tan a) - \dfrac{4Hc\beta}{J_x\dot{\delta}}\right) & \text{for } d(\alpha, a) > \theta_x^* \quad (2.34b) \end{cases}$$

The total time for maneuvering around the y axis is expressed in terms of α and a as

$$t(\alpha, a) = t_a(\alpha, a) + t_b(\alpha, a) + t_c(\alpha, a) + t_d(\alpha, a)\ . \quad (2.35)$$

2.4 Numerical Case Studies

In this section, the total maneuvering time for each method will be evaluated for two cases of moment of inertia. In case-1, the moment of inertia about the x axis is assumed to be less than that about the z axis, whereas in case-2, the moment of inertia about the x axis is assumed to be greater. By comparing the results for case-1 and case-2, the effect of the moment of inertia on the minimum-time maneuver of the spacecraft using the 2SGCMG system will be evaluated under the assumed maneuver sequence. The parameters for these case studies are as follows: $|\dot{\delta}| = \pi/20$ rad/s, $H = 0.044$ Nms, $J_x = 1.34$ kgm^2 and $J_z = 3.27$ kgm^2 for case-1, and $J_x = 3.27$ kgm^2 and $J_z = 1.34$ kgm^2

for case-2. It should be noted that the moment of inertia about the y axis has no effect on the maneuvering time, because a single spin motion around only the x or z axis is assumed in this study. If gyroscopic effects are considered, it is necessary to study the effect of the moment of inertia about the y axis on the maneuvering time. This will be a topic for the future study. In addition, it should be noted that because the maneuver angles around the x and z axes in method-3 are the same as those in method-1, the minimum maneuvering times obtained using method-1 and method-3 are the same and the numerical results for method-3 are thus omitted.

2.4.1 Maps of expression of maneuvering time

Substituting the moments of inertia, J_x, J_z, and maximum gimbal rate $\dot{\delta}$ into Eqs.(2.12) and (2.19) gives $\theta_x^* = 0.483$ rad and $\theta_z^* = 0.280$ rad for case-1, and $\theta_x^* = 0.198$ rad, and $\theta_z^* = 0.683$ rad, for case-2, respectively. By taking the conditions for the boundary angles (Eqs. (2.27) through (2.30)) into consideration, region maps of the expression of the total maneuvering time can be obtained. Figures 2.7(a) and 2.7(b) show the region maps of the expression of the total maneuvering time for case-1, and case-2, respectively. Note that in Figs. 2.7(a) and 2.7(b), the domain is clipped to within $[0, \pi/2] \times [0, \pi/2]$. Because the boundary $a_a(\alpha)$ (Eq. (2.27)) does not depend on α, it is a straight line at $a = \theta_z^*$, while the boundaries $a_b(\alpha)$, $a_c(\alpha)$ and $a_d(\alpha)$ (Eqs. (2.28), (2.29) and (2.30)) do depend on α. Both $a_b(\alpha)$ and $a_d(\alpha)$ begin at the origin and increase with α, while $a_c(\alpha)$ (Eq.(2.29)) begins at $a = \theta_z^*$, decreases as α increases, and finally reaches zero when $\alpha = 0.280$ rad for case-1, and when $\alpha = 0.683$ rad for case-2. Hereafter, $\alpha = 0.280$ rad is referred to as α_1^*, and $\alpha = 0.683$ rad is referred to as α_2^*. For both cases, the domain is divided into nine regions by the boundaries $a_a(\alpha)$, $a_b(\alpha)$, $a_c(\alpha)$ and $a_d(\alpha)$, as indicated in the figures. Figures 2.7(c) and 2.7(d) show magnified regions of Figs. 2.7(a) and 2.7(b), respectively, in order to illustrate the boundary regions in more detail. The expressions of the total maneuvering time corresponding to the different regions are listed in Table 2.1.

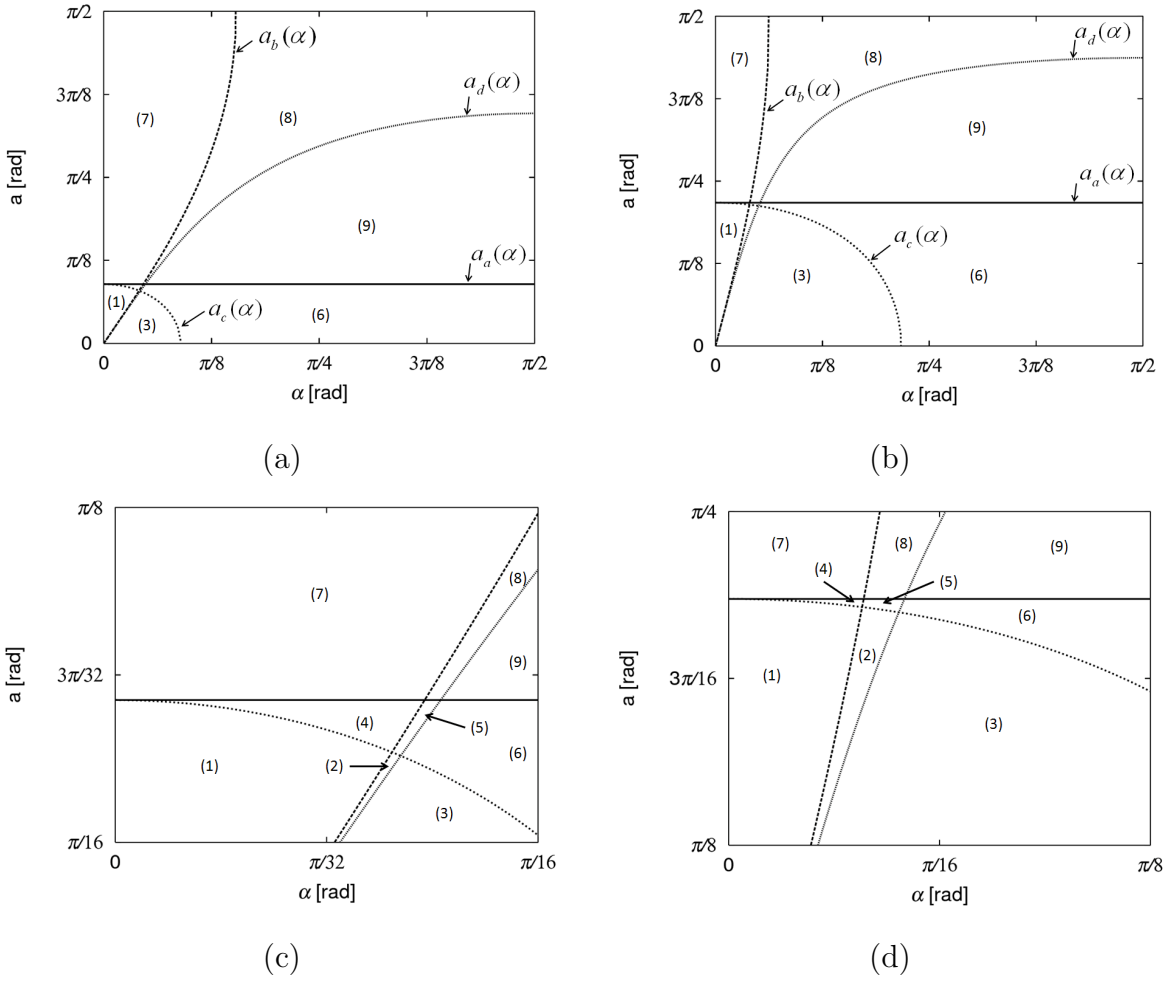

Figure 2.7: Region maps of expression of maneuvering time: (a) case-1, (b) case-2, (c) magnification of (a), and (d) magnification of (b).

Table 2.1: Expression of maneuvering time corresponding to each region.

Region	Total maneuvering time $t(\alpha, a)$
(1)	Eq.(2.31a) + Eq.(2.32a) + Eq.(2.33a) + Eq.(2.34a)
(2)	Eq.(2.31a) + Eq.(2.32b) + Eq.(2.33a) + Eq.(2.34a)
(3)	Eq.(2.31a) + Eq.(2.32b) + Eq.(2.33a) + Eq.(2.34b)
(4)	Eq.(2.31a) + Eq.(2.32a) + Eq.(2.33b) + Eq.(2.34a)
(5)	Eq.(2.31a) + Eq.(2.32b) + Eq.(2.33b) + Eq.(2.34a)
(6)	Eq.(2.31a) + Eq.(2.32b) + Eq.(2.33b) + Eq.(2.34b)
(7)	Eq.(2.31b) + Eq.(2.32a) + Eq.(2.33b) + Eq.(2.34a)
(8)	Eq.(2.31b) + Eq.(2.32b) + Eq.(2.33b) + Eq.(2.34a)
(9)	Eq.(2.31b) + Eq.(2.32b) + Eq.(2.33b) + Eq.(2.34b)

2.4.2 Maneuvering time and time-optimal maneuver angle a

Case-1: $J_x < J_z$

Figure 2.8 shows the maneuvering time for method-1 and case-1, represented in the form of a three-dimensional colored surface. It can be seen that when the required maneuver angle α is small, the total maneuvering time strongly depends on the first maneuver angle a, but this dependence is smaller when α is large.

The relationship between the minimum maneuvering time and the required maneuver angle around the y axis α is shown in Fig. 2.9. The maneuvering times for method-2 and method-4 are also shown for comparison. It can be seen that the minimum maneuvering time for method-1 is always less than that of method-2. This is because the moment of inertia about the x axis, J_x, is less than that about the z axis, J_z. Thus, in order to achieve a shorter maneuvering time, it is desired to more actively select a large maneuver angle around the x axis, rather than the z axis. In addition, it can be seen from Fig. 2.9 that as the required maneuver angle α increases, the difference in the maneuvering time between method-1 and method-2 becomes smaller.

Figure 2.10 shows the relationship between α and the corresponding optimal maneuver angle a. As shown in Fig. 2.10, when α is greater than α_2^*, the optimal maneuver angle a is zero, that is, the first maneuver is skipped in method-1 to obtain the time-optimal solution. On the other hand, when α is less than α_2^*, the optimal maneuver angle a is not zero, but varies between 0 and $\pi/8$ rad. In other words, the time-optimal solution still involves four maneuvers for method-1.

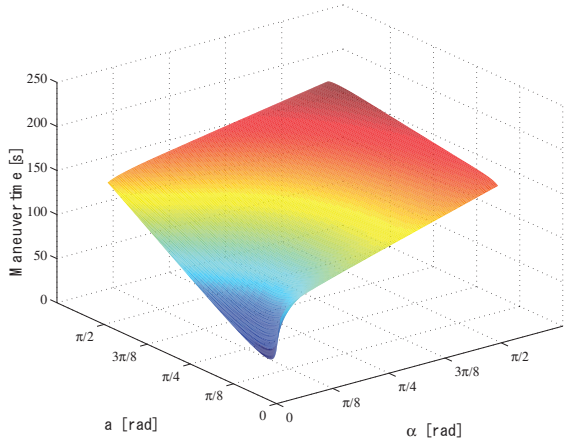

Figure 2.8: Maneuvering time for method-1 and case-1.

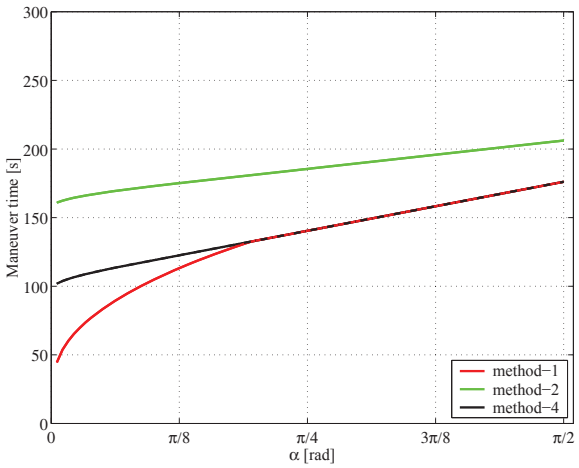

Figure 2.9: Maneuvering time vs. required maneuver angle around the y axis for case-1.

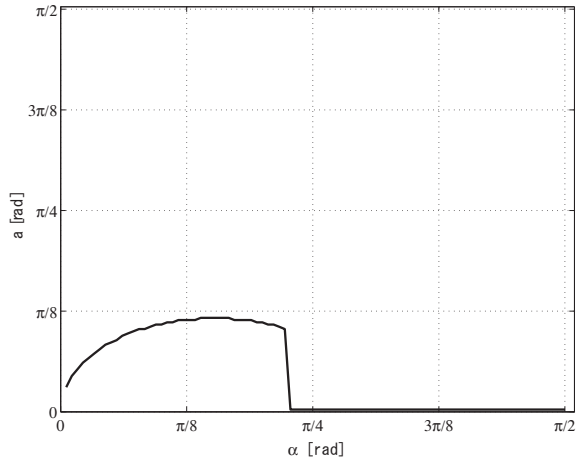

Figure 2.10: Required maneuver angle around the y axis vs. time-optimal first maneuver angle a for case-1.

Case-2: $J_x > J_z$

For case-2, the maneuvering time for method-1, represented in the form of a three-dimensional colored surface, is shown in Fig. 2.11. Similar to case-1, when α is small, the total maneuvering time strongly depends on the first maneuver angle a, but this dependence is smaller when α is large.

Figure 2.12 shows the relationship between the minimum maneuvering time and α. When α is small, the minimum maneuvering time for method-1 is less than that of method-2. However, when α is greater than α_1^*, the minimum maneuvering time for both methods is the same. In short, the optimal maneuver procedure is the same for both methods. The moment of inertia about the x axis, J_x, is greater than that of the z axis J_z. Therefore, in order to achieve a shorter maneuver time, it is desired to more actively select a large maneuver angle around the z axis, rather than the x axis.

The relationship between α and the corresponding optimal maneuver angle a is shown Fig. 2.13. When α is greater than α_1^*, the optimal maneuver angle a is $\pi/2$ rad, that is, the fourth maneuver is not necessary to obtain the time-optimal solution in method-1. On the other hand, as shown in Fig. 2.13, when α is less than α_1^*, the optimal maneuver

angle a is not $\pi/2$, but rather increases with α. In other words, the time-optimal solution still involves four steps in method-1 in this case.

In addition, it should be noted that although the moments of inertia about the x and z axes in case-2 are swapped with each other, compared to those of case-1, the results of case-1 and case-2 are not symmetric with respect to the first optimal maneuver angle a when α is small. This is because the control torques generated by the 2SGCMG system are not symmetric with respect to the x and z axes due to the inclined skew angle, and the maneuver sequences for case-1 and case-2 are not symmetric with each other with respect to the x and z axes. On the other hand, when α is large, the optimal first maneuver angle a is symmetric, i.e., $a = 0$ for case-1, while $a = \pi/2$ for case-2. In other words, as described in Section 3, the maneuvering time depends on the ratio between the moment of inertia J_x and $\cos\beta$, or J_z and $\sin\beta$.

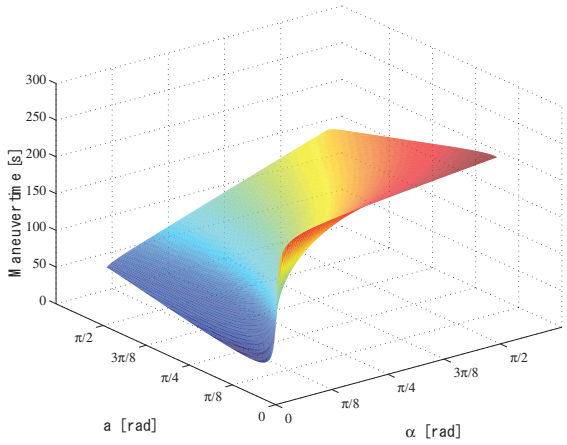

Figure 2.11: Maneuvering time for method-1 and case-2.

2.4.3 Numerical simulation

To verify the validity of the maneuver method and maneuvering time presented above, a numerical simulation is carried out for maneuvering around the y axis. The required maneuver angle is set to 20 deg. The parameters of the 2SGCMG system presented

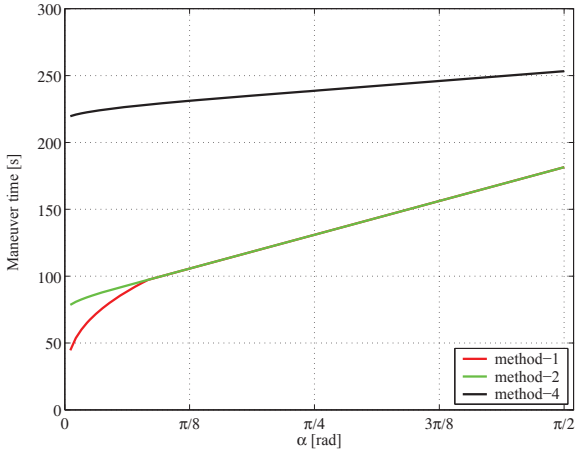

Figure 2.12: Maneuvering time vs. required maneuver angle around the y axis for case-2.

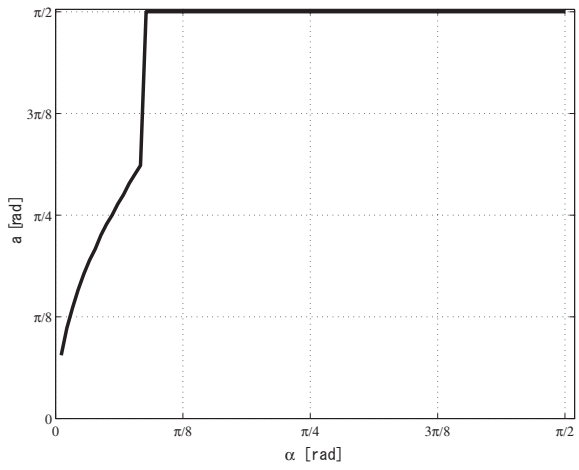

Figure 2.13: Required maneuver angle around the y axis vs. time-optimal first maneuver angle a for case-2.

above, and the satellite's moment of inertia in case-1 are used for the numerical simulation. For the present parameters, the minimum maneuvering time is determined to be 108.6 s using method-1 with the optimal maneuver angle $a = 20.00$ deg.

Figures 2.14(a) and (b) show the time responses of the angular velocities and attitude angles of the satellite, where the angular velocities are expressed in the satellite body frame, and attitude angles are expressed by roll(ϕ), pitch(θ) and yaw(ψ) angles. It is shown in Fig. 2.14(a) that the angular velocities become zero three times before the end of maneuver, and it is shown in Fig. 2.14(b) that the required attitude angle around the y axis, $\theta = 20$ deg, is successfully achieved. The maneuvering time is 108.6 s, which is the same as the analytical result. These numerical results show the validity of the maneuver method and maneuvering time presented in this chapter.

2.5 Conclusion

Rest-to-rest attitude maneuver problems for a satellite using two single-gimbal control moment gyros (2SGCMGs) have been considered. We assumed the same configuration as the traditional pyramid-array CMG system, but also assume that only two CMG units are available at the diagonal positions. Taking into consideration that the rest-to-rest maneuvers around the x and z axes of the satellite body frame can be achieved by the 2SGCMG system, a method by which to achieve a rest-to-rest maneuver around the y axis of the satellite body frame has been considered using the corning effect resulting from the rest-to-rest maneuvers around x and z axes. The maneuver angles around the x and z axes to achieve the maneuver around the y axis were determined based on spherical trigonometry. The total time required to complete the required maneuver around the y axis was then numerically evaluated for two different moments of inertia. The results of numerical case studies showed that when the required maneuver angle around the y axis is large, maneuvering around the minimum moment of inertia is prioritized to obtain the time-optimal solution. However, this tendency does not always apply when the required maneuver angle around the y axis is small.

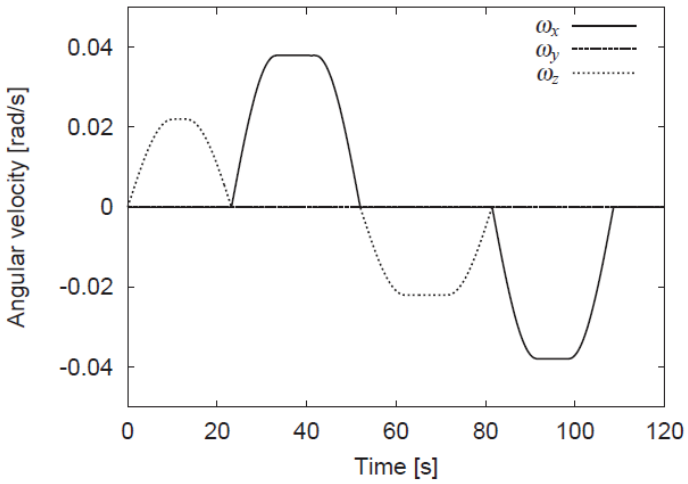

(a) Angular velocities

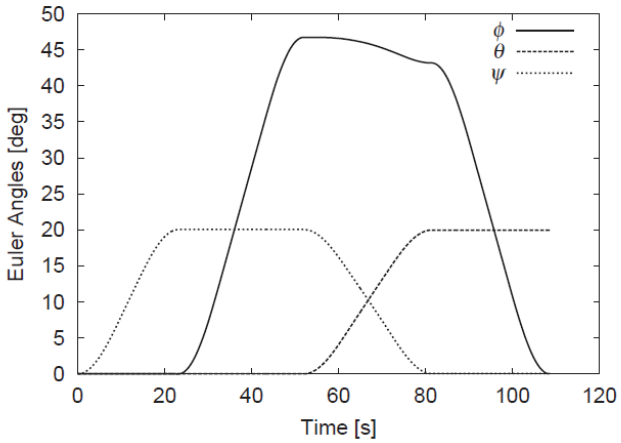

(b) Attitude Euler angles

Figure 2.14: Result of numerical simulation.

It is hoped that the results of this study will contribute to the development of a control strategy for minimum-time maneuvers of a spacecraft using a pyramid-type single-gimbal CMG system in a situation where only two diagonal units of the CMG system are available.

In the near future, this study will be extended to investigate attitude maneuver using a 2SGCMG system with another configuration, and to simultaneous three-axis maneuvers.

References

[1] Margulies, G., Aubrun, J.N.: Geometric Theory of Single-gimbal Control Moment Gyro System, *Journal of Astronautical Sciences*, **26**(1978), pp.159-191.

[2] Kurokawa, H: A Geometric Study of Single Gimbal Control Moment Gyros-Singularity Problems and Steering law, Tech. Rep. Report, Mechanical Engineering Laboratory, Japan, No.175, Jan., 1998.

[3] Vadali, S. R., Oh, H. S., Walker,S. R.: Preferred Gimbal Angles for Single Gimbal Control Moment Gyros, *Journal of Guidance, Control, and Dynamics*, **13**(1990), pp.1090-1095.

[4] Paradiso, J. A.: Global Steering of Single Gimbaled Control Moment Gyroscopes using a Directed Search, *Journal of Guidance, Control and Dynamics*, **15**(1992), pp.1236-1244.

[5] Bedrossian, N. S., Paradiso, J., Bergmann, E. V., Rowell, D.: Steering Law Design for Redundant Single-gimbal Control Moment Gyroscopes, *Journal of Guidance, Control, and Dynamics*, **13**(1990), pp.1083-1089.

[6] Oh, H. S., Vadali, S. R.: Feedback Control and Steering Laws for Spacecraft Using Single Gimbal Control Moment Gyros, *Journal of the Astronautical Sciences*, **39**(1991), pp.183-203.

[7] Ford, K. A., Hall, C. D.: Singular Direction Avoidance Steering for Control-moment Gyros, *Journal of Guidance, Control, and Dynamics*, **23**(2000), pp.648-656.

[8] Wie, B.,Bailey, D., Heiberg, C. J.: Singularity Robust Steering Logic for Redundant Single-gimbal Control Moment Gyros, *Journal of Guidance, Control, and Dynamics*, **24**(2001), pp.865-872.

[9] Wie, B.: Singularity Escape/Avoidance Steering Logic for Control Moment Gyro Systems, *Journal of Guidance, Control, and Dynamics*, **28**(2005), pp.948-956.

[10] Bedrossian, N. S., Paradiso, J., Bergmann, E. V., Rowell, D.: Redundant Single Gimbal Control Moment Gyroscope Singularity Analysis, *Journal of Guidance, Control, and Dynamics*, **13**(1990), pp.1096-1101.

[11] Kurokawa, H.: Constrained Steering Law of Pyramid-type Control Moment Gyros and Ground Tests, *Journal of Guidance, Control, and Dynamics*, **20**(1997), pp.445-449.

[12] Kurokawa, H.: Survey of Theory and Steering Laws of Single-gimbal Control Moment Gyros, *Journal of Guidance, Control and Dynamics*, **30**(2007), pp.1331-1340.

[13] Schaub, H., Junkins, J. L.: Singularity Avoidance using Null Motion and Variable-speed Control Moment Gyros, *Journal of Guidance Control, and Dynamics*, **23**(2000), pp.11-16.

[14] Takada, K., Kojima, H.: Receding Horizon Control on Steering of Control Moment Gyro for Fast Attitude Maneuver, *Transactions of the Japan Society for Aeronautical and Space Sciences*, **52**(2009), pp.1-10.

[15] Takada, K., Kojima, H., Matsuda, N.: Control Moment Gyro Singularity-avoidance Steering Control based on Singular-surface Cost Function, *Journal of Guidance, Control, and Dynamics*, **33**(2010), pp.1442-1450.

[16] Kojima, H.: Stabilization of Angular Velocity of Asymmetrical Rigid Spacecraft using Two Constant Torques, *Journal of Guidance, Control, and Dynamics*, **30**(2007), pp.1163-1168.

[17] Crouch, P. E.: Spacecraft Attitude Control and Stabilization: Application of Geometric Control Theory to Rigid Body Model, *IEEE Transactions on Automatic Control*, **29**(1984), pp.321-331.

[18] Brockett, R. W.: Asymptotic Stability and Feedback Stabilization, *Differential Geometric Control Theory*, **27**(1983), pp.181-208.

[19] Morin, P., Samson, C., Pomet, J. B.,Jiang, Z. P.: Time-varying Feedback Stabilization of the Attitude of a Rigid Spacecraft with Two Controls, *Systems & Control Letters*, **25**(1995), pp.375-385.

[20] Tsiotras, P.: Stabilization and Optimality Results for the Attitude Control Problem, *Journal of Guidance, Control, and Dynamics*, **19**(1995), pp.772-779.

[21] Kwon, S., Shimomura, T., Okubo, H.: Pointing Control of Spacecraft using Two SGCMGs via LPV Control Theory, *Acta Astronautica*, **68**(2011), pp.1168-1175.

Chapter 3

Gain-Scheduled Steering Control Law for Adaptive Skew Pyramid-type CMGs

Gain-scheduled steering control for adaptive skew pyramid-type control moment gyros (ASCMGs) is proposed. In contrast to previous studies that considered a fixed skew angle for pyramid type CMG systems, in the ASCMG, the skew angle is treated as a variable in order to obtain larger torques. The steering control law proposed for the ASCMG considers not only the gimbal angles but also the skew angle, and consists of an off-diagonal singularity robust inverse term and a null motion term.

The numerical results show that the skew angle has a tendency to change towards the normal skew angle in order to maintain the singularity free space as large as possible at the end of the maneuver. In addition, the settling time for the maneuver was shortened compared to the case of a fixed-skew angle SGCMG. Finally, by introducing a weighting function to the element associated with the skew angle in the off-diagonal matrix, the rate of change of the skew angle can be smoothly controlled to avoid chattering-like motion near singularities, and at the end of or after the maneuver.

Notation

$\boldsymbol{C}$	:	Fixed skew angle CMG Jacobian matrix
$\boldsymbol{D}$	:	Skew angle Jacobian vector
$\hat{\boldsymbol{e}}$	:	Quaternion common axis of rotation
$\boldsymbol{h}$	:	CMG system angular momentum vector
h_0	:	Angular momentum of one CMG unit
$\boldsymbol{I}_s$	:	$s-$Dimensional unit matrix
$\boldsymbol{J}$	:	Spacecraft inertia tensor, including CMG
k	:	Singularity avoidance law gain
$\boldsymbol{K}_p, \boldsymbol{K}_d$	:	Quaternion feedback control gains
$\boldsymbol{q}$	:	Quaternion
$\hat{\boldsymbol{q}}$	:	Quaternion vector component
$\boldsymbol{Q}$	:	Adaptive skew angle CMG Jacobian matrix $[\boldsymbol{C}, \boldsymbol{D}]$
$\boldsymbol{R}$	:	Direction cosine matrix
$\boldsymbol{u}$	:	Command torque
$\boldsymbol{W}, \tilde{\boldsymbol{W}}$	:	Weighting matrices
β	:	Skew angle
$\beta_{\max}$	:	Maximum allowed skew angle
$\beta_{\min}$	:	Minimum allowed skew angle
$\boldsymbol{\delta}$	:	Gimbal angle$(= (\delta_1, \delta_2, \delta_3, \delta_4)^T)$
δ_i	:	i^{th} gimbal angle
κ_1, κ_2	:	Jacobian matrice $\boldsymbol{C}$, $\boldsymbol{Q}$ condition numbers
$\boldsymbol{\omega}$	:	Spacecraft angular velocity $= (\omega_1, \omega_2, \omega_3)^T$

3.1 Introduction

A control moment gyroscope (CMG) produces an attitude control torque when the direction of the angular momentum of its rotating flywheel is changed by changing its gimbal angle. CMGs can produce a large torque and are therefore used on the International Space Station and other large spacecraft. They are of two basic types: one (SGCMGs) having a single gimbal axis per CMG unit; and the other (DGCMGs) having two. SGCMGs used for triaxial attitude control usually contain four or more CMG units, for redundancy. In particular, pyramid-type CMGs containing just four CMG units (Fig. 3.1) have been the subject of many studies on applicable steering control laws [1]$^-$ [20]. Even CMGs containing four CMG units encounter states of singularity, [21] in which they cannot produce torque in the required direction. Various steering control laws have been proposed for four-unit CMGs to avoid or escape from these singularities, including singularity-robust (SR) [6, 7], singular-direction avoidance (SDA) [8], null motion [12] and variable-speed (VS) CMGs [12–16] in combination as well as alone. Many pyramid-type CMGs employ a fixed skew angle β of 54.73 deg because the maximum angular momentum envelope is then nearly spherical, and this facilitates maintenance of three-dimensional isotropy in the angular momentum of the CMG system. With a variable skew angle, however, the envelope can be vertically and horizontally expanded and contracted, which may enable shorter attitude-change times. With this possibility in mind, an adaptive skew angle pyramid-type CMG (ASCMG) has been proposed, in which the skew angle is changed in advance in accordance with the attitude-change axis, and it has been shown that the attitude-change time can thereby be shortened [19]. The time required for the advance change was not included in the consideration, however, and the possibility therefore remained that a longer time might actually be required in cases involving a limit on the skew angle change speed. In this light, a modification of the concept was deemed necessary and the possibility of starting the change in skew angle concurrently with initiation of the attitude change rather than in advance was considered, and a steering control law that included the skew angle was proposed [20].

In the ASCMG system developed in the previous studies, the skew-angle control command value was disregarded and the stop was obtained by override when a limit angle was reached in the imposed skew-angle range of 10 to 80 deg [20] thus avoiding exceeding the skew-angle steering control limit command value. This method, however, involves a discontinuity in the rate of skew angle change and therefore carries the risk of placing an excessive load on the motor driving the skew angle. It is also possible that a difference might arise between the generated torque and the command torque, leading to an undesirably large change in attitude. During application of this method, chattering actually occurred in the skew angle movement [20]. A further problem that occurred was a tendency for overshoot to occur near completion of the attitude change, as described below in the results of the numerical simulation.

In the present study, a steering control law is proposed, which incorporates a smooth transfer from the ASCMG steering control law to the fixed skew angle steering control law on reaching the skew angle limit, to minimize the difference between the command torque and the generated torque. The proposed law in effect combines the off-diagonal SR (oDSR) [7] and local gradient methods [12,13]. To facilitate smooth transfer between the two steering control laws, the oDSR weighting gain varies with the skew angle. The local-gradient term is formulated to drive the gimbal in the direction yielding a Jacobian condition number of 1 including the skew angle. At the end of the attitude change, the skew angle is thereby brought close to its original value. This is desirable for performance of the next attitude change, which may need to be made about a different axis.

In this chapter, numerical simulations indicate that ASCMG yields shorter settling times than fixed skew angle CMG and reliably returns the skew angle to its original value at the end of the attitude change. It is also shown that the proposed steering control law, with its inclusion of the operating range, substantially reduces the level of overshoot from that encountered with a steering control law that does not include the range.

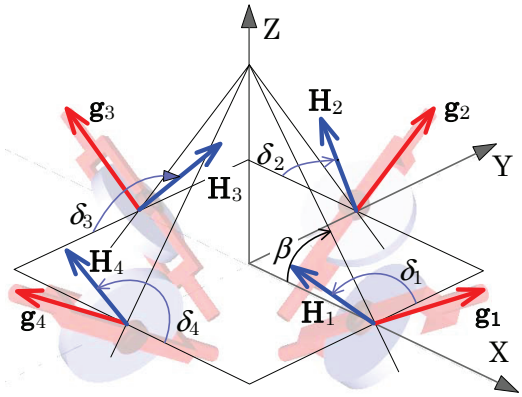

Figure 3.1: Pyramid array CMG.

3.2 ASCMG

In the usual pyramid-type CMG systems, the skew angle is fixed at 54.73 deg, so that the maximum angular momentum envelope is very nearly spherical.

The ASCMG discussed in this chapter, unlike ordinary fixed skew angle pyramid-type CMGs, deals with the angle of a gimbal with a controllable skew angle. It may be regarded as a DGCMG in terms of the number of gimbal axes per CMG unit, but the skew angles of all four of its CMG units can be changed simultaneously and it may therefore more appropriately be regarded as a system intermediate between an SGCMG and a DGCMG [19, 20].

Figure 3.2 shows an external view of the ASCMG constructed for experimental testing, and Fig. 3.3 shows the mechanism for effecting changes in skew angle. Each CMG unit contains gears on a quarter-circumference of a circle, which engage a worm gear located at the center of the system that is driven by a stepper motor to simultaneously change the skew angles of all four CMG units. The range of movement in this experimental system is limited to 10-80 deg, and the steering control law in the present study is formulated accordingly.

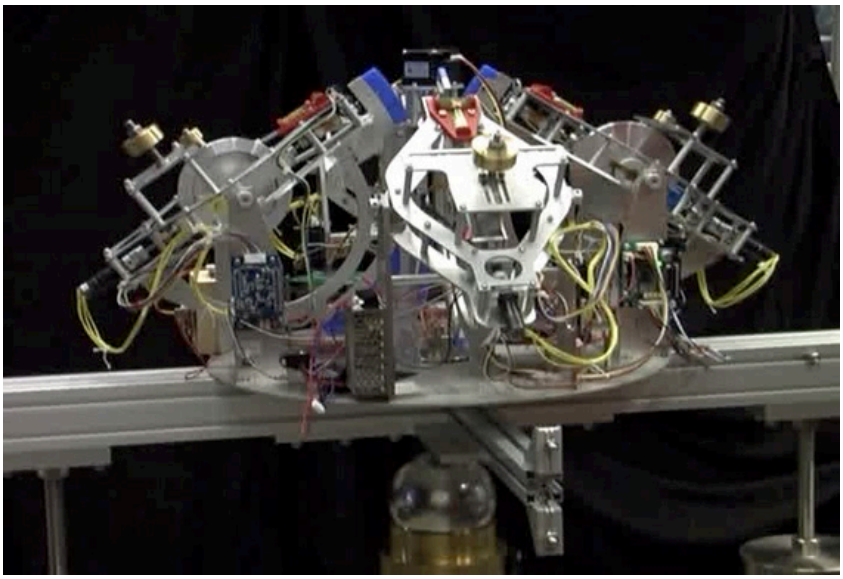

Figure 3.2: ASCMG.

3.3 Attitude Control Law

In this section, an explanation is given for quaternion feedback, which is often used to calculate the command torque for attitude changes.

3.3.1 Equations of motion

Assuming that the total angular momentum of the satellite including the CMG system is zero and further assuming the absence of any external torque, the movement of the satellite and the CMG system may be expressed as

$$\boldsymbol{J}\dot{\boldsymbol{\omega}} + \boldsymbol{\omega} \times \boldsymbol{J}\boldsymbol{\omega} = \boldsymbol{u} \,, \tag{3.1}$$

$$\dot{\boldsymbol{h}} + \boldsymbol{\omega} \times \boldsymbol{h} = -\boldsymbol{u} \tag{3.2}$$

where $\boldsymbol{u}$ is the command torque on the satellite, which is calculated as described below for the quaternion feedback control. To obtain the command torque of the CMG system, it is necessary to obtain the rate of change in angular momentum held by that system, as

$$\dot{\boldsymbol{h}} = -\boldsymbol{u} - \boldsymbol{\omega} \times \boldsymbol{h} \,. \tag{3.3}$$

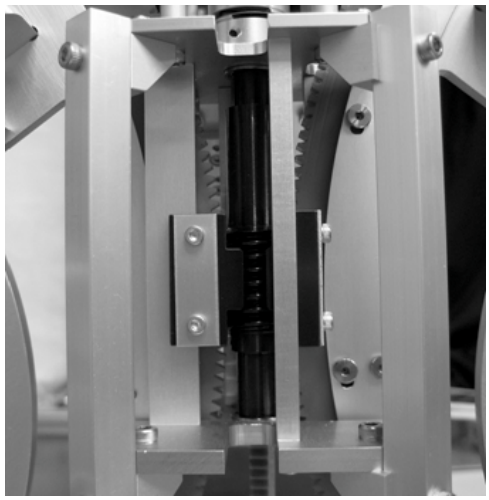

Figure 3.3: Mechanism for controlling skew angle.

3.3.2 Quaternion feedback control law

quaternion feedback control law quaternion $\boldsymbol{q}(= (q_1, q_2, q_3, q_4)^T = (\hat{\boldsymbol{q}}^T, q_4)^T)$ is given by

$$\boldsymbol{q} = \begin{bmatrix} \hat{\boldsymbol{q}} \\ q_4 \end{bmatrix} = \begin{bmatrix} \hat{\boldsymbol{e}} \sin(\varphi/2) \\ \cos(\varphi/2) \end{bmatrix} \tag{3.4}$$

where $\hat{\boldsymbol{e}}$ is the common axis of rotation and φ is the angle of rotation about that axis. The direction cosine matrix $\boldsymbol{R}$, which shows the attitude conversion from the inertial coordinate system to the satellite body coordinate system using the quaternion, is expressed as

$$\boldsymbol{R} = \begin{bmatrix} 1-2(q_2^2+q_3^2) & 2(q_1q_2+q_3q_4) & 2(q_1q_3-q_2q_4) \\ 2(q_1q_2-q_3q_4) & 1-2(q_1^2+q_3^2) & 2(q_2q_3+q_1q_4) \\ 2(q_1q_3+q_2q_4) & 2(q_2q_3-q_1q_4) & 1-2(q_1^2+q_2^2) \end{bmatrix}. \tag{3.5}$$

Using the angular velocity of the satellite, the quaternion differential equation is given as

$$\dot{\boldsymbol{q}} = \frac{1}{2} \begin{bmatrix} q_4\boldsymbol{\omega} - \boldsymbol{\omega} \times \hat{\boldsymbol{q}} \\ -\boldsymbol{\omega}^T \hat{\boldsymbol{q}} \end{bmatrix}. \tag{3.6}$$

In the present study, for simplicity, the target attitude is given throughout in the inertial coordinate system. For the quaternion feedback control [22], the quaternion expressing

the attitude angle error and the satellite angular velocity are multiplied by their respective gains to obtain the command torque using the following control equation, which thus resembles PD control.

$$\boldsymbol{u} = -\boldsymbol{K}_p\hat{\boldsymbol{q}} - \boldsymbol{K}_d\boldsymbol{\omega} \tag{3.7}$$

3.4 Steering Control Laws for the Fixed Skew Angle CMG

In this section, the steering control laws for fixed skew angle CMGs are first described as a reference base for the discussion of the ASCMG steering control law. The Jacobian matrix $\boldsymbol{C}$ for fixed skew angle CMGs can be written as

$$\boldsymbol{C} = \begin{bmatrix} -c\beta\cos\delta_1 & \sin\delta_2 & c\beta\cos\delta_3 & -\sin\delta_4 \\ -\sin\delta_1 & -c\beta\cos\delta_2 & \sin\delta_3 & c\beta\cos\delta_4 \\ s\beta\cos\delta_1 & s\beta\cos\delta_2 & s\beta\cos\delta_3 & s\beta\cos\delta_4 \end{bmatrix} . \tag{3.8}$$

3.4.1 off-Diagonal SR inverse (oDSR)

The oDSR steering control law [7] can be expressed as

$$\dot{\boldsymbol{\delta}} = \boldsymbol{W}\boldsymbol{C}^T\left[\boldsymbol{C}\boldsymbol{W}\boldsymbol{C}^T + \lambda\boldsymbol{E}\right]^{-1}(\dot{\boldsymbol{h}}/h_0) \tag{3.9}$$

where

$$\boldsymbol{W} = \begin{bmatrix} W_1 & \lambda & \lambda & \lambda \\ \lambda & W_2 & \lambda & \lambda \\ \lambda & \lambda & W_3 & \lambda \\ \lambda & \lambda & \lambda & W_4 \end{bmatrix} > 0 , \tag{3.10}$$

$$\boldsymbol{E} = \begin{bmatrix} 1 & \epsilon_3 & \epsilon_2 \\ \epsilon_3 & 1 & \epsilon_1 \\ \epsilon_2 & \epsilon_1 & 1 \end{bmatrix} , \tag{3.11}$$

and λ and ϵ_i are given as follows, using small-valued $\lambda_0 > 0$ and $\epsilon_0 > 0$ to avoid generation of large perturbation torques by λ and ϵ_i.

$$\lambda = \lambda_0 \exp(-\mu \det(\boldsymbol{C}\boldsymbol{C}^T)), \quad \mu > 0 \,, \tag{3.12}$$

$$\epsilon_i = \epsilon_0 \sin(\omega t + \phi_i) \tag{3.13}$$

where ω and ϕ_i are the angular frequency and phase used to apply the time-dependent perturbation.

3.4.2 oDSR-LG steering control law

The steering control law oDSR-LG combines the methods of the oDSR and the local gradient (null motion). This control law is given by

$$\dot{\boldsymbol{\delta}} = \boldsymbol{W}\boldsymbol{C}^T(\boldsymbol{C}\boldsymbol{W}\boldsymbol{C}^T + \lambda \boldsymbol{E})^{-1}(\dot{\boldsymbol{h}}/h_0) + \left[\boldsymbol{I}_4 - \boldsymbol{C}^T(\boldsymbol{C}\boldsymbol{C}^T)^{-1}\boldsymbol{C}\right]\boldsymbol{d}_1 \,. \tag{3.14}$$

The second term is the null motion term, with $\boldsymbol{d}_1$ representing an arbitrary vector. This vector must be appropriately selected for effective avoidance of singularities, and the steering method is chosen to obtain steering control that maintains the steering direction that keeps the condition number as close as possible to 1. With κ_1 as the Jacobian matrix $\boldsymbol{C}$ condition number, $\boldsymbol{d}_1$ is therefore selected by

$$\boldsymbol{d}_1 = -k\left(\frac{\partial \kappa_1}{\partial \boldsymbol{\delta}}\right)^T, \quad k > 0 \,. \tag{3.15}$$

3.5 ASCMG Steering Control Law

The ASCMG Jacobian matrix $\boldsymbol{Q}$ is given by

$$\boldsymbol{Q} = [\boldsymbol{C}, \boldsymbol{D}] \tag{3.16}$$

where

$$\boldsymbol{D} = \begin{bmatrix} (\sin\delta_1 - \sin\delta_3)\, s\beta \\ (\sin\delta_2 - \sin\delta_4)\, s\beta \\ (\sin\delta_1 + \sin\delta_2 + \sin\delta_3 + \sin\delta_4)\, c\beta \end{bmatrix} . \tag{3.17}$$

The steering control law constructed specifically for the ASCMG is described. In this description, a fixed skew angle CMG steering control law is used as a basis of reference.

3.5.1 AS-oDSR law

The oDSR for the ASCMG (the adaptive-skew oDSR) contains one more dimension than the fixed-skew oDSR, and is expressed as

$$\begin{bmatrix} \dot{\boldsymbol{\delta}} \\ \dot{\beta} \end{bmatrix} = \boldsymbol{W}\boldsymbol{Q}^T \left(\boldsymbol{Q}\boldsymbol{W}\boldsymbol{Q}^T + \lambda \boldsymbol{E}\right)^{-1} (\dot{\boldsymbol{h}}/h_0) \tag{3.18}$$

where the weighting matrix is

$$\boldsymbol{W} = \begin{bmatrix} W_1 & \lambda & \lambda & \lambda & \lambda \\ \lambda & W_2 & \lambda & \lambda & \lambda \\ \lambda & \lambda & W_3 & \lambda & \lambda \\ \lambda & \lambda & \lambda & W_4 & \lambda \\ \lambda & \lambda & \lambda & \lambda & W_5 \end{bmatrix} > 0\,. \tag{3.19}$$

3.5.2 AS-oDSR-LG

This steering law combines the oDSR for the ASCMG and the local gradient method, and is written as

$$\begin{bmatrix} \dot{\boldsymbol{\delta}} \\ \dot{\beta} \end{bmatrix} = \boldsymbol{W}\boldsymbol{Q}^T(\boldsymbol{Q}\boldsymbol{W}\boldsymbol{Q}^T + \lambda \boldsymbol{E})^{-1}(\dot{\boldsymbol{h}}/h_0) + \left[\boldsymbol{I}_5 - \tilde{\boldsymbol{W}}\boldsymbol{Q}^T \left(\boldsymbol{Q}\tilde{\boldsymbol{W}}\boldsymbol{Q}^T\right)^{-1} \boldsymbol{Q}\right] \tilde{\boldsymbol{W}}\boldsymbol{d}_2 \tag{3.20}$$

where $\tilde{\boldsymbol{W}}$ is the weighting matrix which positions null motion between the gimbal and the skew angle, and $\boldsymbol{d}_2$ is chosen while referring to the case of the fixed skew angle CMG, taking into account the skew angle changeability, as

$$\boldsymbol{d}_2 = -k \begin{bmatrix} \left(\dfrac{\partial \kappa_2}{\partial \boldsymbol{\delta}}\right)^T \\ \left(\dfrac{\partial \kappa_2}{\partial \beta}\right) \end{bmatrix}, \quad k > 0 \tag{3.21}$$

where κ_2 is the condition number of Jacobian matrix $\boldsymbol{Q}$.

3.5.3 GS-ASoDSR-LG

This gain-scheduled steering control law is designed to ensure smooth transfer from the ASCMG to fixed steering control CMG. The previous system included an override that brought the rate of skew angle change to zero when the skew angle reached the system's mechanical limit, to eliminate the possibility that the skew angle change would continue beyond that limit. This override, however, raised concern that it might result in a difference between the torque produced by the CMG and the command torque and thus prevent achievement of the desired attitude movement. To overcome this, a means of varying the weighting in correspondence with the skew angle was considered, for smooth transfer

For this purpose, in the present study, the AS-oDSR weighting matrix W_5 is formulated as the following function, which generates a curve resembling an inverted bathtub in correspondence with the skew angle:

$$W_5 = \frac{1}{1 + e^{-a(\beta - \beta_{\min} - \epsilon)}} \cdot \frac{1}{1 + e^{a(\beta - \beta_{\max} + \epsilon)}} \tag{3.22}$$

where, $a > 0$, and ϵ is a small positive constant that begins to weaken the skew angle function just before arrival at the limit angle. As illustrated by the example in Fig. 3.4, the W_5 weighting value approaches zero as the skew angle approaches the limit angle, and the torque generating function of the skew angle thereby loses effect.

3.6 Numerical Simulation

An example of 180 deg rotation about the x-axis is considered. The values used in the numerical simulation are listed in Table 3.1.

The simulation results in terms of gimbal-angle and satellite body-attitude history are shown in Figs. 3.5 with oDSR-LG and Fig. 3.6 with oDSR for the fixed skew angle CMG, and in Figs. 3.7 with AS-oDSR and Fig. 3.8 with AS-oDSR-LG for the ASCMG.

With oDSR, the CMG angular momentum remains at an internal singularity for about 5 s starting from about 5 s. To avoid this singularity, it produces a torque per-

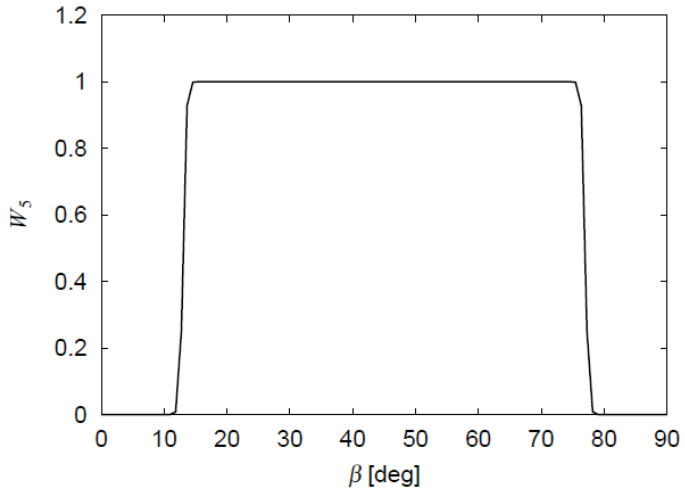

Figure 3.4: Example of W_5 for gain scheduled control.

turbation about the satellite body axis in the direction of the y- or z-axis, which results in the generation of small irregular fluctuations in the satellite attitude about the y-axis or z-axis. It then reaches angular momentum saturation at about 15 s, and escapes at about 58 s. With the oDSR-LG, after remaining at the internal singularity, the occurrence of competition between the oDSR and the local gradient method results in an inability to escape. With the AS-oDSR and AS-oDSR-LG, the skew angle moves below the initial angle to increase the satellite angular velocity about the x-axis until it reaches the minimum angle limit (10 deg). On reaching angular momentum saturation near 10 s, to avoid a singularity the skew angle departs from the minimum angle limit temporarily, but then returns to it. This is followed, near 40 s with the AS-oDSR and near 23 s with AS-oDSR-LG, by departure from the minimum angle limit that leads to arrival at the maximum angle limit. This occurs because the increase in the skew angle decreases the CMG angular momentum in the direction of the x-axis and causes earlier angular velocity deceleration. With the AS-oDSR-LG, the attitude perturbation about the y- and z-axes is smaller than with other methods, as an effect of the attempt by null motion to avoid the singularity. With AS-oDSR-LG, the angular velocity of approach to

Table 3.1: Simulation parameters.

Parameters	Values	Units
$\boldsymbol{\delta}(0)$	[0, 0, 0, 0]	rad
$\dot{\boldsymbol{\delta}}(0)$	[0, 0, 0, 0]	rad/s
$\beta(0)$	54.73	deg
$\beta_{\min}$, $\beta_{\max}$	10, 80	deg
h_0	0.044	Nms
$\boldsymbol{J}$	diag(2.5, 0.65, 1.11)	kgm^2
k	0.00008	
$\boldsymbol{K}_p$	0.09 $\boldsymbol{I}_3$	Nms
$\boldsymbol{K}_d$	0.4242 $\boldsymbol{I}_3$	Nms/(rad/s)
λ_0,μ	0.01, 10	
ϵ_0, ω	0.01, 0.5	
ϕ_i	$0, \pi/2, \pi$	
W_i	1, 1, 2, 3, 1	
$\tilde{\boldsymbol{W}}$	diag(1, 1, 1, 1, 100)	
a	$7 \sim 90$	
ϵ	0.05, 0.01, 0.005, 0.001	

the end attitude is high and leads to overshoot. The overshoot is smaller, however, than the overshoot that occurs with the AS-oDSR even though the angular velocity of the approach to the end attitude with the AS-oDSR is lower than with AS-oDSR-LG. The overshoot occurs because, with the skew angle already at the maximum angle limit, no command attenuation torque can actually be produced despite issuance of the command under the steering control law to increase the skew angle and thus produce the torque needed to attenuate the angular velocity.

Table 3.2 outlines the gain-scheduled GS-AS-oDSR-LG property dependence on parameters a and ϵ of the weighting function W_5. Figures 3.9 to 3.12 show the gain-

scheduled properties found with four pairs of parameter values ((a = 10, ϵ = 0.05), (a = 7, ϵ = 0.005), (a = 30, ϵ = 0.005), and (a = 90, ϵ = 0.005)) that yield very large property differences. If ϵ is larger than 0.05 in the weighting function W_5 for the GS-AS-oDSR-LG, the range of skew angles that can be utilized to activate the ASCMG mode narrows and in many cases the gain-scheduled property function is lost. As can be seen from Table 3.2, with the value of ϵ at 0.05, the range of a values for which the gain-scheduled properties cannot be utilized is quite large. Even with a = 10, which permits utilization of the gain-scheduled properties, near 63 s and 93 s, it crosses gimbal angles for which, as shown by the example in Fig. 3.9, functional utilization as an ordinary CMG is difficult because the operation is approaching condition number 1 and the steering command to return to the former angle has been issued, and a discontinuity occurs in the skew angle steering, with the result that the skew angle does not stabilize. In the example shown in Fig. 3.8, on the other hand, the gimbal angle crosses the angles at which it is difficult for the gimbal angle to function as a CMG before attitude settlement. Settlement is therefore achieved at a specific angle, and is free from discontinuous changes in skew angle because of the deceleration torque accompanying the change in skew angle. The tendencies were found to arise in GS-AS-oDR-LG with ϵ values larger than 0.05. An ϵ value less than or equal to 0.05 is therefore deemed desirable for effective utilization of the gain-scheduled properties.

The changes that occur in the gain-scheduled properties when a is varied, with ϵ at 0.005 are next described. With small values of a, the shape of the weighting function W_5 becomes more trapezoidal than in Fig. 3.4. With large values of a, it becomes more rectangular. When we set a = 7, thus going below the value of 10, then as shown in Fig. 3.10, the gain-scheduled properties are not lost. However, it appears that attenuation torque generation is dependent on the change in the gimbal angle rather than the skew angle and, for the same reasons as in Fig. 3.9, a discontinuity occurs for skew angle changes near 63 s and 93 s, during the end stage of attitude settlement. Further reduction in the value of a results in loss of the gain-scheduled properties.

With a at about 30, in contrast, as shown in Fig. 3.11, the gain-scheduled properties

Table 3.2: Properties of GS-AS-oDSR-LG with respect to a and ϵ.

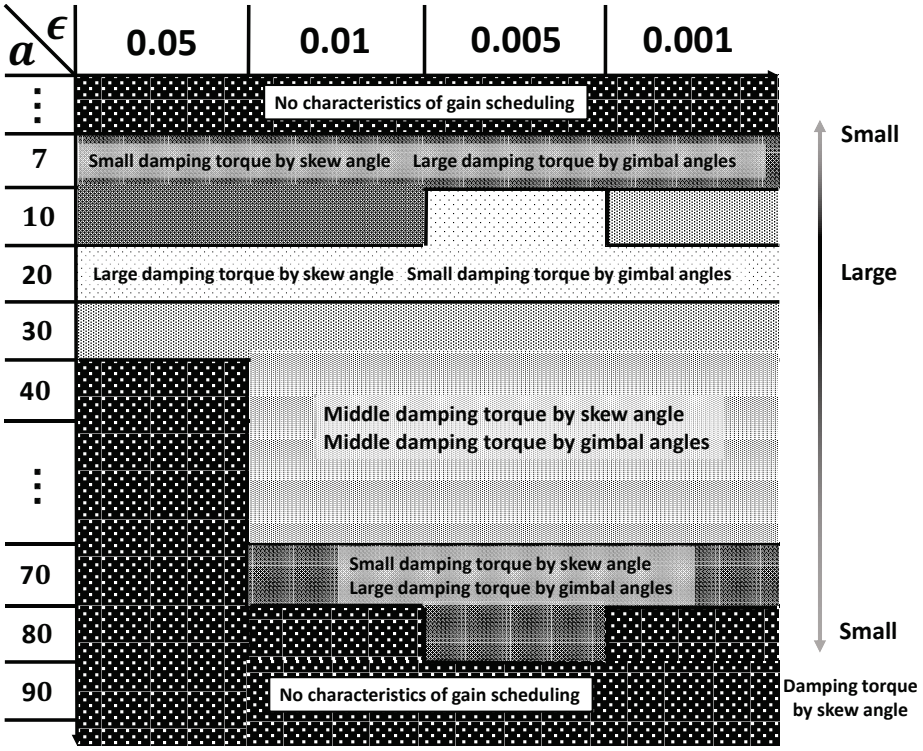

are not lost and the skew-angle change and gimbal-angle change are effectively utilized to produce the attenuation torque and reduce overshoot. Figure 3.11 shows the results with the parameters in the range in which the gain-scheduled properties can be most effectively utilized. The results confirm that in the end stage of the attitude change the gimbal angle tends to approach zero and the skew angle tends to return toward the original angular direction. This is desirable whenever the next attitude change is to be performed about an axis different from the first attitude change axis (in this example, the x-axis). The closer the skew angle is to its original value, the closer the Jacobian matrix condition number is to 1, and the null motion term based on the local gradient method tends to bring the condition number to 1. If a is further increased, as shown for the large value of $a = 90$ in Fig. 3.12, the gain-scheduled properties are again lost and it is evident that, as with AS-oDSR-LG, it becomes impossible to generate sufficient

attenuation torque based on the gimbal angle alone without depending on the change in skew angle, and overshoot therefore occurs. Table 3.3 is a summary of the observed settling times. It shows that the settling times with the AS-oDSR-LG and GS-AS-oDSR-LG are both shorter than that with the fixed skew angle CMG.

Consequently, the results show that with appropriate parameter selection, the steering control law in a gain-scheduled ASCMG with null motion (GS-AS-oDSR-LG), as compared with fixed skew angle CMG steering control, results in less attitude perturbation in early- and middle-stage of maneuver, a shorter settling time, and the same degree of overshoot reduction in the end-stage of maneuver, and further that it tends to return the skew angle to its original value.

Table 3.3: Comparison of settling times.

Controller		Settling Time [s]
oDSR		95.12
oDSR-LG		-
AS-oDSR		122.24
AS-oDSR-LG		81.38
GS-AS-oDSR-LG	(a=10, ϵ=0.05)	81.88
	(a=7, ϵ=0.005)	81.88
	(a=30, ϵ=0.005)	81.54
	(a=90, ϵ=0.005)	88.46

3.7 Conclusion

In this chapter, cases were considered in which the change in skew angle begins at the time of attitude change initiation and a steering control law incorporating the skew angle was proposed. The law combines the oDSR and local gradient methods. With consideration given to the limits in the range of skew-angle operation, the oDSR weighting gain varies with skew angle, and a method is given for smooth transfer from ASCMG steering control to fixed skew angle steering control. The results of numerical simulations show that the ASCMG yields a shorter settling time and less attitude perturbation than the fixed skew angle CMG, and that the skew angle reliably returns to its original value at the end of the attitude change.

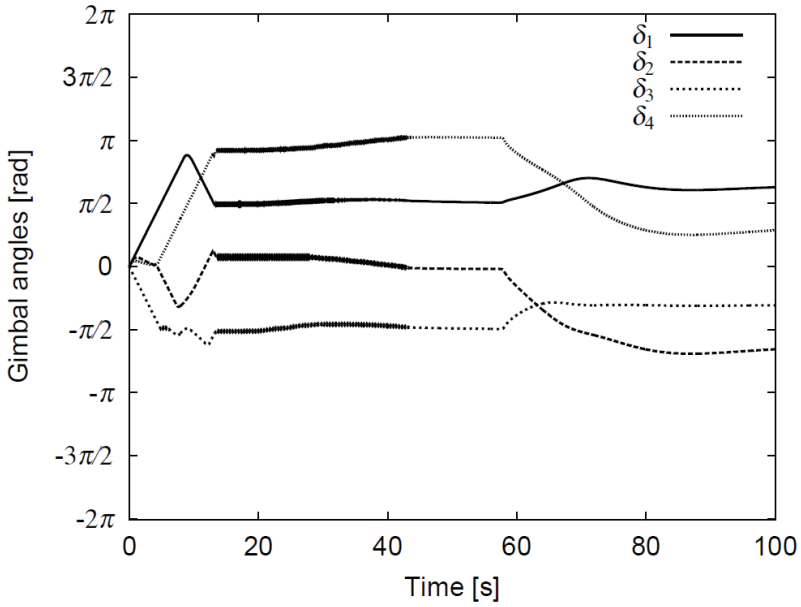

Gimbal angles

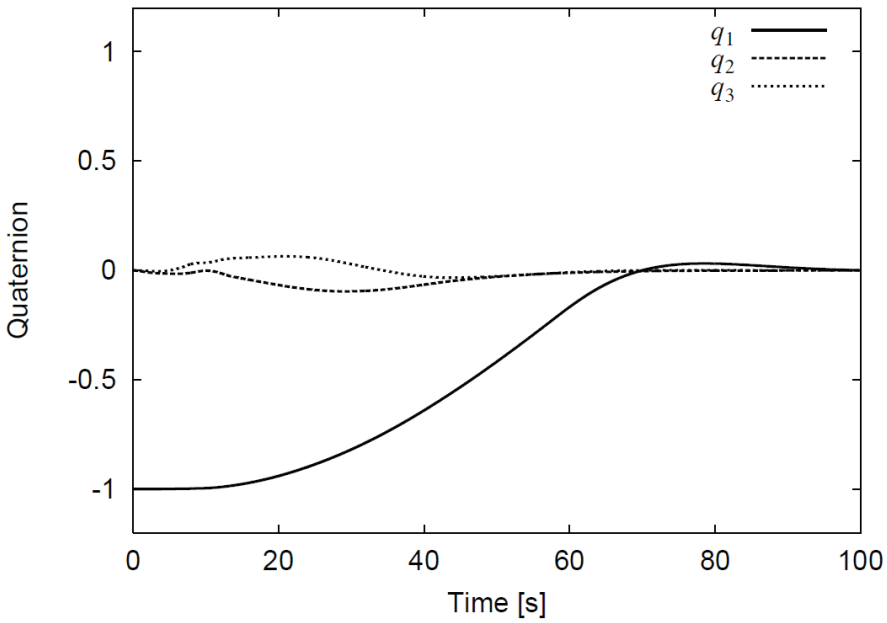

Quaternion

Figure 3.5: Result for oDSR.

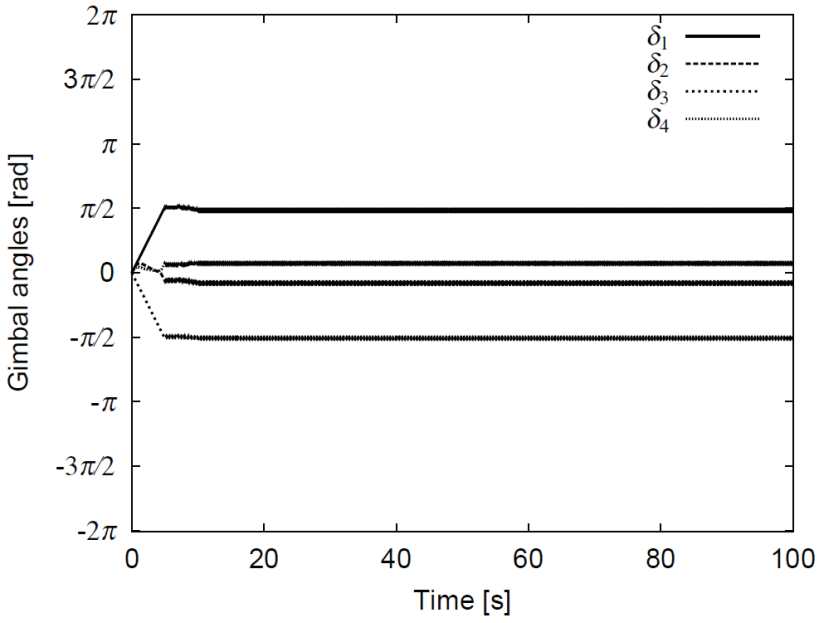

Gimbal angles

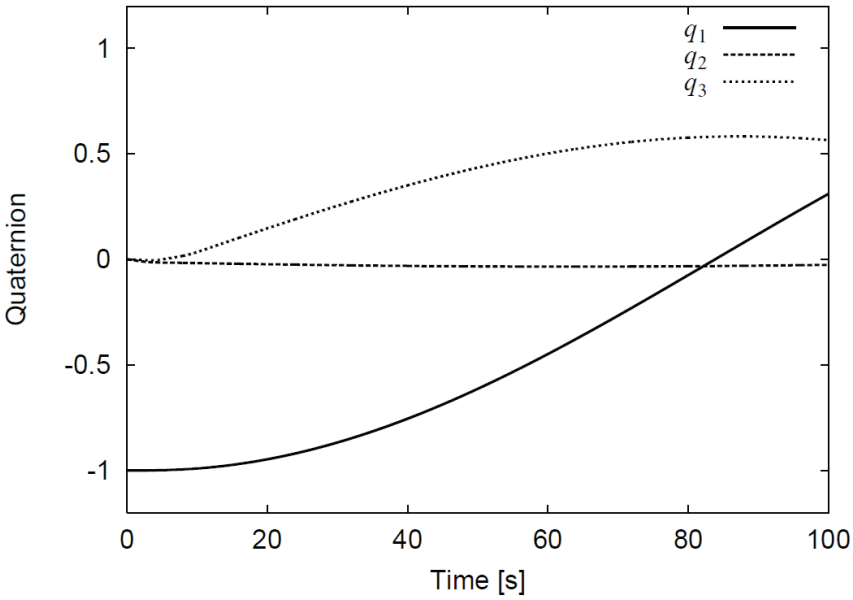

Quaternion

Figure 3.6: Result for oDSR-LG.

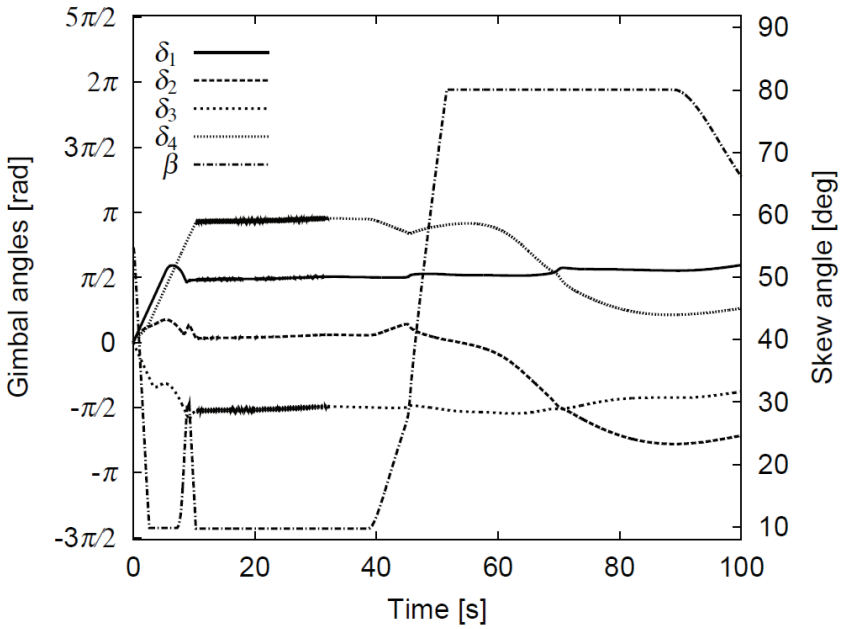

Gimbal angles

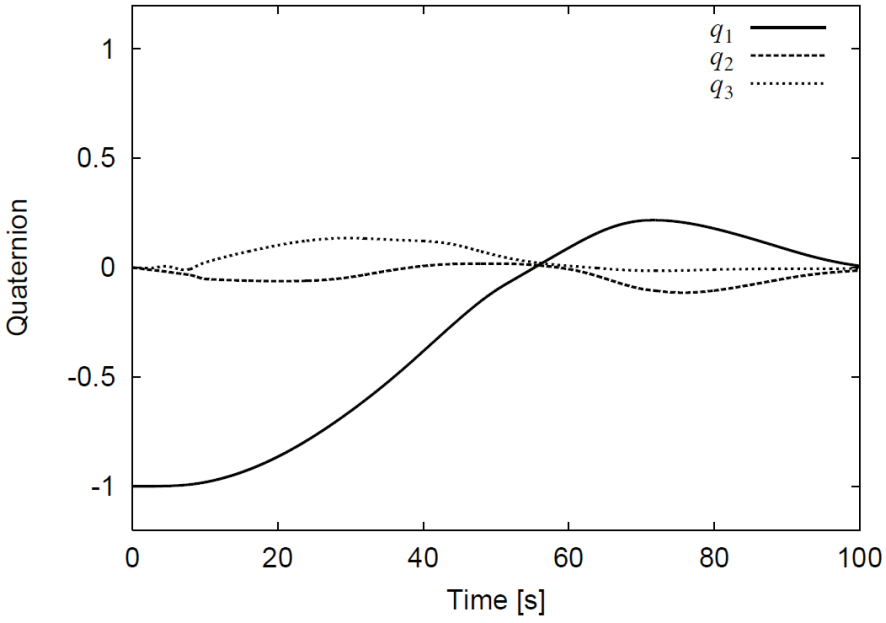

Quaternion

Figure 3.7: Result for AS-oDSR.

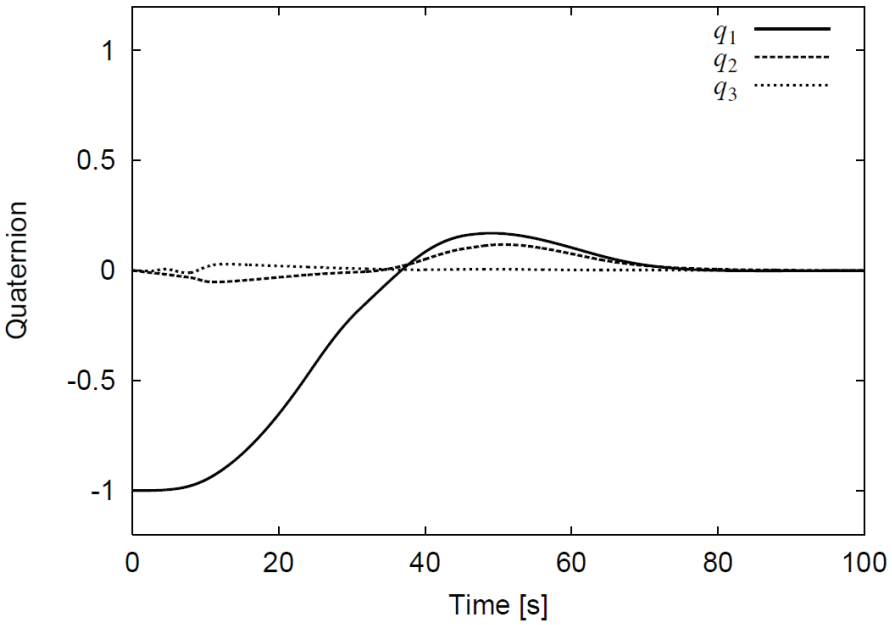

Gimbal angles

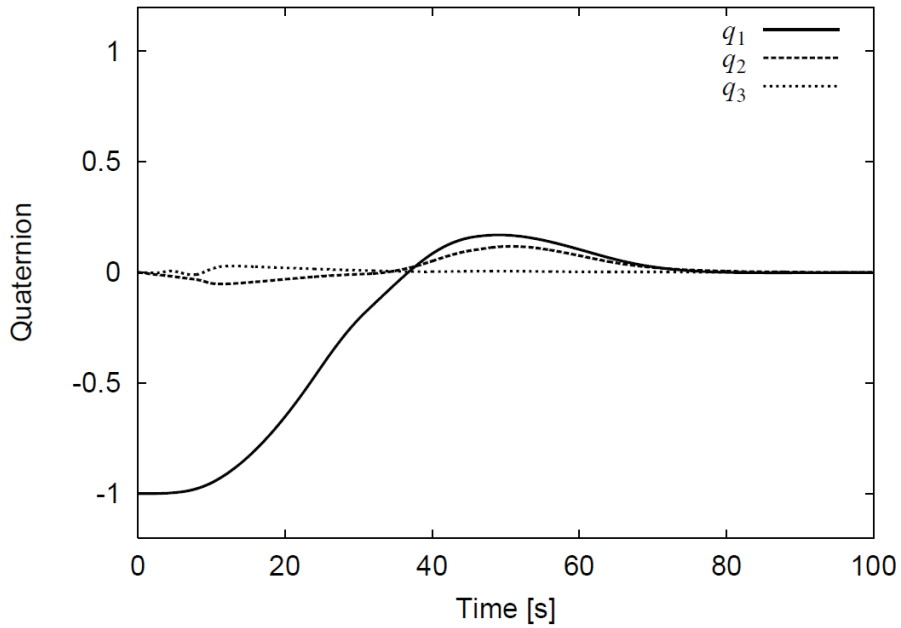

Quaternion

Figure 3.8: Result for AS-oDSR-LG.

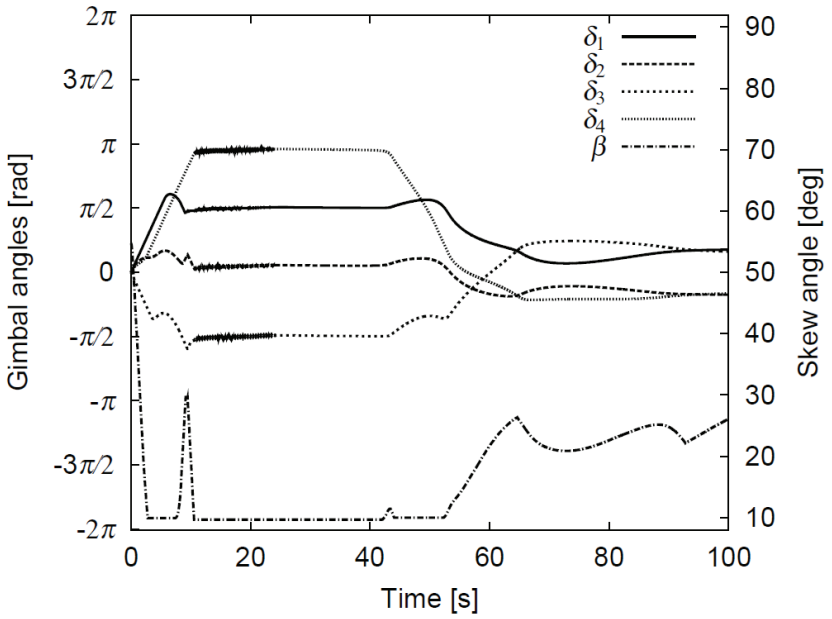

Gimbal angles

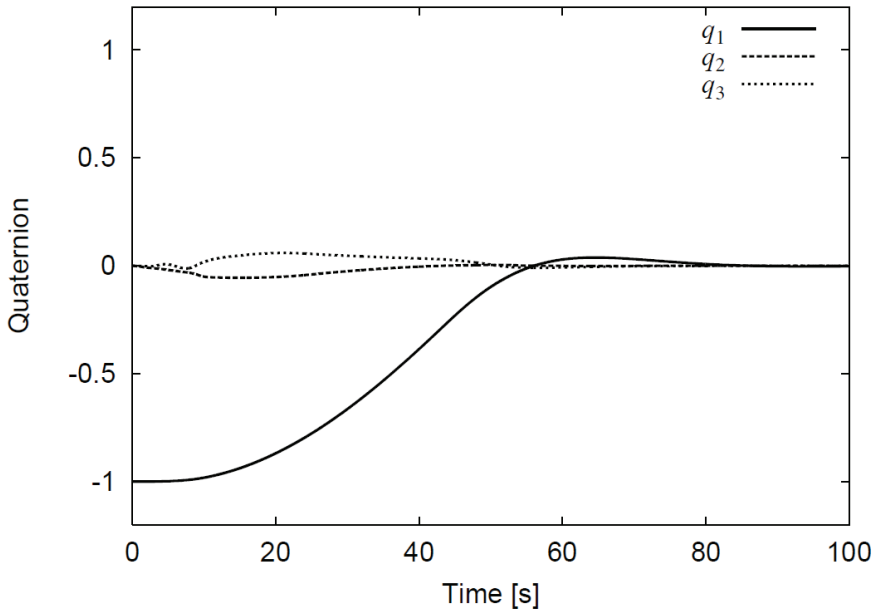

Quaternion

Figure 3.9: Result for GS-AS-oDSR-LG(a=10, ϵ=0.05).

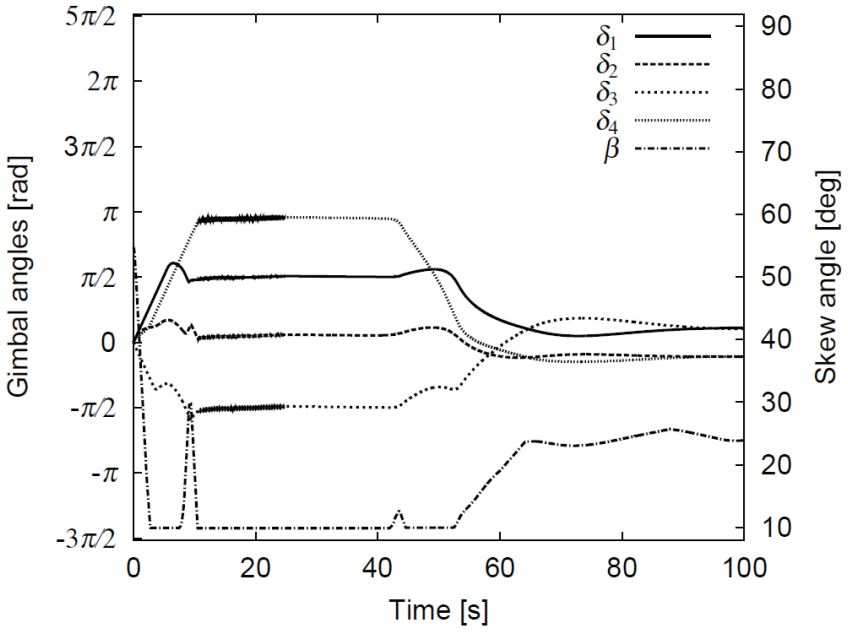

Gimbal angles

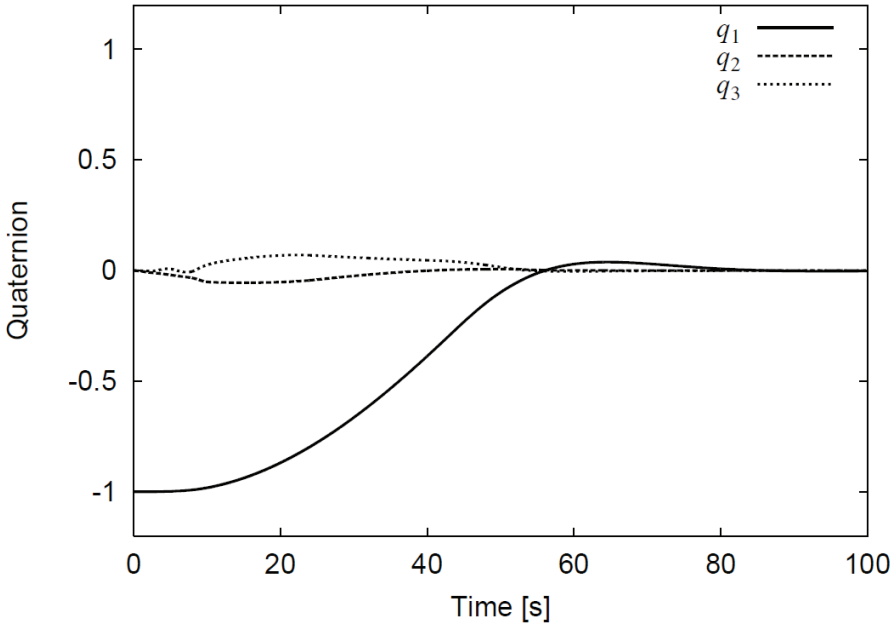

Quaternion

Figure 3.10: Result for GS-AS-oDSR-LG(a=7, ϵ=0.005).

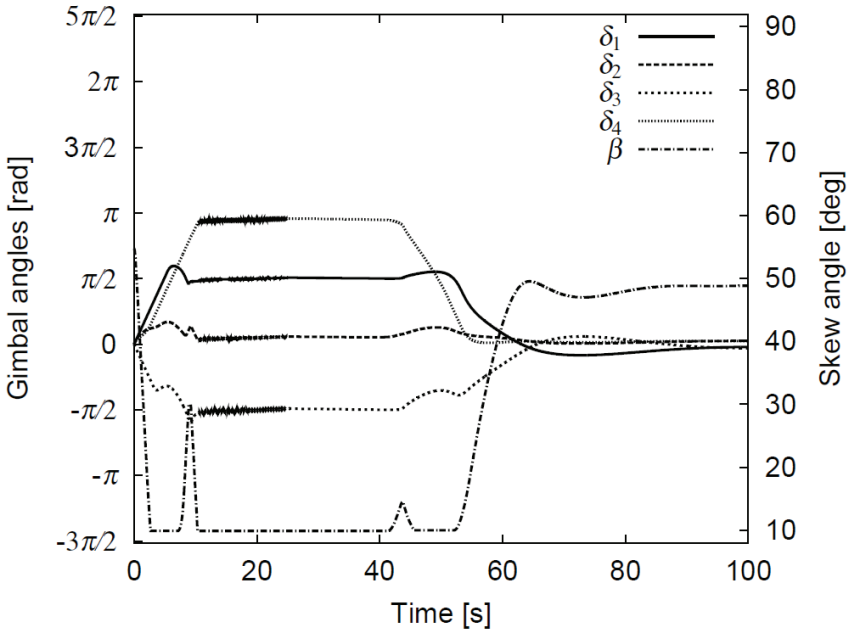

Gimbal angles

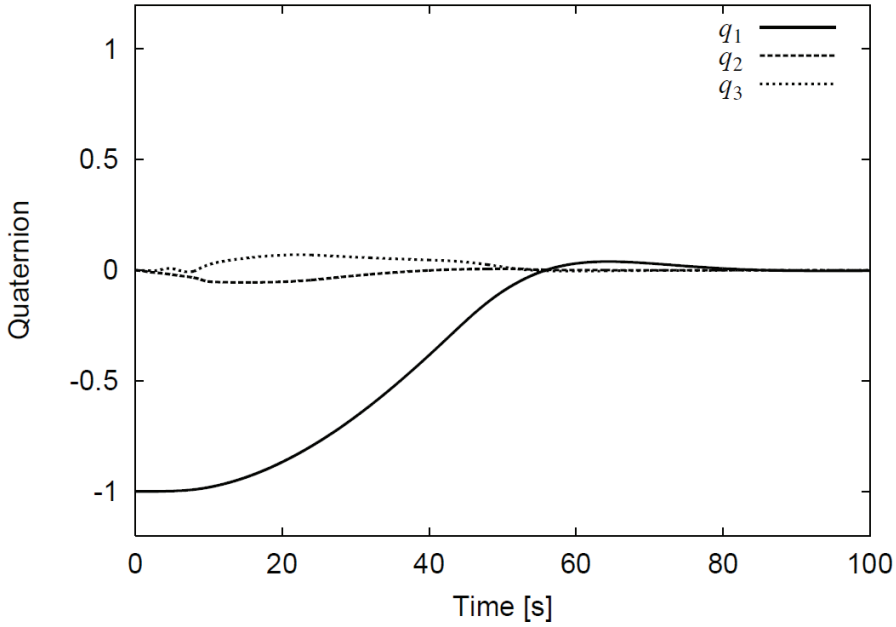

Quaternion

Figure 3.11: Result for GS-AS-oDSR-LG(a=30, ϵ=0.005).

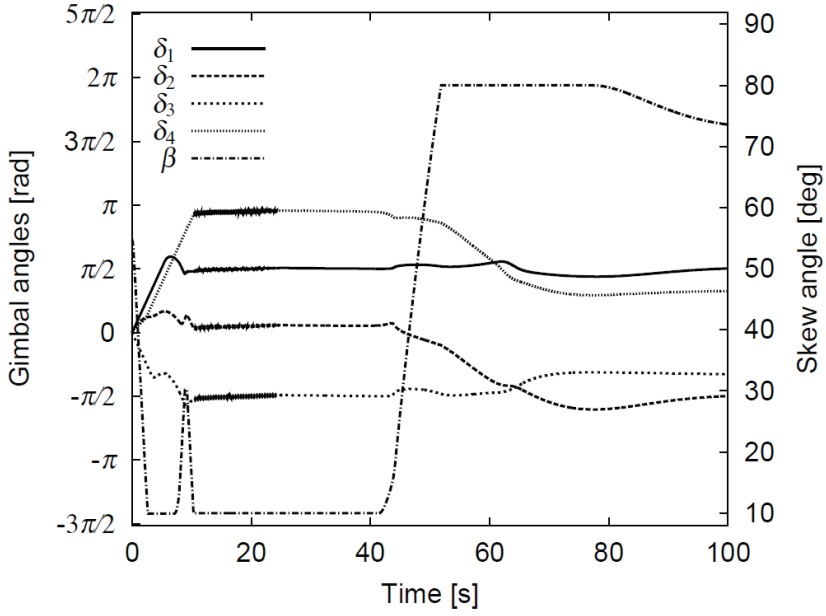

Gimbal angles

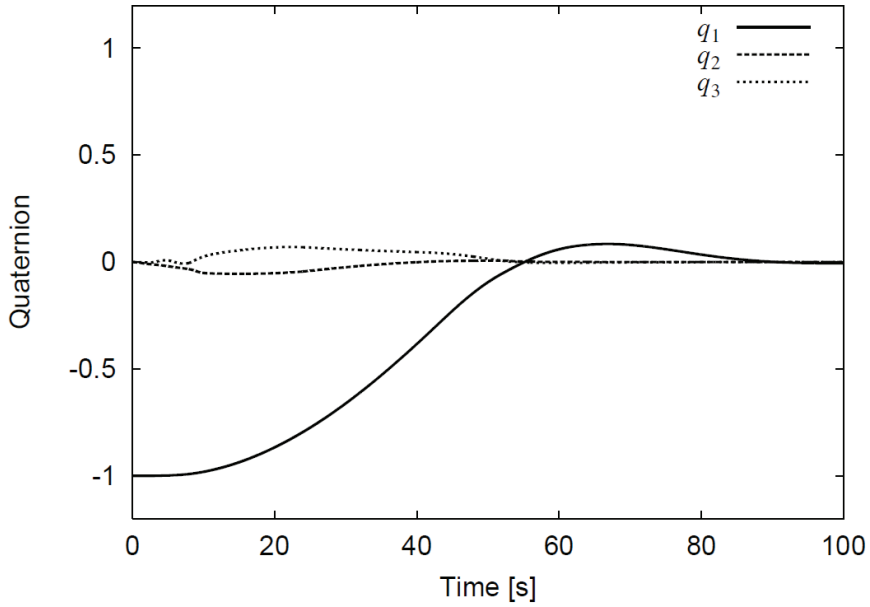

Quaternion

Figure 3.12: Result for GS-AS-oDSR-LG(a=90, ϵ=0.005).

References

[1] Kurokawa, H.: A Geometric Study of Single Gimbal Control Moment Gyros - Singularity Problems and Steering Law, Tech. Rep. Report, Mechanical Engineering Laboratory, Japan, No.175, Jan., 1998.

[2] Vadali, S. R., Oh, H. S. and Walker, S. R.: Preferred Gimbal Angles for Single Gimbal Control Moment Gyros, *Journal of Guidabce, Control, and Dynamics*, **13**(1990), pp.1090-1095.

[3] Paradiso, J. A.: Global Steering of Single Gimbaled Control Moment Gyroscopes using a Directed Search, *Journal of Guidabce, Control, and Dynamics*, **15**(1992), pp.1236-1244.

[4] Fleming, A. and Ross, I. M.: Singularity-Free Optimal Steering of Control Moment Gyros, *Advances in the Astronautical Sciences*, Vol.123-III(2006), pp.2681-2700.

[5] Bedrossian, N. S., Paradiso, J., Bergmann, E. V. and Rowell, D.: Steering Law Design for Redundant Single-Gimbal Control Moment Gyroscopes, *Journal of Guidabce, Control, and Dynamics*, **13**(1990), pp.1083-1089.

[6] Wie, B., Bailey, D. and Heiberg, C. J.: Singularity Robust Steering Logic for Redundant Single-gimbal Control Moment Gyros, *Journal of Guidabce, Control, and Dynamics*, **24**(2001), pp.865-872.

[7] Wie, B.: Singularity Escape/Avoidance Steering Logic for Control Moment Gyro Systems, *Journal of Guidabce, Control, and Dynamics*, **28**(2005), pp.948-956.

[8] Ford, K. A. and Hall, C. D.: Singular Direction Avoidance Steering for Control-Moment Gyros, *Journal of Guidabce, Control, and Dynamics*, **23**(2000), pp.648-656.

[9] Bedrossian, N. S., Paradiso, J., Bergmann, E. V. and Rowell, D.: Redundant Single Gimbal Control Moment Gyroscope Singularity Analysis, *Journal of Guidabce, Control, and Dynamics*, **13**(1990), pp.1096-1101.

[10] Kurokawa, H.: Constrained Steering Law of Pyramid-Type Control Moment Gyros and Ground Tests, *Journal of Guidabce, Control, and Dynamics*, **20**(1997), pp.445-449.

[11] Kurokawa, H.: Survey of Theory and Steering Laws of Single-Gimbal Control Moment Gyros, *Journal of Guidabce, Control, and Dynamics*, **30**(2007), pp.1331-1340.

[12] McMahon, J. and Schaub, H.: Simplified Singularity Avoidance Using Variable-Speed Control Moment Gyroscope Null Motion, *Journal of Guidabce, Control, and Dynamics*, **32**(2009), pp.1938-1943.

[13] Schaub, H. and Junkins, J. L.: Singularity Avoidance Using Null Motion and Variable-Speed Control Moment Gyros, *Journal of Guidabce, Control, and Dynamics*, **23**(2000), pp.11-16.

[14] Yoon, H. and Tsiotras, P.: Singularity Analysis and Avoidance of Variable-Speed Control Moment Gyros, *Journal of Guidabce, Control, and Dynamics*, **27**(2004), pp.374-386.

[15] Yoon, H. and Tsiotras, P.: Spacecraft Line-of-Sight Control Using a Single Variable-Speed Control Moment Gyro, *Journal of Guidabce, Control, and Dynamics*, **29**(2006), pp.1295-1308.

[16] Yoon, H. and Tsiotras, P.: Spacecraft Adaptive Attitude and Power Tracking with Variable Speed Control Moment Gyroscopes, *Journal of Guidabce, Control, and Dynamics*, **25**(2002), pp.1081-1090.

[17] Takada, K. and Kojima, H.: Receding Horizon Control on Steering of Control Moment Gyro for Fast Attitude Maneuver, *Transactions of the Japan Society for Aeronautical and Space Sciences*, **52**(2009), pp.1-10.

[18] Takada, K., Kojima, H. and Matsuda, N.: Control Moment Gyro Singularity-Avoidance Steering Control Based on Singular-Surface Cost Function, *Journal of Guidabce, Control, and Dynamics*, **33**(2010), pp.1442-1450.

[19] Kojima, H., Matsuda, N. and Takada, K.: Adaptive Skewing Pyramid-type CMGs for Fast Attitude Maneuver, *Transactions of the Japan Society for Aeronautical and Space Sciences, Space Technology Japan*, **7**(2009), pp.19-24.

[20] Kojima, H.: Singularity Visualization and Steering Control Law for Adaptive-skew Pyramid-type CMG, *Acta Astronautica*, **85**(2013), pp.120-137.

[21] Margulies, G. and Aubrun, J.N.: Geometric Theory of Single-Gimbal Control Moment Gyro System, *Journal of Astronautical Sciences*, **26**(1978), pp.159-191.

[22] Wie, B.: Space Vehicle Dynamics and Control, 2nd Edition, AIAA Education Series, American Institute of Aeronautics and Astronautics, Inc. 2008.

Chapter 4

LMI-based Control Law for Variable-Speed Control Moment Gyros in Flexible Spacecraft

Nomenclature

$\boldsymbol{C}$	=	Jacobian matrix of the CMG system associated with the gimbal angles
$\boldsymbol{D}$	=	Jacobian matrix of the CMG system associated with the wheel speed
$\hat{\boldsymbol{e}}$	=	eigen axis vector for the quaternion
$\boldsymbol{g}_i$	=	ith gimbal axis vector
$\boldsymbol{h}$	=	angular momentum vector for the CMG system
$\boldsymbol{H}_i$	=	angular momentum vector of the ith CMG
$\boldsymbol{I}_s$	=	unit matrix of dimension s
$\boldsymbol{J}$	=	inertia tensor for the spacecraft excluding the CMGs system
J_w	=	moment of inertia of each CMG wheel around rotation ($= 2.0 \times 10^{-4}$ kgm^2)
H_0	=	nominal angular moment of the CMG, Nms
H_i	=	angular momentum of the ith CMG, Nms
$\boldsymbol{H}_s$	=	angular momentum vector of the spacecraft including the CMG system

k	=	gain for the null motion
$\boldsymbol{K}_p, \boldsymbol{K}_d$	=	control gain matrices for quaternion feedback control
$\boldsymbol{Q}$	=	Jacobian matrix for the VSCMG system (= $[\boldsymbol{C}, \boldsymbol{D}]$)
$\boldsymbol{q}$	=	quaternion
$\boldsymbol{q}_e$	=	quaternion error from the current attitude to the goal attitude
$\hat{\boldsymbol{q}}$	=	first three elements of the quaternion
$\boldsymbol{R}$	=	direction cosine matrix of the spacecraft attitude
S	=	sensitivity function
T	=	complementarity sensitivity function
$\boldsymbol{T}_{\text{ext}}$	=	external torque vector
$\boldsymbol{u}$	=	command torque (Nms)
$\boldsymbol{W}_i$	=	symmetric weighting matrices, $(i = 1, 2, 3)$
W_s, W_t	=	weighting functions for the mixed sensitivity problem
β	=	pyramid skew angle (= 54.73 deg)
$\boldsymbol{\delta}$	=	gimbal angle vector (= $(\delta_1, \delta_2, \delta_3, \delta_4)^T$)
δ_i	=	gimbal angle of the ith CMG
κ_1, κ_2	=	condition numbers associated with Jacobian matrices $\boldsymbol{C}$ and $\boldsymbol{D}$, respectively
$\boldsymbol{\Phi}$	=	eigenvector for the generalized eigenvalue problem
$\boldsymbol{\omega}$	=	spacecraft angular velocity (= $(\omega_1, \omega_2, \omega_3)^T$)
Ω_i	=	rotational speed of ith CMG (rad/s)
$\boldsymbol{\Omega}$	=	CMG wheel rotational speed vector (= $(\Omega_1, \Omega_2, \Omega_3, \Omega_4)^T$), rad/s

4.1 Introduction

Spacecraft attitude control is necessary to smoothly accomplish many missions. Since the first manned space vehicle was launched, the size of spacecraft has increased. As spacecraft have become larger, solar panels installed on them have also become larger so that they may supply sufficient electric power to the spacecraft. Increasing the size

of solar panels lowers their natural vibration frequency. Because of these low natural frequencies, solar panels are likely to experience vibrations during attitude maneuvers. Such vibrations are undesirable when undertaking missions because the spacecraft attitude may become unstable if vibrations are not taken into consideration. To suppress the vibrations of these flexible structures, H_∞ methods are considered.

H_∞ methods are used in modern control theory to design controllers that can suppress vibrations and stabilize the spacecraft with guaranteed control performance [1–3]. To obtain the desired controller, H_∞ methods access the transfer function by using the H_∞ norm, which gives the maximum output of the transfer function with respect to the input. If the H_∞ norm is small, the designed controller will successfully suppress the vibrations and stabilize the spacecraft with guaranteed control performance. In particular, the linear matrix inequality (LMI)-based H_∞ controller design method is suitable for obtaining the desired controller by solving a convex optimization even if the control system and the requirement are complicated.

Spacecraft need actuators, such as thrusters, to realize calculated command control torques, as well as momentum-exchange torque generators, specifically reaction wheels (RWs) and control moment gyros (CMGs). As mentioned earlier, spacecraft tend to increase in size as missions become increasingly complicated. Large spacecraft require a large output torque for attitude maneuvering because of their large moment of inertia. Thus, momentum-exchange torque generators are necessary for large spacecraft to generate a high output torque. CMG systems are more suitable than RWs for this purpose.

CMG systems can be classified into two types based on the degrees of freedom of each CMG: single-gimbal CMGs (SGCMGs) and double-gimbal CMGs (DGCMGs). SGCMGs can generate a higher torque than DGCMGs. SGCMG systems are mechanically simpler than DGCMG systems, but producing a torque around an arbitrary direction generally requires more than three SGCMGs for three-axis attitude control. Even when four SGCMGs are used, SGCMG systems have more critical singularity problems than DGCMGs. SGCMG systems suffer from a singularity problem when the number

of CMG units is less than six. Numerous studies have been conducted in an attempt to overcome the singularity problem for SGCMGs [4–14] and single-gimbal variable-speed CMGs (VSCMGs) [15–20], which have more functions than a typical SGCMG.

VSCMG systems have functions of both CMGs and RWs. The control torques generated by CMGs are much larger than those generated by RWs. It is preferable to use the maximum angular momentum of the CMGs to rapidly maneuver the spacecraft attitude. Conversely, RWs are more effective at maintaining the spacecraft at the desired attitude in the presence of an external disturbance because the control torques generated by RWs are more precise than those generated by CMGs. Considering the advantages of CMGs and RWs, VSCMG systems can use the CMG mode for fast attitude maneuvering and the RW mode for precise attitude stabilization in the target direction.

From the above key points regarding H_∞ methods and VSCMG systems, the sole use of the LMI-based H_∞ controller is insufficient to calculate the command control torque that can suppress the vibration of flexible structures and stabilize the spacecraft with guaranteed control performance when dealing with a large spacecraft. For such a spacecraft, VSCMGs should be used in addition to the H_∞ controller to realize the large command control torque required to control the spacecraft attitude by using the CMG mode and the small torque required to stabilize the spacecraft and suppress the vibration of the flexible structures near the end of the maneuver by using the RW mode. Past studies [21, 22] have considered LMI-based controller designs for DGCMG systems or DGVSCMG systems. In these papers, a model of the spacecraft was used to construct a linear parameter-varying (LPV) model while considering DGCMG or DGVSCMG systems. Then, LPV state feedback control was designed by solving a convex optimization problem using LMI. The algorithm proposed in these studies was shown to be successful in the design of gain-scheduled LPV state-feedback controllers, and the effectiveness of these controllers for DGCMG and DGVSCMG was demonstrated. However, these studies did not consider a spacecraft equipped with flexible structures. Conversely, other past studies [23, 24] have analyzed LMI-based controllers for DGCMG systems by considering the suppression of the vibration. In these papers, DGCMG systems were assessed for

their ability to suppress vibrations in medium-sized or small structures. These studies showed the effectiveness of the design method based on H_∞ control using LMI. However, these studies did not consider fast attitude maneuvering.

In contrast to these past studies, it is important to consider both fast, stable attitude maneuvering and the vibration suppression of flexible structures because in the near future, spacecraft will continue to grow in size to be able to simultaneously accomplish numerous missions. Therefore, this study investigates the use of a pyramid-type variable-speed four-SGCMG system that is suitable for the fast attitude maneuvering of the spacecraft. Additionally, an LMI-based controller is designed to generate the command control torque for a spacecraft equipped with flexible structures. In this study, we consider a controller to generate the command control torque and a steering controller.

The proposed controller is designed by H_∞ synthesis via LMI taking into consideration the characteristics of the wheel dynamics of the experimental VSCMG setup developed in our laboratory, which is expressed as a second-order system with different characteristics for the acceleration and deceleration cases. In particular, the RW mode will be activated to realize the command torque generated by the abovementioned controller for precise attitude stabilization and vibration suppression at the end of a maneuver. Furthermore, to realize the command control torque generated by the abovementioned controller, it is desirable to use the CMG mode for fast attitude maneuvering when the attitude error is large and to use the RW mode for vibration suppression and precise attitude stabilization in the target direction when the attitude error is small. To achieve a smooth mode transition in the VSCMG, the CMG and RW modes can be selected by employing the gain-scheduled steering control law that is adopted for the VSCMG in this study. The proposed gain-scheduled steering law consists of the generalized singularity-robust (GSR) term and the local gradient-based null motion (LG) term for the VSCMGs. These two terms are weighted using weighting matrices. The elements in the weighting matrices related to the CMG and RW modes are changed according to the attitude errors and condition numbers for the two modes. The gradient-based null motion is employed to set the gimbal angle to a suitable value for the RW mode

to effectively stabilize the spacecraft attitude at the end of a maneuver. This proposed steering control law contributes to the effective utilization of the VSCMG system, which has characteristics of both CMG and RW systems.

Numerical simulations are carried out, and their results demonstrate the effectiveness of the proposed steering control law for attitude stabilization, vibration suppression, and transitioning between the CMG and RW modes. However, the LMI-based H_∞ controller cannot be simply applied to the VSCMG system, because the VSCMG system is a nonlinear system whereas the designed H_∞ controller is linear. If we apply the linear H_∞ controller to a nonlinear system, the effectiveness of the controller is guaranteed only near the end of a maneuver [25–29]. Thus, the proposed H_∞ control law will be applied for a short time at the beginning and near the end of a maneuver in the numerical simulation.

4.2 Variable-Speed Control Moment Gyros

The pyramid-array variable-speed four-SGCMG system proposed in this study is shown in Fig. 4.1. The skew angle β for the pyramid array CMG is usually set to $\beta = 54.73$ deg, because the momentum envelope, which represents the maximum available angular moment of the CMG for an attitude maneuver, becomes nearly spherical. The wheel speed of the flywheel is treated as a variable in VSCMG systems. From this point of view, VSCMG systems can be considered hybrid systems with characteristics of both SGCMG and RW systems. A conceptual transition diagram for the steering control law for our VSCMG system is shown in Fig. 4.2. The CMG mode can generate a much larger control torque than the RW mode. The spacecraft achieves fast rotational motion by using the CMG mode when the attitude error is large. The VSCMG mode takes a middle position between the CMG and RW modes and should be activated when the attitude error is small. The RW mode can more precisely generate the control torque than the CMG mode. Thus, the RW mode should be activated for the precise attitude stabilization at the end of a maneuver. Mode transitions between the CMG and RW

modes were considered for the scissor CMG system ([30]). In this study, a similar mode transition method is considered for the pyramid-type variable-speed four-SGCMG system.

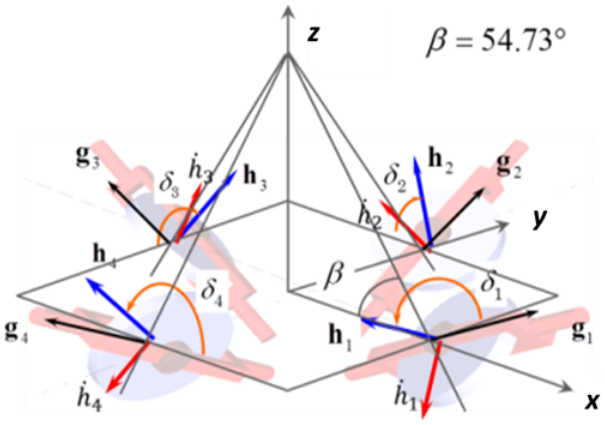

Figure 4.1: Pyramid-type variable-speed four-SGCMG system.

4.2.1 Jacobian matrix of VSCMG

The total angular momentum of the pyramid-array VSCMG is given by

$$\begin{aligned} \boldsymbol{h} &= H_1 \begin{bmatrix} -\cos\beta\sin\delta_1 \\ \cos\delta_1 \\ \sin\beta\sin\delta_1 \end{bmatrix} + H_2 \begin{bmatrix} -\cos\delta_2 \\ -\cos\beta\sin\delta_2 \\ \sin\beta\sin\delta_2 \end{bmatrix} \\ &+ H_3 \begin{bmatrix} \cos\beta\sin\delta_3 \\ -\cos\delta_3 \\ \sin\beta\sin\delta_3 \end{bmatrix} + H_4 \begin{bmatrix} \cos\delta_4 \\ \cos\beta\sin\delta_4 \\ \sin\beta\sin\delta_4 \end{bmatrix} \end{aligned} \tag{4.1}$$

where H_i is the angular momentum of the ith CMG unit around the wheel spin axis and is given by $J_\omega\Omega_i$. Considering that the wheel speed Ω_i in the VSCMGs is variable and assuming that the moment of inertia of the CMG wheel unit about all axes other than the spin axis can be neglected, the time derivative of the angular momentum of the

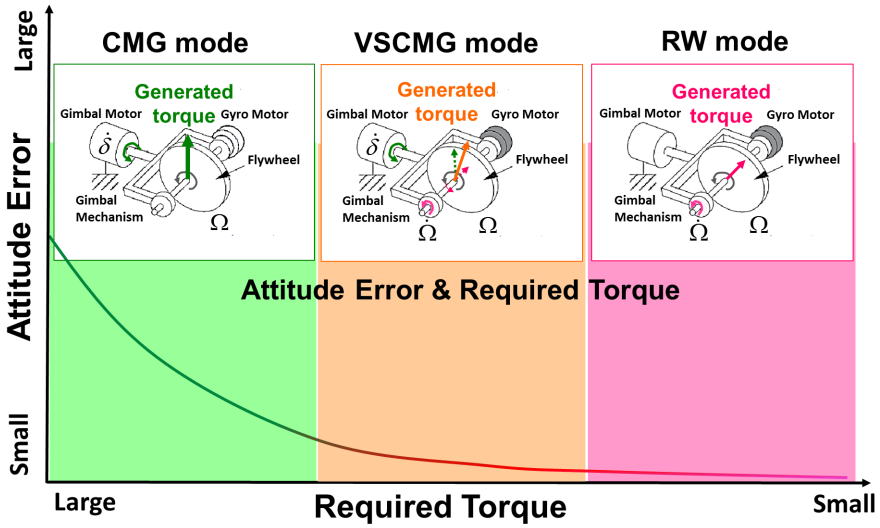

Figure 4.2: Conceptual transition diagram for VSCMG.

VSCMG is obtained as

$$\dot{\boldsymbol{h}} = \sum_{i=1}^{4} \frac{\partial \boldsymbol{H}_i}{\partial \delta_i} \dot{\delta}_i + \sum_{i=1}^{4} \frac{\partial \boldsymbol{H}_i}{\partial \Omega_i} \dot{\Omega}_i = \begin{bmatrix} \boldsymbol{C} & \boldsymbol{D} \end{bmatrix} \begin{bmatrix} \dot{\boldsymbol{\delta}} \\ \dot{\boldsymbol{\Omega}} \end{bmatrix} \tag{4.2}$$

where $[\ \boldsymbol{C} \quad \boldsymbol{D}\ ](=\boldsymbol{Q})$ is the Jacobian matrix with respect to the gimbal angles and wheel speed, and is given as

$$\boldsymbol{C} = \begin{bmatrix} -H_1 \cos\beta \cos\delta_1 & H_2 \sin\delta_2 & H_3 \cos\beta \cos\delta_3 & -H_4 \sin\delta_4 \\ -H_1 \sin\delta_1 & -H_2 \cos\beta \cos\delta_2 & H_3 \sin\delta_3 & H_4 \cos\beta \cos\delta_4 \\ H_1 \sin\beta \cos\delta_1 & H_2 \sin\beta \cos\delta_2 & H_3 \sin\beta \cos\delta_3 & H_4 \sin\beta \cos\delta_4 \end{bmatrix}, \tag{4.3}$$

$$\boldsymbol{D} = J_w \begin{bmatrix} \cos\beta \sin\delta_1 & -\cos\delta_2 & \cos\beta \cos\delta_3 & \cos\delta_4 \\ \cos\delta_1 & -\cos\beta \sin\delta_2 & -\cos\delta_3 & \cos\beta \sin\delta_4 \\ \sin\beta \cos\delta_1 & \sin\beta \cos\delta_2 & \sin\beta \cos\delta_3 & \sin\beta \sin\delta_4 \end{bmatrix}. \tag{4.4}$$

These two matrices are related to the CMG and RW modes, respectively.

4.2.2 Condition number analysis of Jacobian matrices

In this study, the condition numbers for the matrices $\boldsymbol{C}$ and $\boldsymbol{D}$ are analyzed with respect to the gimbal angle. CMGs can generate a larger torque than RWs, but CMGs are inferior to RWs regarding the generation of a sufficiently precise small torque because of the limited resolution of the gimbal angle control. In contrast, RWs do not have such limited resolution for the generated torque. Therefore, the RW mode is suitable for attitude stabilization near the end of a maneuver. The objective of the condition number analysis is to determine suitable gimbal angles for the activation of the RW mode at the end of the maneuver. Assuming that the total angular momentum of a spacecraft equipped with a CMG system is zero, the angular momentum of the CMG system becomes zero at the end of the attitude maneuver. A set of gimbal angles that yield a zero angular momentum of the CMGs can be obtained by employing the null motion from gimbal angles of zero, i.e., $\boldsymbol{\delta} = (\delta, -\delta, \delta, -\delta)^T$. This set of gimbal angles implies that the signs of the gimbal angles of CMGs facing each other are the same and those of neighboring CMGs are opposite. Figure 4.3 shows the condition numbers for the Jacobian matrices $\boldsymbol{C}$ and $\boldsymbol{D}$ with respect to the gimbal angle δ. When the gimbal angle is 0 deg or 60 deg, the condition number κ_1 for the CMG mode is small, and the condition number κ_2 for the RW mode is large. Conversely, when the gimbal angle is 30 deg or 90 deg, the condition number κ_2 for the RW mode is small, and the condition number κ_1 for the CMG mode is large. Based on these results, the following three points can be addressed.

(1) A gimbal angle of 0 deg or 60 deg is desirable to effectively utilize the CMG mode.

(2) A gimbal angle of 30 deg or 90 deg is desirable to effectively utilize the RW mode.

(3) A gimbal angle of 15 deg or 75 deg is desirable to effectively utilize the CMG and RW modes simultaneously (i.e., the VSCMG mode) if the CMG and RW modes can generate equal attitude control torques.

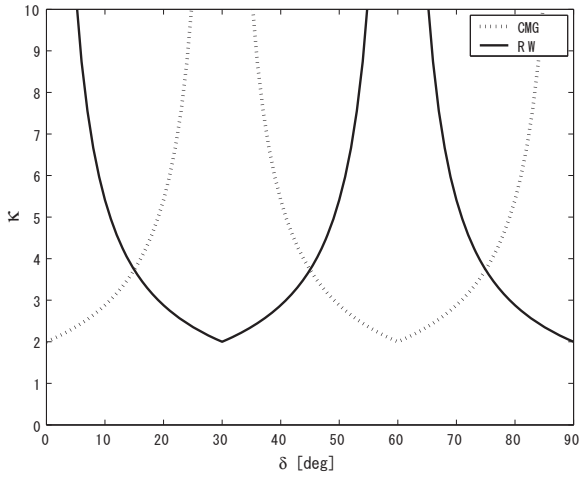

Figure 4.3: Condition number vs. gimbal angle.

In this study, a gimbal angle of 30 deg or 90 deg should be chosen near the end of the maneuver to activate the RW mode because it is intended to activate the RW mode and deactivate the CMG mode near the end of a maneuver.

4.2.3 Wheel rotational dynamics

A CMG flywheel cannot quickly respond to a rotational acceleration or deceleration command because of the mechanical and electrical limitations of the motor driving the rotational motion of the wheel and the moment of inertia of the wheel. In this subsection, the wheel dynamics are addressed to precisely simulate the rotational motion of the wheel and the attitude motion of a spacecraft controlled by the VSCMG system in our laboratory. In the experimental setup of the VSCMG system, the rotational motion of the CMG flywheel is derived using a brushless direct current (DC) electric motor and the rotational speed is measured using a hall-effect sensor. To precisely obtain the characteristics of the wheel dynamics, we measured the time response of the wheel rotational speed to the command wheel speed, which is given in a step form. The moment of inertia of the control moment gyro wheel around the spin axis is 2.07×10^{-4} kgm^2. An acceleration case (from 1500 to 3000 rpm) and a deceleration case (from 3000 to 1500

Table 4.1: Wheel dynamics parameters.

	Acceleration case	Deceleration case
P	0.127	0.317
t_p	45.7 s	64.9 s
ζ	0.549	0.343
ω_n	0.0822 rad/s	0.0515 rad/s

rpm) are studied. Figures 4.4(a) and 4.4(b) show the step responses of the wheel speed for the acceleration and deceleration cases, respectively. The responses of the wheel speed are similar to the step response of a second-order system with a damping ratio of nearly 0.5, as shown in the figures. The characteristic equation of such a second-order system can be expressed as

$$s^2 + 2\zeta\omega_n s + \omega_n^2 = 0 \tag{4.5}$$

where ζ is the damping ratio and ω_n is the natural angular frequency. These two parameters can be estimated from the overshoot P and overshoot timing t_p as follows:

$$\zeta = \frac{|\log P|}{\sqrt{\pi^2 + |\log P|^2}} , \tag{4.6}$$

$$\omega_n = \frac{\pi}{t_p\sqrt{1-\zeta^2}} . \tag{4.7}$$

The overshoot P and overshoot timing t_p are measured from the experimental results.

Table 4.1 shows the overshoot and overshoot timing measured from the experimental results and the estimated parameters ζ and ω_n for the wheel rotational speed dynamics. These estimated parameters are used for the numerical simulations.

4.3 Modeling of Flexible Spacecraft

The equations of motion for the spacecraft describe the translational, rotational, and vibrational motion of the flexible structure. It is assumed that the spacecraft is equipped with flexible structures and a CMG system, which maneuvers the attitude. First, the

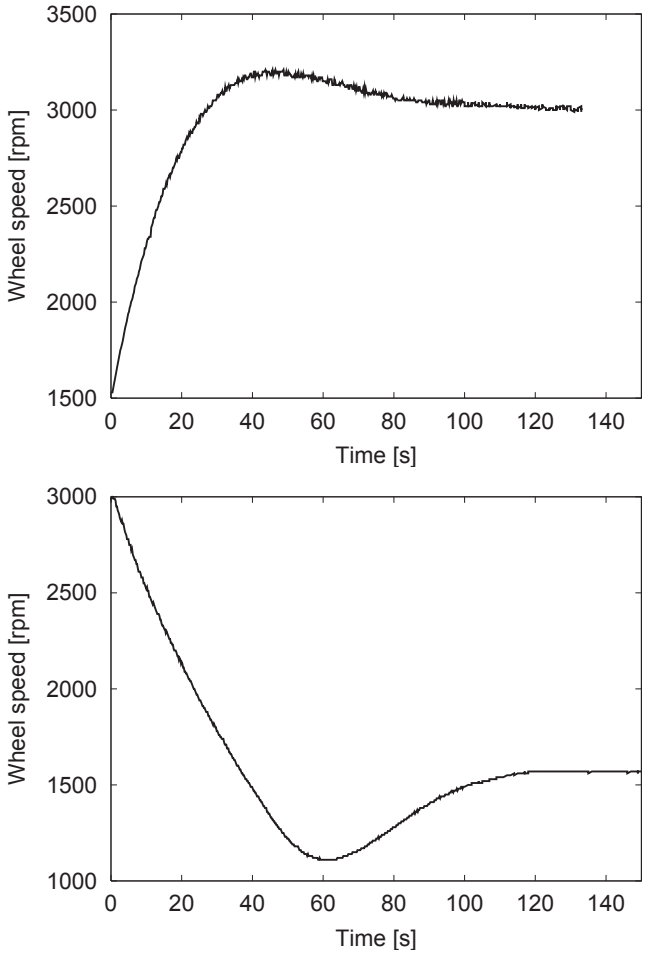

Figure 4.4: Time response of wheel speed for (a) acceleration and (b) deceleration.

equations of motion for a rigid spacecraft using a CMG system for the maneuvering of the attitude are introduced. Subsequently, the equations of motion for a spacecraft equipped with a flexible structure are derived. In this section, a spacecraft is assumed to be equipped with two flexible solar panels, as shown in Fig. 4.5. The in-plane, out-of-plane, and torsional vibrations of the flexible structure affect the spacecraft. If the spacecraft rotates around the x-axis, the out-of-plane vibration of the flexible structure affects the spacecraft motion around the x-axis. The in-plane and torsional vibration of the flexible structure affects the spacecraft motion around the z- and y-axes, respectively.

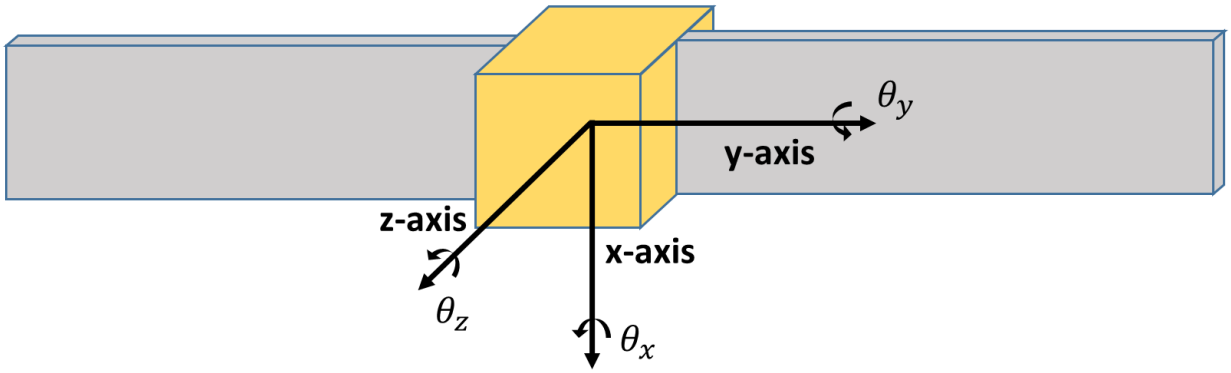

Figure 4.5: Spacecraft equipped with flexible structures.

4.4 Equations of Motion

4.4.1 Equations of motion for CMG systems

The total angular momentum vector, which consists of the angular momentum of the main body of the spacecraft and the CMG angular momentum, is expressed as

$$\boldsymbol{H}_s = \boldsymbol{J}\boldsymbol{\omega} + \boldsymbol{h} \ . \tag{4.8}$$

The rotational equation of motion for a rigid spacecraft using momentum-exchange actuators, such as CMG systems, is given by

$$\dot{\boldsymbol{H}}_s + \boldsymbol{\omega} \times \boldsymbol{H}_s = \boldsymbol{T}_{\text{ext}} \ . \tag{4.9}$$

Equations (4.8) and (4.9) are combined to yield

$$\boldsymbol{J}\dot{\boldsymbol{\omega}} + \dot{\boldsymbol{h}} + \boldsymbol{\omega} \times (\boldsymbol{J}\boldsymbol{\omega} + \boldsymbol{h}) = \boldsymbol{T}_{\text{ext}} \ . \tag{4.10}$$

Introducing the internal control torque vector generated by the CMGs (denoted by $\boldsymbol{u} = (u_1, u_2, u_3)^T$), Eq. (4.10) is rewritten as

$$\boldsymbol{J}\dot{\boldsymbol{\omega}} + \boldsymbol{\omega} \times \boldsymbol{J}\boldsymbol{\omega} = \boldsymbol{u} + \boldsymbol{T}_{\text{ext}} \ , \tag{4.11}$$

$$\boldsymbol{u} = -\dot{\boldsymbol{h}} - \boldsymbol{\omega} \times \boldsymbol{h} \ . \tag{4.12}$$

4.4.2 Constrained mode model

The equations of vibrational motion of the flexible structure are considered. The vibrational motion can be expressed as

$$\boldsymbol{M}\ddot{\boldsymbol{\xi}} + \boldsymbol{E}\dot{\boldsymbol{\xi}} + \boldsymbol{K}\boldsymbol{\xi} = \boldsymbol{0} \tag{4.13}$$

where $\boldsymbol{M}$, $\boldsymbol{E}$, and $\boldsymbol{K}$ are the mass, damping, and stiffness matrices, respectively, and $\boldsymbol{\xi} \in \mathcal{R}^n$ is the displacement vector at the nodes of the finite element. The above equations need to be expressed in a modal coordinate system to design the controller. To obtain a modal coordinate system, a generalized eigenvalue problem is solved. The obtained modal coordinate system can be expressed as

$$\bar{\boldsymbol{M}}\ddot{\boldsymbol{\eta}} + \bar{\boldsymbol{E}}\dot{\boldsymbol{\eta}} + \bar{\boldsymbol{K}}\boldsymbol{\eta} = \boldsymbol{0} \tag{4.14}$$

where $\bar{\boldsymbol{M}}$, $\bar{\boldsymbol{E}}$, and $\bar{\boldsymbol{K}}$ are diagonal matrices. These diagonal matrices have modal parameters that consist of the modal mass, frequency, and damping ratio, respectively. By combining this normalized, diagonalized equation for the flexible structure with the translational and rotational motion, the constrained mode model can be obtained as

$$\boldsymbol{m}\ddot{\boldsymbol{x}} + \boldsymbol{\rho}_0\ddot{\boldsymbol{\eta}} = \boldsymbol{F}_t \ , \tag{4.15}$$

$$\boldsymbol{J}\ddot{\boldsymbol{\theta}} + \boldsymbol{\rho}_1\ddot{\boldsymbol{\eta}} = \boldsymbol{F}_r \ , \tag{4.16}$$

$$\boldsymbol{\rho}_0^T\ddot{\boldsymbol{x}} + \boldsymbol{\rho}_1\dot{\boldsymbol{\theta}} + \ddot{\boldsymbol{\eta}} + \bar{\boldsymbol{E}}\dot{\boldsymbol{\eta}} + \bar{\boldsymbol{K}}\boldsymbol{\eta} = \boldsymbol{0} \tag{4.17}$$

where $\boldsymbol{x} \in \mathcal{R}^3$, $\boldsymbol{\theta} \in \mathcal{R}^3$, and $\boldsymbol{\eta} \in \mathcal{R}^n$ are the displacement, rotational angle, and modal coordinate, respectively. In addition, $\boldsymbol{m} \in \mathcal{R}^{3\times3}$, $\boldsymbol{J} \in \mathcal{R}^{3\times3}$, $\boldsymbol{\rho}_0 \in \mathcal{R}^{3\times n}$, $\boldsymbol{\rho}_1 \in \mathcal{R}^{3\times n}$, $\bar{\boldsymbol{E}} \in \mathcal{R}^{n\times n}$, $\bar{\boldsymbol{K}} \in \mathcal{R}^{n\times n}$, $\boldsymbol{F}_t$ and $\boldsymbol{F}_r$ are the mass matrix, moment of inertia tensor, zeroth and first interference matrices, damping matrix, rigidity matrix, translational force and rotational torque, respectively.

However, the translational motion should be removed from the constrained mode model when designing the attitude controller because translational motion is generally uncontrollable and unobservable from the viewpoint of attitude control. In addition, the rotational motion becomes the motion of the low-dimensional parameterizations. In this study, five vibration modes are considered as the constrained modal parameters, that is, $n = 5$. The modal frequency and damping ratio of the constrained modal parameters are listed in Table 4.2. These parameters are chosen by referring to [31]. The constrained mode model for the controller design can be derived from

$$\hat{\boldsymbol{M}}\ddot{\boldsymbol{p}} + \hat{\boldsymbol{E}}\dot{\boldsymbol{p}} + \hat{\boldsymbol{K}}\boldsymbol{p} = \hat{\boldsymbol{L}}\boldsymbol{F}_r \,, \tag{4.18}$$

$$\boldsymbol{y} = \hat{\boldsymbol{H}}\boldsymbol{p} \tag{4.19}$$

where $\boldsymbol{p} = [\boldsymbol{\theta}^T \ \boldsymbol{\eta}^T]^T$ and

$$\begin{aligned}
\hat{\boldsymbol{M}} &= \begin{bmatrix} \boldsymbol{J} & \boldsymbol{\rho}_1 \\ \boldsymbol{\rho}_1^T & \boldsymbol{I}_5 \end{bmatrix} \in \mathcal{R}^{8\times8} \,, \\
\hat{\boldsymbol{K}} &= \begin{bmatrix} \boldsymbol{0} & \boldsymbol{0} \\ \boldsymbol{0} & \bar{\boldsymbol{K}} \end{bmatrix} \in \mathcal{R}^{8\times8} \,, \\
\hat{\boldsymbol{E}} &= \begin{bmatrix} \boldsymbol{0} & \boldsymbol{0} \\ \boldsymbol{0} & \bar{\boldsymbol{E}} \end{bmatrix} \in \mathcal{R}^{8\times8} \,, \\
\hat{\boldsymbol{L}} &= \begin{bmatrix} \boldsymbol{I}_3 \\ \boldsymbol{0}_{5\times3} \end{bmatrix} \in \mathcal{R}^{8\times3} \,, \\
\hat{\boldsymbol{H}} &= \hat{\boldsymbol{L}}^T \in \mathcal{R}^{3\times8} \,.
\end{aligned}$$

Table 4.2: Constrained modal parameters.

Mode No. (i)	Modal frequency (Hz)	Damping ratio
1	1.00	0.05
2	3.94	0.05
3	11.83	0.05
4	12.52	0.05
5	17.37	0.05

4.4.3 Non-constrained mode model

The obtained constrained mode model is converted into a non-constrained mode model, which is expressed by Eqs. (4.20) and (4.21). By solving the generalized eigenvalue problem $\hat{\boldsymbol{K}}\boldsymbol{\Phi} = \sigma\hat{\boldsymbol{M}}\boldsymbol{\Phi}$, the non-constrained mode model can be derived as

$$\ddot{\boldsymbol{\mu}} + \Delta\dot{\boldsymbol{\mu}} + \boldsymbol{\Lambda}\boldsymbol{\mu} = \boldsymbol{\Phi}^T\hat{\boldsymbol{L}}\boldsymbol{F}_r \ , \tag{4.20}$$

$$\boldsymbol{y} = \hat{\boldsymbol{L}}^T\boldsymbol{\Phi}\boldsymbol{\mu} \tag{4.21}$$

where the eigenvector of the generalized eigenvalue problem for conversion, $\boldsymbol{\Phi}$, can be expressed as

$$\boldsymbol{\Phi} = \begin{bmatrix} \boldsymbol{J}^{-\frac{1}{2}} & \boldsymbol{\Psi} \\ \boldsymbol{0}_{5\times 3} & \boldsymbol{\Theta} \end{bmatrix} \tag{4.22}$$

where $\boldsymbol{\Theta} \in \mathcal{R}^{5\times 5}$ is a diagonal matrix, and $\boldsymbol{\Psi} = [\psi_1, \psi_2, \cdots, \psi_5]$. Therefore, Eq. (4.20) is converted as follows:

$$\ddot{\boldsymbol{\eta}}_r = \boldsymbol{J}^{-\frac{1}{2}} \ , \tag{4.23}$$

$$\ddot{\boldsymbol{\eta}}_f + 2\nu\sigma\boldsymbol{\eta}_f + \sigma^2\boldsymbol{\eta}_f = \boldsymbol{\Psi}^T\boldsymbol{F}_r \tag{4.24}$$

where $\boldsymbol{\eta}_r$ is the rigid body mode, $\boldsymbol{\eta}_f$ is the flexible mode, and σ is the non-constrained mode frequency. In addition, $\boldsymbol{\mu} = [\boldsymbol{\eta}_r^T \ \boldsymbol{\eta}_f^T]^T$ can be translated to $\boldsymbol{p} = [\boldsymbol{\theta}^T \ \boldsymbol{\eta}^T]^T$ by using $\boldsymbol{\Phi}$, as

$$\boldsymbol{p} = \boldsymbol{\Phi}\boldsymbol{\mu} \ . \tag{4.25}$$

Table 4.3: Modal parameters.

Mode No. (i)	σ_i (Hz)	ψ_i	ν_i
0	0.00	$\boldsymbol{J}^{-\frac{1}{2}}$	0.00
1	1.04	-0.273	0.05
2	3.96	-0.073	0.05
3	11.92	0.158	0.05
4	12.57	-0.074	0.05
5	17.45	-0.091	0.05

Equation (4.24) is converted as

$$\dot{\boldsymbol{\theta}} = \boldsymbol{J}^{-1}\boldsymbol{F}_r + \boldsymbol{\Psi}\boldsymbol{\eta}_f \ . \tag{4.26}$$

Equation (4.26) is similar to Eq. (4.11). By adding the second term on the left-hand side of Eq. (4.11) ($= -\boldsymbol{J}^{-1}(\boldsymbol{\omega} \times \boldsymbol{J}\boldsymbol{\omega})$), Eq. (4.26) can be made equivalent to Eq. (4.11). The natural frequency of this model is stored because the vibration of the non-constrained mode model can be expressed as an additive error. However, in the constrained mode model, the natural frequency changes if the higher vibration is cut off. Thus, the constrained mode model is not suitable for the design of the controller. For this reason, the non-constrained mode model is used to design the controller in this study. The modal parameters of the non-constrained mode model are listed in Table 4.3. These parameters are chosen by referring to [31]. In this study, the rigid body mode (No. 0) and the first flexible mode (No. 1) of the out-of-plane vibrational motion are treated as a control model for the design of the controller. Other modes are treated as a residual model.

4.5 Quaternion

In this study, a quaternion is used to express the attitude of the spacecraft. A quaternion vector $\boldsymbol{q}(=(q_1,q_2,q_3,q_4)^T=(\hat{\boldsymbol{q}}^T,q_4)^T)$ is defined as

$$\boldsymbol{q}=\begin{bmatrix}\hat{\boldsymbol{q}}\\ q_4\end{bmatrix}=\begin{bmatrix}\hat{\boldsymbol{e}}\sin(\varphi/2)\\ \cos(\varphi/2)\end{bmatrix} \tag{4.27}$$

where $\hat{\boldsymbol{e}}$ is the eigen axis unit vector for rotation, and φ is the rotational angle. The direct cosine matrix from the inertial frame to the body frame $\boldsymbol{R}$ is given using quaternions as

$$\boldsymbol{R}=\begin{bmatrix}1-2(q_2^2+q_3^2) & 2(q_1q_2+q_3q_4) & 2(q_1q_3-q_2q_4)\\ 2(q_1q_2-q_3q_4) & 1-2(q_1^2+q_3^2) & 2(q_2q_3+q_1q_4)\\ 2(q_1q_3+q_2q_4) & 2(q_2q_3-q_1q_4) & 1-2(q_1^2+q_2^2)\end{bmatrix}. \tag{4.28}$$

The differential equations describing quaternion kinematics are given by

$$\begin{bmatrix}\dot{q}_1\\ \dot{q}_2\\ \dot{q}_3\\ \dot{q}_4\end{bmatrix}=\frac{1}{2}\begin{bmatrix}0 & \omega_3 & -\omega_2 & \omega_1\\ -\omega_3 & 0 & \omega_1 & \omega_2\\ \omega_2 & -\omega_1 & 0 & \omega_3\\ -\omega_1 & -\omega_2 & -\omega_3 & 0\end{bmatrix}\begin{bmatrix}q_1\\ q_2\\ q_3\\ q_4\end{bmatrix} \tag{4.29}$$

or

$$\dot{\boldsymbol{q}}=\frac{1}{2}\begin{bmatrix}q_4\boldsymbol{\omega}-\boldsymbol{\omega}\times\hat{\boldsymbol{q}}\\ -\boldsymbol{\omega}^T\hat{\boldsymbol{q}}\end{bmatrix}. \tag{4.30}$$

A quaternion vector is well suited for on-board real-time computation. In addition, a quaternion vector has no singular points. The attitude error quaternions are computed using the desired or commanded attitude quaternions and the current attitude quaternions as

$$\begin{bmatrix}q_{e1}\\ q_{e2}\\ q_{e3}\\ q_{e4}\end{bmatrix}=\begin{bmatrix}q_{c4} & q_{c3} & -q_{c2} & -q_{c1}\\ -q_{c3} & q_{c4} & q_{c1} & -q_{c2}\\ q_{c2} & -q_{c1} & q_{c4} & -q_{c3}\\ q_{c1} & q_{c2} & q_{c3} & q_{c4}\end{bmatrix}\begin{bmatrix}q_1\\ q_2\\ q_3\\ q_4\end{bmatrix} \tag{4.31}$$

where q_{ei} is the i th attitude quaternion and q_c is the i the desired or commanded attitude quaternion. If the fastest attitude control laws are required, the quaternion feedback

control law can be a candidate. The following quaternion feedback control ([32]) can be considered for real-time implementation to determine the commanded torque:

$$\boldsymbol{u} = -\boldsymbol{K}_p \hat{\boldsymbol{q}}_e - \boldsymbol{K}_d \boldsymbol{\omega} \ . \tag{4.32}$$

Hereafter, for simplicity, it is assumed that the desired attitude is the inertial frame. In this case, the attitude error quaternion is idential to the current attitude quaternion, that is $\boldsymbol{q}_e = \boldsymbol{q}$.

4.6 H_∞ Methods

As previously mentioned, because spacecraft have been increasing in size each year, solar panels installed on large spacecraft have increased in size as well and thus have a lower natural vibration frequency. Because of the decreased natural frequency, vibrations may be excited on the solar panels. The modeling of flexible spacecraft is necessary in order to design an effective controller to stabilize the spacecraft and suppress the vibration of flexible structures. The governing equations for the vibrational motion should be mathematically expressed by ideal equations.

Because the dimension of the controller is finite, the controller is designed using the equations of motion in the form of low-dimensional parameterizations. H_∞ methods are used in modern control theory to design controllers that can achieve stabilization with guaranteed control performance. To obtain the desired controller, H_∞ methods access the transfer function by using the H_∞ norm. This H_∞ norm yields the maximum output of the transfer function with respect to the input. If the H_∞ norm is small, the designed controller will achieve stabilization with guaranteed control performance. Because H_∞ methods are highly robust, they can overcome the VSCMG system problems associated with the modeling error for the flexible structures and the characteristics of the RW. This control theory will show high robustness and precise convergence performance.

In this section, an H_∞ controller is designed, which guarantees precise convergence performance against spates of residual vibrations excited on a flexible appendage installed

in the spacecraft equipped with the VSCMG system, which has flywheel dynamics and RW and CMG systems. In addition, the H_∞ controller will be applied for a short time or near the end of a maneuver, considering that the H_∞ controller cannot be simply applied to CMG systems, because CMG systems are nonlinear. During the period in which the H_∞ controller is not applied, the quaternion feedback controller (Eq. (4.32)) is used instead to determine the attitude control torques for the spacecraft. The effectiveness of the proposed H_∞ controller for the VSCMG system will be demonstrated numerically.

4.6.1 Mixed sensitivity problem

The generalized plant is shown in Fig. 4.6. The accuracy of the target state and the robustness against the modeling error for the controlled system are very important. However, it is difficult to simultaneously achieve these two characteristics in a wide frequency band. Taking this problem into consideration, these two characteristics are treated as a mixed sensitivity problem by introducing two weighting functions W_t and W_s to divide the frequency band into high and low frequency bands. $\boldsymbol{\varpi}$ is assumed to be the target state of the output $\boldsymbol{y}$. The purpose of the controller is achieved if the difference $\boldsymbol{z}_s$ between $\boldsymbol{y}$ and $\boldsymbol{\varpi}$ is zero, i.e., if $\boldsymbol{y}$ traces $\boldsymbol{\varpi}$. The transfer function from $\boldsymbol{\varpi}$ to $\boldsymbol{z}_s$ can be expressed as

$$\boldsymbol{z}_s = -\boldsymbol{S}(s)\boldsymbol{\varpi} , \tag{4.33}$$

$$\boldsymbol{S}(s) = (\boldsymbol{I} + \boldsymbol{P}(s)\boldsymbol{K}(s))^{-1} . \tag{4.34}$$

From Eq. (4.33), if $||\boldsymbol{S}(s)||_\infty$ is made to be as small as possible, the difference $\boldsymbol{z}_s$ between $\boldsymbol{y}$ and $\boldsymbol{\varpi}$ is small. This transfer function is called the sensitivity function. If it is intended to assess the efficiency of the convergence to the target state in this manner, it is necessary to consider the minimization of the evaluation function $||\boldsymbol{S}(s)||_\infty$. However, it is not optimal to minimize the evaluation function over the entire frequency band. This is because, for example, if the heavy robot arm traces the target state in the high frequency band, the actuator of the robot arm will be broken. To overcome this problem, the weighting function W_s should be employed. By employing the weighting

function W_s, the gain of $\boldsymbol{S}(s)$ becomes small in the low frequency band. As a result, the controller will be able to achieve convergence in the low frequency band. A numerical model of the actual controlled system is used for designing the controller and controlling the actual system. However, there is a difference between the numerical model and the actual controlled system. It is necessary to design the controller to stabilize not only the numerical model but also the actual controlled system to ensure robustness. Let the actual transfer function and the transfer function of the numerical model be represented as $\boldsymbol{P}_r(s)$ and $\boldsymbol{P}(s)$, respectively. The actual transfer function $\boldsymbol{P}_r(s)$ can be expressed as

$$\boldsymbol{P}_r(s) = \boldsymbol{P}(s) + \boldsymbol{\Delta}_a(s) \tag{4.35}$$

where $\boldsymbol{\Delta}_a(s)$ is the additional error. To apply a limit to $\boldsymbol{\Delta}_a(s)$, the weighting function W_t should be employed for stabilization in the high frequency band as

$$|\boldsymbol{\Delta}_a(s)| < |W_t| \ . \tag{4.36}$$

The transfer function $\boldsymbol{T}$ from $\boldsymbol{\varpi}$ to $\boldsymbol{z}_t$ in Fig. 4.6 can be expressed as

$$\boldsymbol{T}(s) = (\boldsymbol{I} + \boldsymbol{P}(s)\boldsymbol{K}(s))^{-1}\boldsymbol{K}(s) \ . \tag{4.37}$$

If $||W_t\boldsymbol{T}(s)||_\infty$ is made as small as possible, the robustness of the modeling error can be guaranteed.

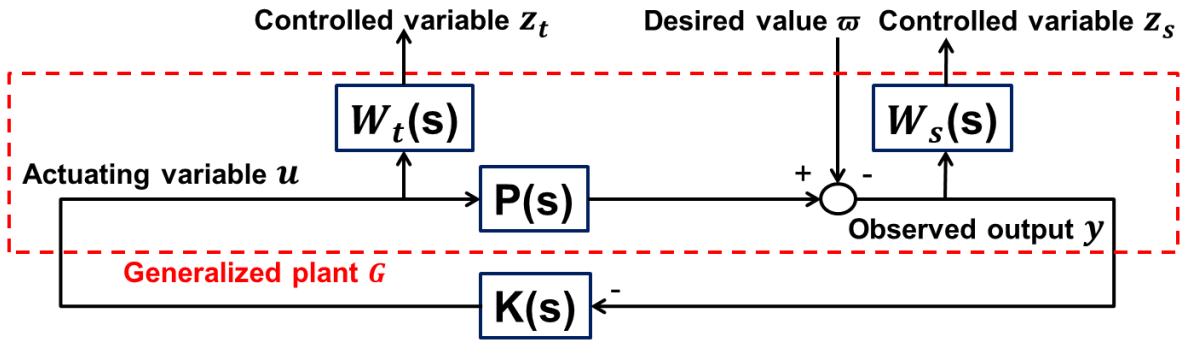

Figure 4.6: Generalized plant.

4.7 Generalized Plant Design

The damping matrix $\boldsymbol{\Delta}$, the stiffness matrix $\boldsymbol{\Lambda}$, and the input matrix $\boldsymbol{\Gamma}$ for the non-constrained mode model are divided into the control mode c and the residual mode r.

$$\boldsymbol{\Delta} = \begin{bmatrix} \boldsymbol{\Delta}_c & \mathbf{0}_{n_c \times n_r} \\ \mathbf{0}_{n_r \times n_c} & \boldsymbol{\Delta}_r \end{bmatrix} , \boldsymbol{\Lambda} = \begin{bmatrix} \boldsymbol{\Lambda}_c & \mathbf{0}_{n_c \times n_r} \\ \mathbf{0}_{n_r \times n_c} & \boldsymbol{\Lambda}_r \end{bmatrix} , \boldsymbol{\Phi}^T \boldsymbol{L} = \boldsymbol{\Gamma} = \begin{bmatrix} \boldsymbol{\Gamma}_c \\ \boldsymbol{\Gamma}_r \end{bmatrix} \tag{4.38}$$

where $\boldsymbol{\Delta}_c \in \mathcal{R}^{n_c \times n_c}$, $\boldsymbol{\Lambda}_c \in \mathcal{R}^{n_c \times n_c}$ and $\boldsymbol{\Gamma}_c \in \mathcal{R}^{n_c}$ are the matrices of the control mode c, and $\boldsymbol{\Delta}_r \in \mathcal{R}^{n_r \times n_r}$, $\boldsymbol{\Lambda}_r \in \mathcal{R}^{n_r \times n_r}$ and $\boldsymbol{\Gamma}_r \in \mathcal{R}^{n_r}$ are the matrices of the residual mode r.

The nominal plant P is provided by the control mode c.

$$\dot{\boldsymbol{x}} = \boldsymbol{A}_c \boldsymbol{x} + \boldsymbol{B}_c \boldsymbol{u} , \boldsymbol{y} = \boldsymbol{C}_c \boldsymbol{x} , \tag{4.39}$$

$$\boldsymbol{A}_c = \begin{bmatrix} \mathbf{0}_{n_c \times n_c} & \boldsymbol{I}_{n_c} \\ -\boldsymbol{\Lambda}_c & -\boldsymbol{\Delta}_c \end{bmatrix} , \boldsymbol{B}_c = \begin{bmatrix} \mathbf{0}_{n_c \times 1} \\ \boldsymbol{\Gamma}_c \end{bmatrix} , \boldsymbol{C}_c = [\boldsymbol{\Gamma}_c^T \ \ \mathbf{0}_{1 \times n_c}] . \tag{4.40}$$

An additional error $\boldsymbol{\Delta}_a(s)$ is provided by the residual mode r. The weighting function W_t is designed to limit this additional error. In addition, the wheel dynamics can be considered as a characteristic of the VSCMG system. The error for the wheel dynamics is regarded as the additional error. To stabilize the control system in a high bandwidth, the weighting function W_t is designed to be larger than the singular value of the additional error for the residual mode r and the wheel dynamics. In this section, two weighting functions W_{t1} and W_{t2} are used for different purposes in accordance with their use. First, the weighting function W_{t1} is considered when the RW mode is activated and the attitude error is small. The weighting function W_{t1} should be designed to guarantee the robustness of the residual mode r and the difference between the wheel dynamics in the acceleration and deceleration cases. The selected weighting function W_{t1} is defined as

$$W_{t1}(s) = \frac{0.001s + 2000}{6000s + 1000} . \tag{4.41}$$

The frequency responses of the chosen weighting function W_{t1}, the residual mode r, and the wheel dynamics in the acceleration and deceleration cases are shown in Fig.

4.7. The residual mode r has a maximum singular value at four frequency bands (3.96, 11.92, 12.57, and 17.45 Hz). The wheel dynamics have a maximum singular value at two frequency bands (0.007 Hz and 0.009 Hz). To guarantee the robustness of the controller in the low-dimensional parameterization, the weighting function W_{t1} (Eq. (4.41)) is designed such that the singular value of W_{t1} is larger than the singular value of the residual mode r and the additional error for the wheel dynamics in all frequency bands. Next, a case is considered in which the RW mode is not activated and the attitude error is large. In other words, the weighting function W_{t2} can be designed without considering the robustness of the controller against the difference between the wheel dynamics in the acceleration and deceleration cases when the attitude error is large. The weighting function W_{t2} can be designed to guarantee robustness against only the residual mode r. The selected weighting function W_{t2} is defined as

$$W_{t2}(s) = \frac{0.001s + 1000}{3500s + 1000} \ . \tag{4.42}$$

The frequency responses of the chosen weighting function W_{t2} and the residual mode r are shown in Fig. 4.8. The residual mode r has a maximum singular value at four frequency bands (3.96, 11.92, 12.57, and 17.45 Hz). To guarantee the robustness of the controller against the low-dimensional parameterization, the weighting function W_{t2} (Eq. (4.42)) is designed such that the singular values of W_{t2} are larger than the singular value of the residual mode r in all frequency bands.

The weighting function W_s is designed to be large in the low frequency band because the system requires the convergence to the target state to be highly accurate. This design of the weighting function W_s guarantees control in the low frequency band. W_s is given in the form of a transfer function as

$$W_s = \frac{10000}{50000s + 1} \ . \tag{4.43}$$

The weighting functions W_s, W_{t1}, and W_{t2} are designed to satisfy the mixed sensitivity problem. If $||W_s \boldsymbol{S}(s)||_\infty$ is less than one and is made to be as small as possible, controllability can be guaranteed by the small gain theorem. Furthermore, if $||W_t \boldsymbol{T}(s)||_\infty$ is less

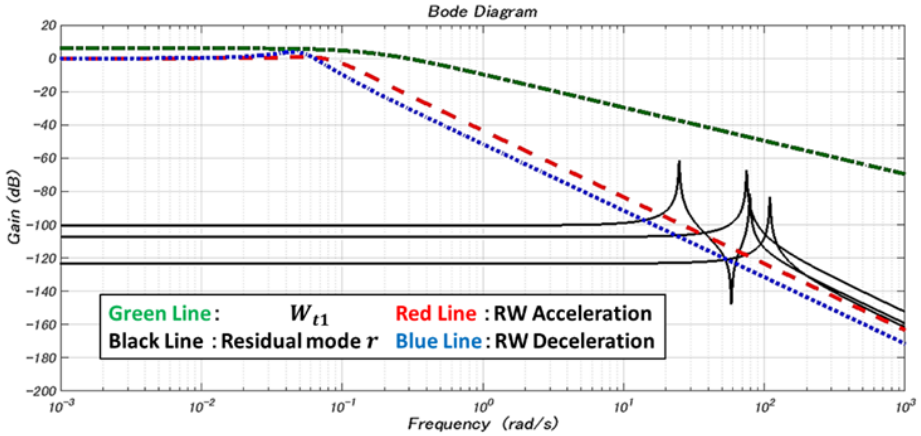

Figure 4.7: Frequency responses of W_{t1}, wheel dynamics, and residual mode r.

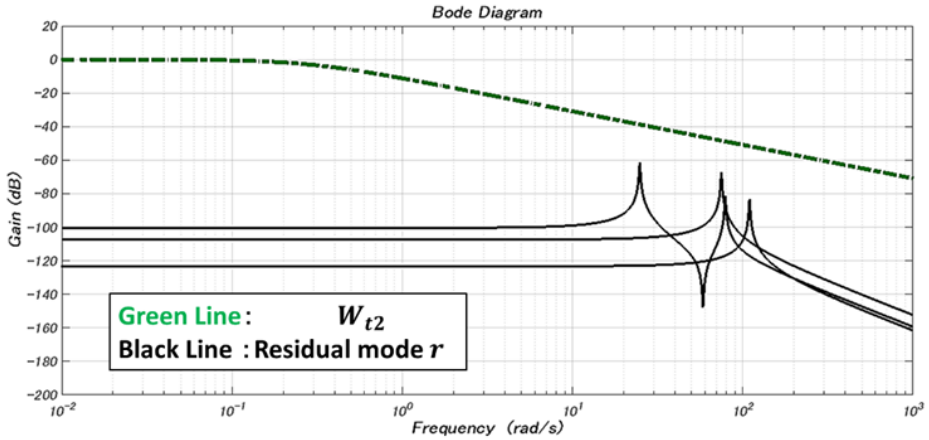

Figure 4.8: Frequency responses of W_{t2} and residual mode r.

than one and is made to be as small as possible, the robustness against the modeling error can be guaranteed by the small gain theorem. To prove that the small gain theorem holds, Figs. 4.9-4.12 show the frequency responses of the above weighting functions and the transfer functions $\boldsymbol{S}$ and $\boldsymbol{T}$.

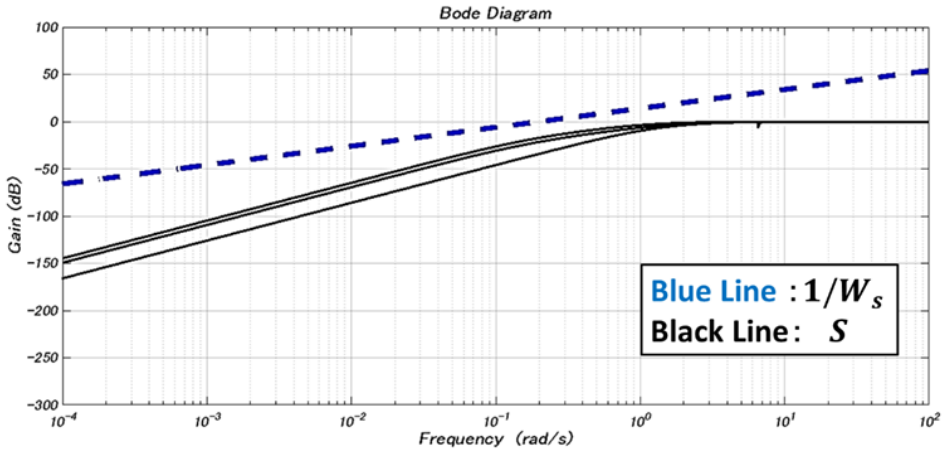

Figure 4.9: Frequency responses of $1/W_s$ and S when the RW mode is activated.

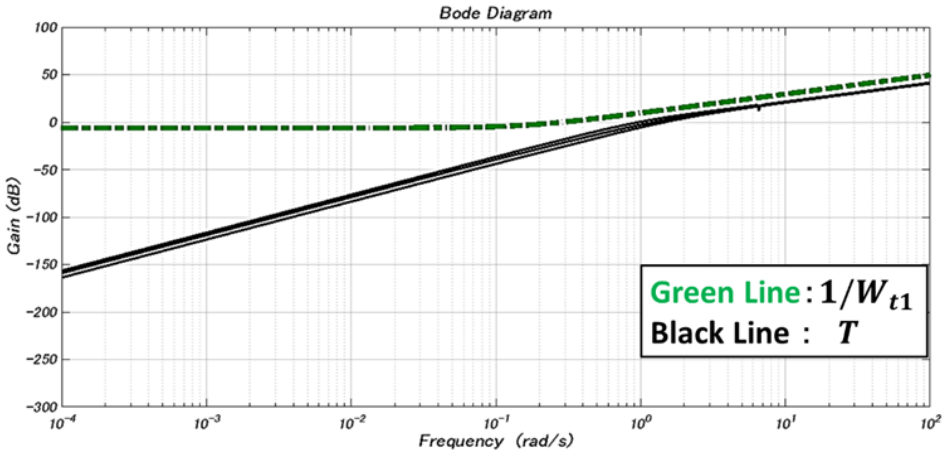

Figure 4.10: Frequency responses of $1/W_{t1}$ and T when the RW mode is activated.

The weighting functions W_s, W_{t1}, and W_{t2}, which are used to design the LMI-based H_∞ controller, satisfy the mixed sensitivity problem. Therefore, the LMI-based H_∞

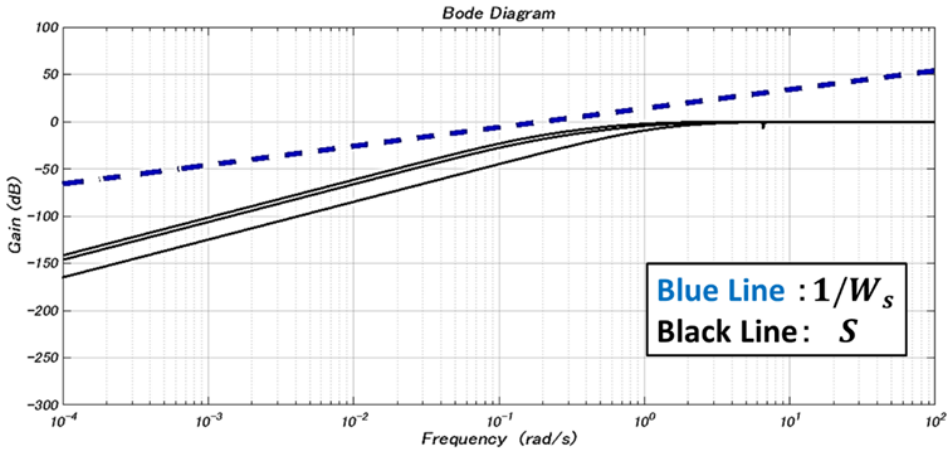

Figure 4.11: Frequency responses of $1/W_s$ and S when the CMG mode is activated.

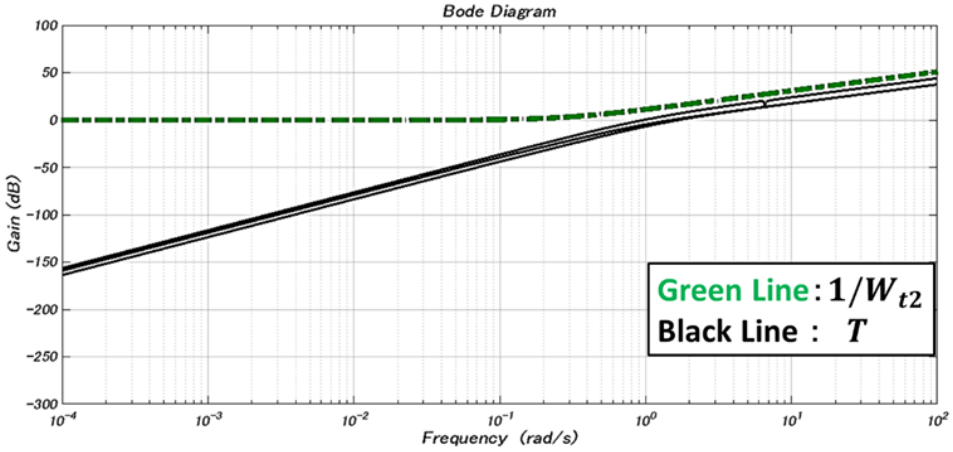

Figure 4.12: Frequency responses of $1/W_{t2}$ and T when the CMG mode is activated.

controller, which use these weighting functions, can guarantee high robustness and controllability. Finally, the equations for the generalized plant can be expressed in the state space form as

$$\dot{\boldsymbol{x}} = \begin{bmatrix} \boldsymbol{A}_c & \boldsymbol{0}_{8\times3} & \boldsymbol{0}_{8\times3} \\ \boldsymbol{B}_s\boldsymbol{C}_c & \boldsymbol{A}_s & \boldsymbol{0}_{3\times3} \\ \boldsymbol{0}_{3\times8} & \boldsymbol{0}_{3\times3} & \boldsymbol{A}_t \end{bmatrix} \boldsymbol{x} + \begin{bmatrix} \boldsymbol{0}_{8\times3} \\ \boldsymbol{B}_s \\ \boldsymbol{0}_{3\times3} \end{bmatrix} \boldsymbol{\varpi} + \begin{bmatrix} \boldsymbol{B}_c \\ \boldsymbol{0}_{3\times3} \\ \boldsymbol{B}_t \end{bmatrix} \boldsymbol{u} \ , \tag{4.44}$$

$$\boldsymbol{z} = \begin{bmatrix} \boldsymbol{0}_{3\times8} & \boldsymbol{0}_{3\times3} & \boldsymbol{C}_t \\ \boldsymbol{D}_s\boldsymbol{C}_c & \boldsymbol{C}_s & \boldsymbol{0}_{3\times3} \end{bmatrix} \boldsymbol{x} + \begin{bmatrix} \boldsymbol{0}_{3\times3} \\ \boldsymbol{D}_s \end{bmatrix} \boldsymbol{\varpi} + \begin{bmatrix} \boldsymbol{D}_t \\ \boldsymbol{0}_{3\times3} \end{bmatrix} \boldsymbol{u} \ , \tag{4.45}$$

$$\boldsymbol{y} = \begin{bmatrix} \boldsymbol{C}_c & \boldsymbol{0}_{3\times3} & \boldsymbol{0}_{3\times3} \end{bmatrix} \boldsymbol{x} + \boldsymbol{\varpi} \ . \tag{4.46}$$

4.7.1 Linear matrix inequality

The control theorem for the linear matrix inequality differs from the previous control theorem. The previous control theorem obtained a controller using the calculation formula, which was solved analytically. Conversely, the control theorem for the linear matrix inequality obtains a controller by numerically solving the inequality of the control algorithm. Furthermore, though the multi-objective control problem is difficult to solve analytically, an LMI-based controller can be used for this problem. In this section, controller design is considered as a multi-objective control problem. To solve such a problem, a mixed H_2/H_∞ control is considered. The state feedback controller $\boldsymbol{K}_\infty$ is expressed as

$$\boldsymbol{K}_\infty = \boldsymbol{Y}\boldsymbol{X}^{-1} \ . \tag{4.47}$$

Furthermore, the closed-loop system is derived by combining the generalized plant and the controller $\boldsymbol{K}_\infty$. The state equation for the closed-loop system can be expressed as

$$\dot{\boldsymbol{x}}_{close}(t) = \boldsymbol{A}_{cl}\boldsymbol{x}_{close}(t) + \boldsymbol{B}_{cl}\boldsymbol{\varpi}(t) \ , \tag{4.48}$$

$$\boldsymbol{z}_{s,t}(t) = \boldsymbol{C}_{cl}\boldsymbol{x}_{close}(t) + \boldsymbol{D}_{cl}\boldsymbol{\varpi}(t) \ , \tag{4.49}$$

$$\begin{bmatrix} \boldsymbol{A}_{cl} & \boldsymbol{B}_{cl} \\ \boldsymbol{C}_{cl} & \boldsymbol{D}_{cl} \end{bmatrix} = \begin{bmatrix} \boldsymbol{A} + \boldsymbol{B}_2\boldsymbol{K}_\infty & \boldsymbol{B}_1 \\ \boldsymbol{C}_{1,2} + \boldsymbol{D}_{12,22}\boldsymbol{K}_\infty & \boldsymbol{D}_{11,21} \end{bmatrix} \ . \tag{4.50}$$

The LMI conditions for the above closed-loop system can be expressed as

$$\begin{bmatrix} He(\boldsymbol{AX}+\boldsymbol{B}_2\boldsymbol{Y}) & \boldsymbol{B}_1 & (\boldsymbol{C}_1\boldsymbol{X}+\boldsymbol{D}_{12}\boldsymbol{Y})^T \\ \boldsymbol{B}_1^T & -\boldsymbol{I}_{n_\varpi} & \boldsymbol{D}_{11}^T \\ \boldsymbol{C}_1\boldsymbol{X}+\boldsymbol{D}_{12}\boldsymbol{Y} & \boldsymbol{D}_{11} & -\boldsymbol{I}_{n_{z_t}} \end{bmatrix} < 0 \,, \tag{4.51}$$

$$\begin{bmatrix} He(\boldsymbol{AX}+\boldsymbol{B}_2\boldsymbol{Y}) & (\boldsymbol{C}_2\boldsymbol{X}+\boldsymbol{D}_{22}\boldsymbol{Y})^T \\ \boldsymbol{C}_2\boldsymbol{X}+\boldsymbol{D}_{22}\boldsymbol{Y} & -\boldsymbol{I}_{n_{z_s}} \end{bmatrix} < 0 \,, \tag{4.52}$$

$$\begin{bmatrix} \boldsymbol{\Xi} & \boldsymbol{B}_1^T \\ \boldsymbol{B}_1 & \boldsymbol{X} \end{bmatrix} > 0, \mathrm{trace}(\boldsymbol{\Xi}) < \gamma_2^2 \tag{4.53}$$

where $\boldsymbol{X} \in \mathcal{R}^{14\times 14}$ and $\boldsymbol{Y} \in \mathcal{R}^{n_u\times 14}$ are the matrices to solve the LMI conditions. The evaluation output $\boldsymbol{z}_t$ is evaluated by the H_∞ norm. Equation (4.51) shows the LMI condition for the evaluation output $\boldsymbol{z}_t$ with reference to the robustness. The evaluation output $\boldsymbol{z}_s$ is evaluated by the H_2 norm. Equations (4.52) and (4.53) show the LMI condition for the evaluation output $\boldsymbol{z}_s$ with reference to the controllability. The necessary and sufficient condition for the existence of the controller $\boldsymbol{K}_\infty$ is that it fulfills the LMI conditions of Eqs. (4.51), (4.52), and (4.53). If these LMI conditions are solvable, the desired controller $\boldsymbol{K}_\infty$ that stabilizes the closed-loop system G_{close} is obtained. The obtained controller generates the command control torque to maneuver the attitude of the spacecraft. As mentioned earlier, the three weighting functions are designed for different purposes in accordance with their use. Therefore, the controllers $\boldsymbol{K}_\infty$ should be designed for two patterns in accordance with these two weighting functions to generate the desired command control torque. However, because the controllers $\boldsymbol{K}_\infty$ are designed using linear control design methods, they should be used for a short time at the beginning and near the end of a maneuver. The quaternion feedback controller (Eq. (4.32)) is used to determine the command torques for the attitude maneuvering of the spacecraft instead of the H_∞ controller during the period in which the H_∞ controller is not applied.

4.8 Gain-Scheduled Steering Law for VSCMG

To realize the command control torque demanded by the controllers, the steering law for the VSCMG system is considered. The gain-scheduled steering control law for the VSCMG system consists of a GSR term and an LG term, which are weighted by weighting matrices. These weighting matrices are related to the CMG and RW modes, and the elements in these matrices vary according to the attitude error and condition number for the Jacobian matrix.

4.8.1 Singularity-robust inverse

If the pyramid-array four-CMG system is used as the torque generator, it is necessary to consider the singularity problem for the CMG system. The steering control laws for the pyramid-array four-CMG system must avoid singularities. The GSR law ([10, 12]) is one of the most popular steering laws used to avoid singularities in a CMG system. The GSR law for VSCMGs can be expressed as

$$\begin{bmatrix} \dot{\boldsymbol{\delta}} \\ \dot{\boldsymbol{\Omega}} \end{bmatrix} = \boldsymbol{W}_1 \boldsymbol{Q}^T (\boldsymbol{Q}\boldsymbol{W}_1\boldsymbol{Q}^T + H_0^2 \lambda \boldsymbol{E}_r)^{-1} \dot{\boldsymbol{h}} \tag{4.54}$$

where $\boldsymbol{W}_1$ is a weighting matrix $\in \mathcal{R}^{8\times 8}$ and $\boldsymbol{E}_r$ is a perturbation matrix for singularity avoidance given by

$$\boldsymbol{W}_1 = \begin{bmatrix} \boldsymbol{I}_4 & \boldsymbol{0}_{4\times 4} \\ \boldsymbol{0}_{4\times 4} & \boldsymbol{I}_4 \end{bmatrix}, \ \boldsymbol{E}_r = \begin{bmatrix} 1 & \epsilon_3 & \epsilon_2 \\ \epsilon_3 & 1 & \epsilon_1 \\ \epsilon_2 & \epsilon_1 & 1 \end{bmatrix} . \tag{4.55}$$

The parameters λ and ϵ_i are set to appropriate values to avoid singularities:

$$\lambda = \lambda_0 \exp(-\mu \det(\boldsymbol{C}\boldsymbol{C}^T)/H_0^2), \lambda_0 > 0, \ \mu > 0 \, , \tag{4.56}$$

$$\epsilon_i = \epsilon_0 \sin(\tau t + \varphi_i) \tag{4.57}$$

where λ_0, ε_0, τ, and φ_i are the value, amplitude, modulation frequency, and phase that must be chosen appropriately for the perturbation.

4.8.2 Local gradient-based steering law

The singularity avoidance control laws can achieve more effective avoidance if they use a null motion, which has no effect on the generated output torque. Such steering control laws are commonly known as the local gradient method, and that for the VSCMG is given by

$$\begin{bmatrix} \dot{\boldsymbol{\delta}} \\ \dot{\Omega} \end{bmatrix} = \boldsymbol{W}_1\boldsymbol{Q}^T\left(\boldsymbol{Q}\boldsymbol{W}_1\boldsymbol{Q}^T + H_0^2\lambda\boldsymbol{E}_r\right)^{-1}\dot{\boldsymbol{h}} + \begin{bmatrix} (\boldsymbol{I}_4 - \boldsymbol{W}_2\boldsymbol{C}^T(\boldsymbol{C}\boldsymbol{W}_2\boldsymbol{C}^T)^{-1}\boldsymbol{C})\boldsymbol{W}_2\boldsymbol{d}_1 \\ \boldsymbol{0}_4 \end{bmatrix}, (\boldsymbol{d}_1 \in \mathcal{R}^{4\times 1}) \quad (4.58)$$

where $\boldsymbol{W}_1$ and $\boldsymbol{W}_2$ are weighting matrices and $\boldsymbol{d}_1$ is an arbitrary vector. This vector should be selected appropriately to effectively avoid CMG singularities.

4.8.3 Gain-scheduled steering law for VSCMGs

The gain-scheduled steering control law for the VSCMGs consists of the GSR and LG terms. In the previously mentioned local gradient-based steering law for the VSCMG, the gradient-based null motion is employed to steer the CMG gimbal angles toward suitable values in which the RW mode is effectively available for the precise stabilization of the spacecraft attitude at the target attitude near the end of a maneuver. Conversely, the gradient-based null motion in past studies is employed to maintain the condition number for the CMG Jacobian at as small a value as possible, which is intended to increase the availability of the CMG mode as much as possible. This gain-scheduled steering control law can be expressed as

$$\begin{bmatrix} \dot{\boldsymbol{\delta}} \\ \dot{\Omega} \end{bmatrix} = \boldsymbol{W}_1\boldsymbol{Q}^T\left(\boldsymbol{Q}\boldsymbol{W}_1\boldsymbol{Q}^T + H_0^2\lambda\boldsymbol{E}_r\right)^{-1}\dot{\boldsymbol{h}} + \begin{bmatrix} (\boldsymbol{I}_4 - \boldsymbol{W}_2\boldsymbol{C}^T(\boldsymbol{C}\boldsymbol{W}_2\boldsymbol{C}^T)^{-1}\boldsymbol{C})\boldsymbol{W}_2\boldsymbol{d}_1 \\ \boldsymbol{0}_4 \end{bmatrix}, (\boldsymbol{d}_1 \in \mathcal{R}^{4\times 1}) \quad (4.59)$$

$$\boldsymbol{W}_1 = \begin{bmatrix} w_1(\hat{\boldsymbol{q}})\boldsymbol{I}_4 & \boldsymbol{0}_{4\times4} \\ \boldsymbol{0}_{4\times4} & w_2(\hat{\boldsymbol{q}},\kappa_2)\boldsymbol{I}_4 \end{bmatrix}, \ \boldsymbol{W}_2 = \boldsymbol{I}_4 \tag{4.60}$$

where w_1 and w_2 are given in the form of a sigmoid function of the attitude error and the condition number to transition the steering controller between the CMG and RW modes as follows:

$$w_1(\hat{\boldsymbol{q}}) = \frac{1}{1+e^{-a(|\hat{\boldsymbol{q}}|-\varsigma_1)}}, \tag{4.61}$$

$$w_2(\hat{\boldsymbol{q}},\kappa_2) = \frac{1}{1+e^{a(|\hat{\boldsymbol{q}}|-\varsigma_1)}} \cdot \frac{1}{1+e^{b(\kappa_2-\varsigma_2)}} \tag{4.62}$$

where a, b, ς_1, and ς_2 are constant parameters and should be selected appropriately. The weighting parameters w_1 and w_2 are shown in Fig. 4.13. When the attitude error is large, the weighting parameter w_1 is approximately 1, and w_2 is 0. Conversely, when the attitude error and the condition number κ_2 for the RW Jacobian are smaller than 2, w_1 is 0, and w_2 approaches 1. This means that this steering control law can properly use the CMG and RW modes depending on the attitude error and κ_2. Employing the modified weighting matrix described above does not yet guarantee the steering of the gimbal angles such that the system approaches gimbal angles suitable for the RW mode. To steer the gimbal angles to such values, the null motion is chosen for the modified LG term as

$$\begin{bmatrix} \dot{\boldsymbol{\delta}} \\ \dot{\boldsymbol{\Omega}} \end{bmatrix}_{null} = \begin{bmatrix} [\boldsymbol{I}_4 - \boldsymbol{W}_2\boldsymbol{C}^T(\boldsymbol{C}\boldsymbol{W}_2\boldsymbol{C}^T)^{-1}\boldsymbol{C}]\boldsymbol{W}_2\boldsymbol{d}_2 \\ \boldsymbol{0}_4 \end{bmatrix}, \tag{4.63}$$

$$\boldsymbol{d}_2 = -k\, w_3(\hat{\boldsymbol{q}}) \left(\frac{\partial\kappa_2}{\partial\boldsymbol{\delta}}\right)^T, \tag{4.64}$$

$$w_3(\hat{\boldsymbol{q}}) = \frac{1}{1+e^{a(|\hat{\boldsymbol{q}}|-\varsigma_1)}} \tag{4.65}$$

where w_3 is a sigmoid function that activates the null motion only near the end of a maneuver. Because the null motion is necessary to steer the gimbal angles toward the suitable gimbal angles for the RW mode, w_3 is selected to activate the null motion near the end of a maneuver.

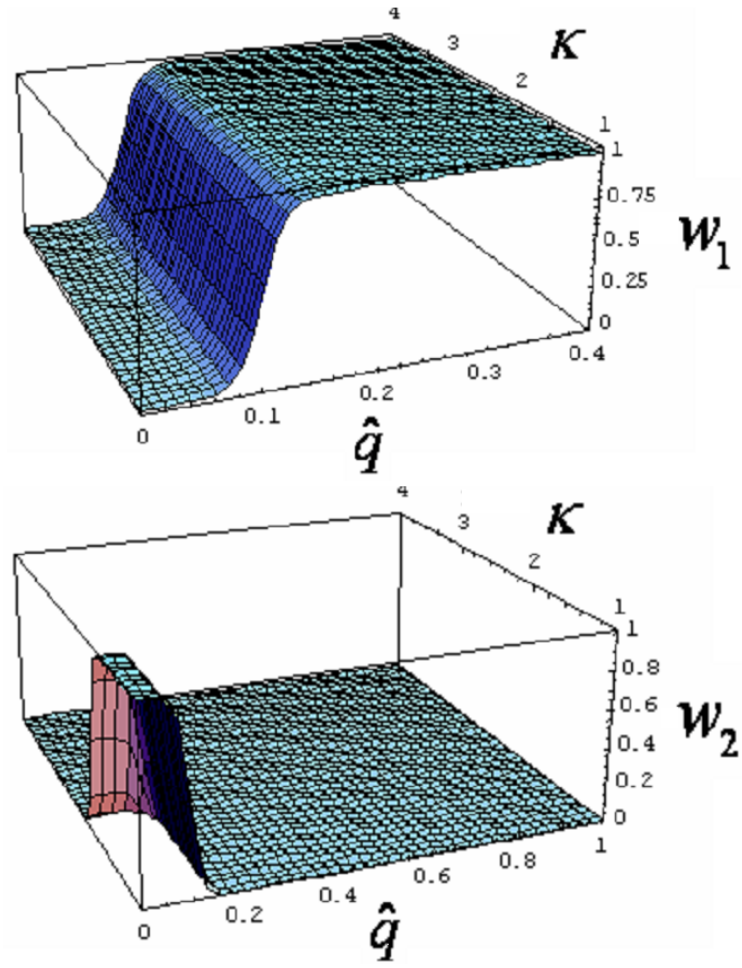

Figure 4.13: Weighting parameters w_1 and w_2.

4.9 Numerical Simulations

4.9.1 Simulation conditions

Numerical simulations are conducted to validate the effectiveness of the proposed control law that generates the VSCMG command control torque. Two cases are considered: Cases 1 and 2. In Case 1, the quaternion feedback control law is used to generate the command control torque over all time without considering the flexible structures. In Case 2, the attitude maneuvers are divided into three phases to use the LMI-based H_∞ and quaternion feedback controllers. In the first phase, the LMI-based H_∞ controller for the CMG mode is used to generate the command control torque at the beginning of the maneuver until the difference between the command control torque by the LMI-based H_∞ controller and the quaternion feedback controller approaches 0. In the second phase, the quaternion controller is used instead of the LMI-based H_∞ controller. Finally, in the third phase, the LMI-based H_∞ controller for the RW mode is used when the quaternion error is less than 0.01. The gain-scheduled steering control law for the VSCMG is used in both cases. In the simulations, the initial angular velocities and the attitude of the satellite are set to 0 and $\boldsymbol{q}_s = (-1, 0, 0, 0)^T$, respectively, and the goal attitude is set to $\boldsymbol{q}_g = (0, 0, 0, 1)^T$. The parameters used for the simulations are listed in Table 4.4, which includes the parameters for the gain-scheduled steering law for the VSCMG to transfer from the CMG mode to the RW mode with respect to the attitude error and condition number, and the dimension numbers of matrices and vectors. The modal parameters listed in Table 4.3 are used for the numerical simulations. From these modal parameters, H_∞ controllers are obtained by solving the LMI condition. The designed controller gains are given in the Appendix of this chapter.

4.10 Simulation Results

First, the results for the quaternion feedback controller (Case 1) are shown as a reference for comparison with those for the newly proposed control law. Figures 4.14-4.17

Table 4.4: Simulation parameters.

Parameters	Values (unit)
$\boldsymbol{\delta}(0)$	$[0, 0, 0, 0]^T$ (rad)
$\dot{\boldsymbol{\delta}}(0)$	$[0, 0, 0, 0]^T$ (rad/s)
$\dot{\delta}_{max}$	0.32 (rad/s)
H_0	0.044 (Nms)
$\boldsymbol{J}$	diag(1.5, 0.65, 1.1)(Kgm^2)
$\boldsymbol{K}_p$	$0.09\boldsymbol{I}_3$
$\boldsymbol{K}_d$	$0.4242\boldsymbol{I}_3$
k	0.001
$\lambda_0, \mu, \varepsilon_0, \tau$	0.0105, 10.5, 0.01, 0.5
$\varphi_1, \varphi_2, \varphi_3$	0, $\pi/2$, π
a, b	200, 20
ς_1, ς_2	0.01, 5
$n, n_c, n_r, n_u, n_\varpi, n_{z_s}, n_{z_t}$	5, 4, 4, 3, 3, 3, 3

show the time responses of the quaternions, angular velocity, gimbal angles, and wheel rate, respectively. Quaternion 1 for the spacecraft approached 0 at approximately 60 s, at which point the wheel speed began to change smoothly. Because the quaternion error became small, the weighting parameter w_2 for the gain scheduled steering control law reached 1 at approximately 60 s. Furthermore, the null motion steered the gimbal angles toward suitable values for the RW mode. Therefore, the steering control law is intended to activate the RW mode instead of the CMG mode near the end of the maneuver. However, the quaternions failed to converge to 0 because the angular velocities also failed to converge to 0, as shown in Fig. 4.15. This is because the influence of the vibration and the second-order system of the wheel dynamics prevented the RW mode from stabilizing the attitude of the spacecraft. Furthermore, because the in-plane and torsional vibrations of the flexible structure were ignored as a residual mode, quaternions 2 and 3 became unstable. To stabilize the quaternions again, the RW mode ensured continual variation in the wheel speed of all the wheels at the end of the maneuver. These numerical results show that the gain-scheduled steering law can smoothly transition between the CMG and RW modes by using the weighting functions. However, these numerical results also demonstrate that the quaternion feedback control law without considering flexible structures did not show good convergence performance, because the vibration and the second-order system of the wheel dynamics interfered with the RW mode and the ignored residual mode affected quaternions 2 and 3.

Next, the results for the proposed control law (Case 2) are shown. Figures 4.18-4.22 show the time responses of the quaternions, angular velocity, gimbal angles, wheel rate, and influence of vibration, respectively. At the beginning of the maneuver, the LMI-based H_∞ controller for the CMG mode was used instead of the quaternion feedback controller to generate the command control torque for approximately 0.5 s until the difference between the command control torque by the LMI-based H_∞ controller and the quaternion feedback controller approached 0. After that, the quaternion controller was used to generate the command control torque until the LMI-based H_∞ controller for the RW mode was activated at approximately 50 s. Quaternion 1 for the spacecraft approached

0 at approximately 50 s. The wheel speed began to change smoothly at approximately 50 s. Because the quaternion error became small, the weighting parameter w_2 for the gain scheduled steering control law reached 1 at approximately 50 s. Furthermore, the null motion steered the gimbal angles toward suitable values for the RW mode. Therefore, the steering control law is intended to activate the RW mode instead of the CMG mode near the end of the maneuver. The LMI-based H_∞ controller for the RW mode was used instead of the quaternion feedback controller to generate the command control torque from 50 to 400 s. The quaternions quickly converged to 0 at approximately 60 s and remained at 0 until the end of the simulation. The proposed control law shows good convergence performance, which can be explained primarily by the following two factors. Because the weighting function W_s effectively guarantees the controllability and the weighting function W_t effectively guarantees robustness against the second-order system of the wheel dynamics and the in-plane and torsional vibration of the flexible structure as a residual mode, the RW mode was properly activated to stabilize the attitude near the end of the maneuver and suppress the vibration. Therefore, because the wheel speeds changed after the convergence of the quaternions, the very small residual vibration was absorbed slowly by the RW mode after the convergence of the quaternions. Figure 4.22 shows the influence of vibration along the x-axis to compare Cases 1 and 2. Figure 4.22(a) shows the effectiveness of the LMI-based H_∞ controller in the first phase, during which the vibration was suppressed by the controller. The influence of the vibration on the angular velocities along the x-axis for Case 1 is approximately three times that for Case 2 from 15 to 35 s. Figure 4.22(b) shows the effectiveness of the LMI-based H_∞ controller in the third phase, during which the vibration was suppressed by the controller. The influence of the vibration on the angular velocities along the x-axis in Case 1 is four times that for Case 2 starting from 60 to 110 s. Figure 4.23 shows the influence of the robustness and controllability about the y- and z-axes to compare Cases 1 and 2. Figure 4.23 shows the effectiveness of LMI-based H_∞ controller in the third phase, during which the angular velocities about the y- and z-axes in Case 2 converged to 0 as a result of the LMI-based H_∞ controller taking into consideration the residual mode and the

characteristics of the wheel dynamics. In contrast to the angular velocities about the y- and z-axes in Case 2, those in Case 1 did not converge to 0, because the robustness and controllability of Case 1 were less than those of Case 2. Based on the differences in the robustness, controllability, and vibration suppression performance, the settling time for Case 2 was shorter than that for Case 1. These numerical results demonstrate that the gain-scheduled steering law can smoothly transition between the CMG and RW modes by using the proposed weighting functions. Furthermore, these results show that the proposed control law is effective in terms of the convergence performance and vibration suppression of flexible structures using H_∞ methods to guarantee high robustness and controllability for the VSCMG system.

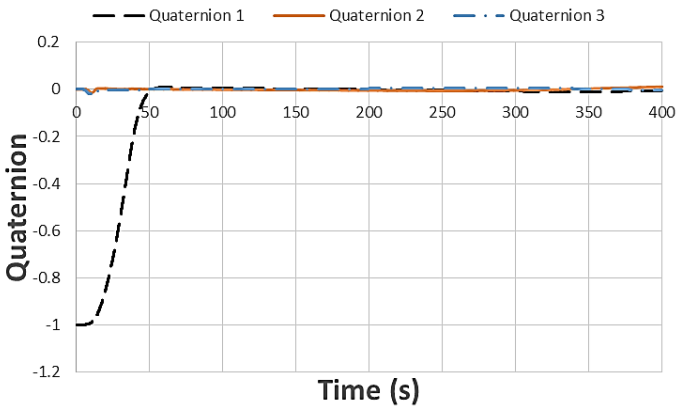

Figure 4.14: Time response of quaternions in Case 1.

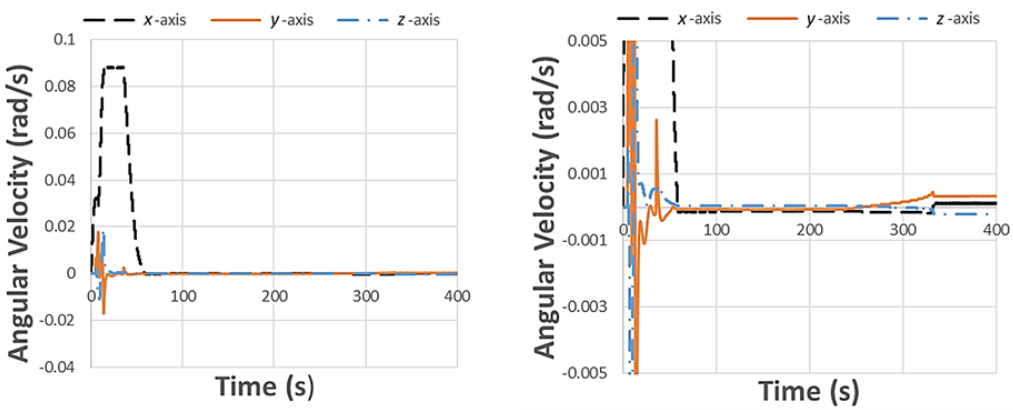

(a) (b)

Figure 4.15: Time response of angular velocity in Case 1: (a) view including the maximum and minimum values and (b) magnified view.

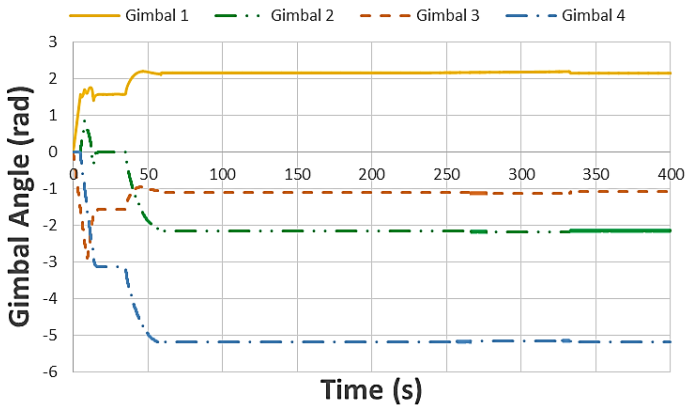

Figure 4.16: Time response of gimbal angles in Case 1.

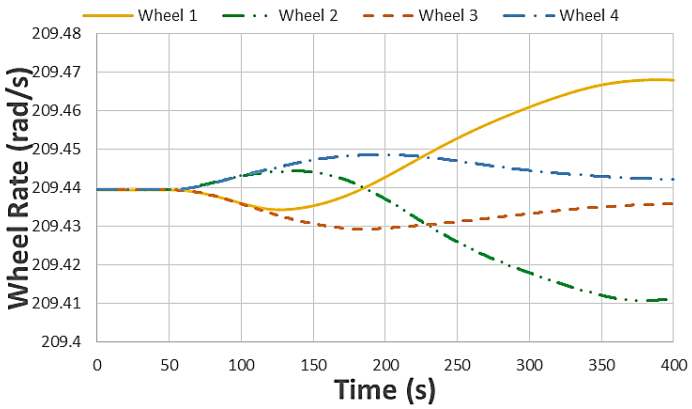

Figure 4.17: Time response of wheel rate in Case 1.

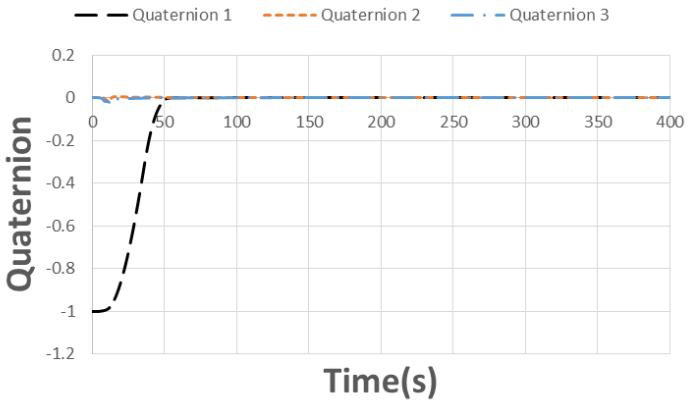

Figure 4.18: Time response of quaternions in Case 2.

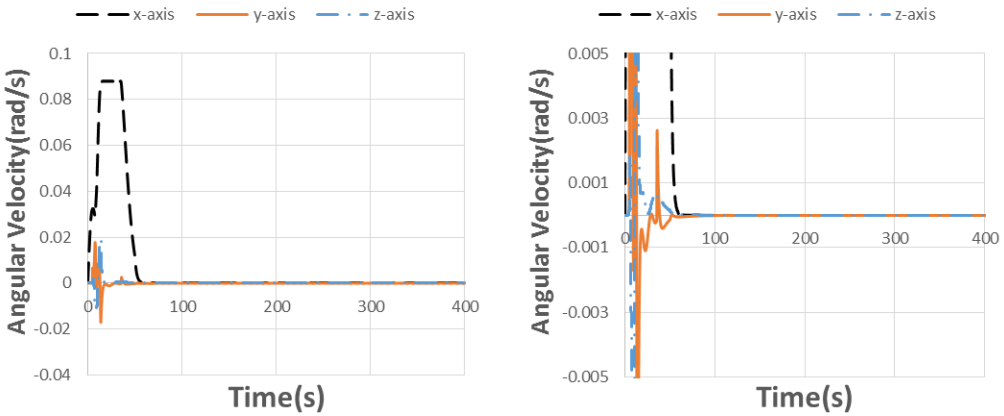

(a) (b)

Figure 4.19: Time response of angular velocity in Case 2: (a) view including the maximum and minimum values and (b) magnified view.

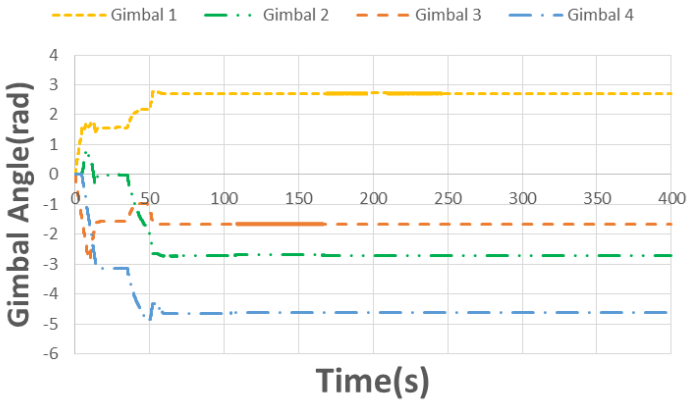

Figure 4.20: Time response of gimbal angles in Case 2.

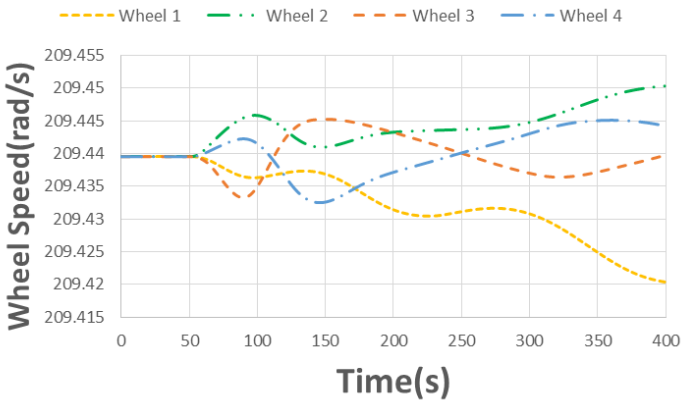

Figure 4.21: Time response of wheel rate in Case 2.

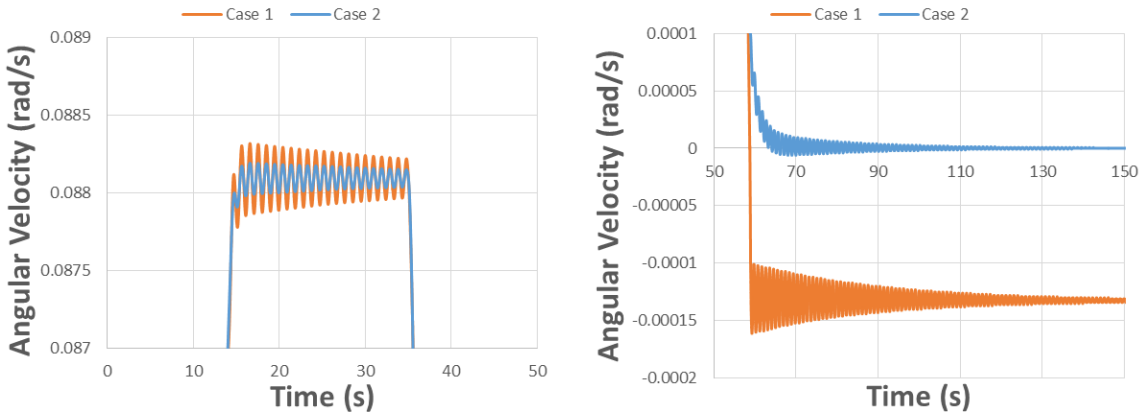

(a) (b)

Figure 4.22: Influence of vibration on motion about the x-axis: (a) magnified view of angular velocity after first phase and (b) view during third phase.

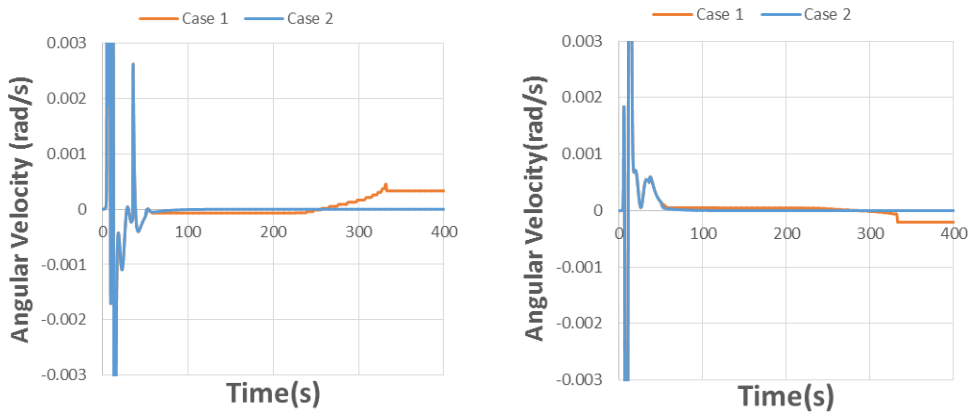

(a) (b)

Figure 4.23: Influence of vibration on motion about the (a) y- and (b) z-axes.

4.11 Conclusion

VSCMGs have functions of both CMGs and RWs. When the attitude error is large, the CMG mode is activated because it has a more powerful torque output than the RW mode. Conversely, the RW mode is activated near the end of a maneuver because the RW mode generates a more precise torque output than the CMG mode. To fully derive the performance of this VSCMG system for spacecraft equipped with flexible structures, H_∞ methods are considered. H_∞ methods are used in modern control theory to design controllers that can achieve stabilization with guaranteed control performance. The LMI-based controller design method is used to obtain the desired controller by solving a convex optimization even if the control system and the requirement are complicated. In this paper, an LMI-based control law of the VSCMGs is proposed for a flexible spacecraft. The proposed control law is designed using H_∞ synthesis via LMI, considering the characteristics of the VSCMG system, the RW, and vibration suppression. Furthermore, to realize the command control torque generated by the abovementioned controller, it was desirable for the steering law to use the CMG mode for fast attitude maneuvering when the attitude error was large and the RW mode for vibration suppression and pre-

cise attitude stabilization in the target direction when the attitude error was small. To achieve a smooth mode transition in the VSCMG system, the gain-scheduled steering law for the VSCMG system was proposed.

The numerical results show that the proposed control law effectively stabilizes the spacecraft and suppresses vibration. The two weighting functions obtained by the H_∞ methods guarantee the high robustness and controllability of the VSCMG system for the attitude control problem of a spacecraft equipped with flexible structures. The gain-scheduled steering law could smoothly transition between the CMG and RW modes based on the attitude error and condition number.

In the future work, experiments will be conducted to validate the effectiveness of this proposed control law. Furthermore, this control law will be extended to an adaptive skew CMG system. If a new hybrid CMG system that consists of the VSCMG and an adaptive skew CMG system is used, the developed control law will demonstrate more effective stabilization and vibration suppression and faster convergence performance than the proposed control law.

Appendix: Generalized Plant and Control Gains

The generalized plant are given as

$$\dot{\boldsymbol{x}} = \boldsymbol{A}\boldsymbol{x} + \boldsymbol{B}_1\boldsymbol{\varpi} + \boldsymbol{B}_2\boldsymbol{u} \,, \tag{4.66}$$

$$\boldsymbol{z}_t = \boldsymbol{C}_1 x + \boldsymbol{D}_{11}\boldsymbol{\varpi} + \boldsymbol{D}_{12}\boldsymbol{u} \,, \tag{4.67}$$

$$\boldsymbol{z}_s = \boldsymbol{C}_2 x + \boldsymbol{D}_{21}\boldsymbol{\varpi} + \boldsymbol{D}_{22}\boldsymbol{u} \,. \tag{4.68}$$

The matrices $\boldsymbol{A}$, $\boldsymbol{B}_1$, $\boldsymbol{B}_2$, $\boldsymbol{C}_1$, $\boldsymbol{C}_2$, and $\boldsymbol{D}_{ij}, (i,j=1,2)$ for the generalized plant for the three axes are obtained as follows:

$$\boldsymbol{A} = \begin{bmatrix} \boldsymbol{A}_c & \boldsymbol{0}_{8\times3} & \boldsymbol{0}_{8\times3} \\ \boldsymbol{B}_s\boldsymbol{C}_c & \boldsymbol{A}_s & \boldsymbol{0}_{3\times3} \\ \boldsymbol{0}_{3\times8} & \boldsymbol{0}_{3\times3} & \boldsymbol{A}_t \end{bmatrix} , \tag{4.69}$$

$$\boldsymbol{A}_c = \begin{bmatrix} \boldsymbol{0}_{4\times4} & \boldsymbol{I}_4 \\ \mathrm{diag}(0,0,0,-42.9) & \mathrm{diag}(0,0,0,-6.55\times10^{-2}) \end{bmatrix} , \tag{4.70}$$

$$\boldsymbol{A}_s = -2.0\times10^{-5}\boldsymbol{I}_3 , \tag{4.71}$$

$$\boldsymbol{A}_t = \begin{cases} -0.16\boldsymbol{I}_3 & (\text{for } W_{t1}) \\ -0.29\boldsymbol{I}_3 & (\text{for } W_{t2}) \end{cases} , \tag{4.72}$$

$$\boldsymbol{B}_s\boldsymbol{C}_c = [\mathrm{diag}(0.41,0.67,0.48)\ \mathrm{diag}(-0.12,0,0)\ \ \boldsymbol{0}_{3\times1}] , \tag{4.73}$$

$$\boldsymbol{B}_1 = \begin{bmatrix} \boldsymbol{0}_{8\times3} \\ 0.5\boldsymbol{I}_3 \\ \boldsymbol{0}_{3\times3} \end{bmatrix} , \tag{4.74}$$

$$\boldsymbol{B}_2 = \begin{bmatrix} \boldsymbol{0}_{4\times3} \\ \mathrm{diag}(0.82,1.24,0.95) \\ \mathrm{diag}(-0.24,0,0) \\ \boldsymbol{0}_{1\times3} \\ 0.5\boldsymbol{I}_3 \end{bmatrix} , \tag{4.75}$$

$$\boldsymbol{C}_1 = \begin{cases} \begin{bmatrix} \boldsymbol{0}_{3\times11} & 0.67\boldsymbol{I}_3 \end{bmatrix} & (\text{for } W_{t1}) \\ \\ \begin{bmatrix} \boldsymbol{0}_{3\times11} & 0.57\boldsymbol{I}_3 \end{bmatrix} & (\text{for } W_{t2}) \end{cases} , \tag{4.76}$$

$$\boldsymbol{C}_2 = \begin{bmatrix} \boldsymbol{0}_{3\times8} & 0.4\boldsymbol{I}_3 & \boldsymbol{0}_{3\times3} \end{bmatrix} , \tag{4.77}$$

$$\boldsymbol{D}_{11} = \boldsymbol{0}_{3\times3} , \tag{4.78}$$

$$\boldsymbol{D}_{12} = 1.67\boldsymbol{I}_3 , \tag{4.79}$$

$$\boldsymbol{D}_{21} = \boldsymbol{0}_{3\times3} , \tag{4.80}$$

$$\boldsymbol{D}_{22} = \boldsymbol{0}_{3\times3} . \tag{4.81}$$

The linear matrix inequality-based H_∞ controller for the two weighting functions W_{t1} and W_{t2} is shown. The state feedback controller $\boldsymbol{K}_\infty$ is expressed as

$$\boldsymbol{K}_\infty = \boldsymbol{Y}\boldsymbol{X}^{-1} \, . \tag{4.82}$$

In the case of the weighting function W_{t1}, the state feedback controller components for the three axes are obtained by solving the LMI condition as follows:

$$\boldsymbol{K}_\infty = \begin{bmatrix} -0.029 & 0 & 0 & -2.315 & -0.893 & 0 & 0 & 2.345 \\ 0 & -0.029 & 0 & 0 & 0 & -0.893 & 0 & 0 \\ 0 & 0 & -0.029 & 0 & 0 & 0 & -0.893 & 0 \end{bmatrix} \begin{bmatrix} -0.05 & 0 & 0 & 0.002 & 0 & 0 \\ 0 & -0.05 & 0 & 0 & 0.002 & 0 \\ 0 & 0 & -0.05 & 0 & 0 & 0.002 \end{bmatrix} \tag{4.83}$$

In the case of the weighting function W_{t2}, the state feedback controller components for the three axes are obtained by solving the LMI condition as follows:

$$\boldsymbol{K}_\infty = \begin{bmatrix} -0.03 & 0 & 0 & -1.719 & -0.633 & 0 & 0 & 1.984 \\ 0 & -0.03 & 0 & 0 & 0 & -0.633 & 0 & 0 \\ 0 & 0 & -0.03 & 0 & 0 & 0 & -0.633 & 0 \end{bmatrix} \begin{bmatrix} -0.057 & 0 & 0 & 0.004 & 0 & 0 \\ 0 & -0.057 & 0 & 0 & 0.004 & 0 \\ 0 & 0 & -0.057 & 0 & 0 & 0.004 \end{bmatrix} \tag{4.84}$$

References

[1] Glover, K., and Doyle, C. J.: State-Space Formulae for All Stabilizing Controllers that Satisfy an H_∞ - Norm Bound and Relations to Risk Sensitivity, *Systems & Control Letters*, **11**(1988), pp.167-172.

[2] Doyle, C. J., Glover, K., Khargonekar, P. P., and Francis, A. B.: State-space Solutions to Standard H_2 and H_∞ Control Problems, *Proc.1988 American Control Conference*, Atlanta, *IEEE Trans. on Automatic Control*(1989), pp.34-38.

[3] Doyle, C. J., Francis, A. B., and Tannenbaum, R. A.: Feedback Control Theory, (1992), Macmillan.

[4] Margulies, G., Aubrun, J. N.: Geometric Theory of Single-gimbal Control Moment Gyro System, *Journal of Astronautical Sciences*, **26**(1978), pp.159-191.

[5] Bedrossian, N. S., Paradiso, J., Bergmann, E. V., Rowell, D.: Steering Law Design for Redundant Single-gimbal Control Moment Gyroscopes, *Journal of Guidance, Control and Dynamics*, **13**(1990), pp.1083-1089.

[6] Vadali, S. R., Oh, H. S., Walker, S. R.: Preferred Gimbal Angles for Single Gimbal Control Moment Gyros, *Journal of Guidance, Control, and Dynamics*, **13**(1990), pp.1090-1095.

[7] Paradiso, J. A.: Global Steering of Single Gimbaled Control Moment Gyroscopes using a Directed Search, *Journal of Guidance, Control and Dynamics*, **15**(1992), pp.1236-1244.

[8] Ford, K. A. and Hall, C. D.: Singular Direction Avoidance Steering for Control-moment Gyros, *Journal of Guidance, Control, and Dynamics*, **23**(2000), pp.648-656.

[9] Kurokawa, H.: A Geometric Study of Single Gimbal Control Moment Gyros - Singularity Problems and Steering Law, Technical Report, Mechanical Engineering Laboratory, Japan, No.175, (1998), Jan.

[10] Wie, B., Bailey, D., and Heiberg, C. J.: Singularity Robust Steering Logic for Redundant Single-gimbal Control Moment Gyros, *Journal of Guidance, Control, and Dynamics*, **24**(2001), pp.865-872.

[11] Wie, B.: Singularity Aanalysis and Visualization for Single-gimbal Control Moment Gyros Systems, *Journal of Guidance, Control, and Dynamics*, **27**(2004), pp.271-282.

[12] Wie, B.: Singularity Escape/Avoidance Steering Logic for Control Moment Gyro Systems, *Journal of Guidance, Control, and Dynamics*, **28**(2005), pp.948-956.

[13] Takada, K., Kojima, H.: Receding Horizon Control on Steering of Control Moment Gyro for Fast Attitude Maneuver, *Transactions of the Japan Society for Aeronautical and Space Sciences*, **52**(2009), pp.1-10.

[14] Takada, K., Kojima, H., and Matsuda, N.: Control Moment Gyro Singularity-avoidance Steering Control based on Singular-surface Cost Function, *Journal of Guidance, Control, and Dynamics*, **33**(2010), pp.1442-1450.

[15] Schaub, H. and Junkins, J. L.: Singularity Avoidance using Null Motion and Variable-speed Control Moment Gyros, *Journal of Guidance Control, and Dynamics*, **23**(2000), pp.11-16.

[16] Nanamori, Y., Takahashi, M., Taniwaki, S., Yoshida, K., and Ohkami, Y.: High Accuracy Multi Target Pointing Steering Law of Earth Observation Satellite using Variable-speed Control Moment Gyros, *Proceeding of Dynamics and Design Conference*, 411, (2007) (in Japanese).

[17] McMahon, J. and Schaub, H.: Simplified Singularity Avoidance using Variable-speed Control Moment Gyroscope Null Motion, *Journal of Guidance, Control, and Dynamics*, **32**(2009), pp.1938-1943.

[18] Yoon, H. and Tsiotras, P.: Spacecraft Adaptive Attitude and Power Tracking with Variable Speed Control Moment Gyroscopes, *Journal of Guidance, Control, and Dynamics*, **25**(2002), pp.1081-1090.

[19] Yoon, H. and Tsiotras, P.: Spacecraft Line-of-sight Control using a Single Variable-speed Control Moment Gyro, *Journal of Guidance, Control, and Dynamics*, **29**(2006), pp.1295-1308.

[20] Yoon, H. and Tsiotras, P.: Singularity Analysis of Variable-speed Control Moment Gyros, *Journal of Guidance, Control, and Dynamics*, **27**(2004), pp.374-386.

[21] Abbas, S. H., Ali, A., Hashemi, M. S., Werner, H.: LPV Gain-scheduled Control of a Control Moment Gyroscope, *2013 American Control Conference*, Washington, DC, USA, (2013), June 17-19.

[22] Sasaki, T., Sakuramata, N., Shimomura, T.: Attitude Control of a Spacecraft with a DGVSCMG via LPV Control Theory, *Journal of the Japan Society for Aeronautical and Space Sciences*, **63**(2015), pp.77-82 (in Japanese).

[23] Edo, K., Kanki, H., Kawanishi, M.: Active Jiggle Control for Hung Structure using Double Gimbals CMG, *Journal of the Japan Society of Mechanical Engineers Part (C)*, **66**(2000), pp.3289-3296 (in Japanese).

[24] Edo, K., Kanki, H., Kawanishi, M., Kagawa, R.: Dynamical Characteristics Analysis of Double Gimbal CMG and its Application to Vibration Control, *Journal of the Japan Society of Mechanical Engineers Part (C)*, **67**(2001), pp.110-117 (in Japanese).

[25] Sampei, M., Mita, T., and Nakamichi, M.: An Algebraic Approach to H_∞ Output Feedback Control Problems, *Systems & Control Letters*, **14**(1990), pp.13-24.

[26] Wei-Mi Lu., and Doyle, C. J.: H_∞ Control of Non-linear Systems: A Convex Characterization, *Proceedings of American Control Conference*, (1994), pp.2098-2012.

[27] van der Schaft, A. J.: L_2-gain and Passivity Techniques in Nonlinear Control, Springer-Verlag, (1996).

[28] Patpong, L., Sampei, M., Koga, M., Shimuzu, E.: A Numerical Computational Approach of Hamilton-Jacobi-Isaacs Equation in Nonlinear H_∞ Control Problems, *35th Conference on Decision and Control*, (1996), pp.3774-3779.

[29] Ohsaku S., Nakayama T., Kamimura I., Motozono, Y.: Nonlinear H_∞ State Feedback Controller for Semi-active Controlled Suspension, *Proceedings of AVEC '98*, (1998), pp.63-68.

[30] Steyn, W. H.: A Dual-wheel Multi-mode Spacecraft Actuator for Near-minimum-time Large Angle Slew Maneuvers, *Aerospace Science and Technology*, **12**(2008), pp.545-554.

[31] Kida, T., Yamaguchi, I., Ikeda, M.: LSS Attitude Control Experiment –Application of LQ Loop-shaping Capability –, *Society of Instrument and Control Engineers Journal*, **28**(1992), pp.107-115 (in Japanese).

[32] Wie, B.: Space Vehicle Dynamics and Control, 2nd edition, AIAA Education Series, American Institute of Aeronautics and Astronautics, Inc. (2008).

Chapter 5

Conclusions

This dissertation has described research on further increasing the performance of 4-SGCMG pyramid-array systems. To achieve this objective, steering unit mechanisms and methods for transition between control modes were proposed to meet the three key requirements of increased fault tolerance, higher torque, and vibration control, and their effectiveness was investigated.

Chapter 1 reviewed past advances in CMGs, noted the remaining problems, and described the objectives of the present study.

Chapter 2 described a method for increasing the fault tolerance of 4-SGCMG pyramid arrays, as illustrated by the problem of attitude control using a CMG system with only two of the four SGCMGs in its steering unit remaining operational. For attitude control by only two of four opposing SGCMGs in a pyramid array, direct output of torque can be performed about the x- and z-axes, but not about the y-axis. For three-axis attitude control, the problem is then to provide a means of attitude control about the y-axis. The proposed solution was to apply the corning effect induced by attitude maneuvers about the x- and z-axes to y-axis attitude control, together with a proposed gimbal steering control law to determine by spherical trigonometry the x- and z-axis attitude control angles that will induce the desired y-axis attitude control. It was verified by numerical simulations that the proposed gimbal steering control law enables effective three-axis control using just two of the SGCMGs in a 4-SGCMG pyramid-array system,

thus increasing the system's fault tolerance.

Chapter 3 described a proposed ASCCMG system incorporating variable-skew rather than fixed-skew gimbals to obtain a higher torque output and thereby attain the target attitude in the minimum time. The range of angles that can be obtained by a variable skew angle mechanism is inherently limited, and a gimbal steering control law that disregards this limit would tend to result in mismatches between the command torque and the generated torque and thus cause the angle of the spacecraft to overshoot the target state. The range of attainable skew angles was therefore considered, and a method was proposed for obtaining smooth contact between the steering control laws for ASCMG operation and classical fixed-angle gimbal operation by varying the weight gain in accordance with the current skew angle, to shorten the settling time while also eliminating overshoot. Numerical simulations showed that the proposed gimbal steering control law shortened the settling time by approximately 10% from that with the classical fixed-skew angle CMG alone, minimized attitude disturbance, and on completion of the attitude maneuver tended to return the skew angle to its former value. The results thus indicate that the proposed gimbal steering control law yields a further increase in high torque output which enables target-state attainment in the minimum time using a pyramid -arrayed 4-SGCMG.

Chapter 4 describes the proposed utilization of VSCMGs to change the steering unit from a fixed-speed flywheel unit to a variable-speed flywheel unit, for control of flexible-body vibration. The increased torque output of the 4-SGCMG pyramid-array unit described in Chapter 3 will make it capable of effective attitude control for large spacecraft, but increasing spacecraft size also increases the tendency for excitement of vibration of flexible components. For utilization of CMGs in attitude control of large flexible spacecraft, it is therefore necessary to control the level of vibrational excitation. With this objective, Chapter 4 proposed a transformation of the four pyramid-array SGCMGs to VSCMGs by gain weighting them in accordance with the distance to the target state, together with a gimbal steering control law that places the VSCMGs in a high output-torque CMG mode when distant from the target state and a low output-

torque CMG mode when near the target state. In addition, H_∞ control theory was applied to consider uncertainty in variations of the wheel speed in the VSCMGs and vibration modes of flexible structures, and an LMI-based controller was designed to provide the VSCMGs with a command torque to meet the requirements of robustness against this uncertainty, and increase their performance in converging to the target state. Numerical simulations showed that the proposed steering control law effectively selects the CMG mode or the RW mode in accordance with the distance to the target state, with high performance in both target-state convergence and vibration control. The results thus indicate that the proposed steering control law for a pyramid-arrayed 4-SGCMG incorporating VSCMG functionality provides the vibration control required for large flexible structures in space during attitude maneuvers.

The steering-mode variation control method proposed in this dissertation for a 4-SGCMG pyramid-array system can thus achieve increased fault tolerance together with higher torque and increased vibration control.

With the advances described in this dissertation, the 4-SGCMG pyramid-array system is expected to be a superior system for attitude control of large satellites and thus make a major contribution to the progress of mankind in space exploration and development.

Achievement

The results and outcomes of the research presented within this dissertation have been published in the peer-reviewed journals, and proceedings. Those publications are listed below.

Peer-reviewed papers related with this dissertation

1) Kasai, S., Kojima, H., and Satoh, M.: Spacecraft Attitude Maneuver using Two Single-Gimbal Control Moment Gyros, *Elsevier Acta Astronautica*, **84**(2013), pp.88-98.

2) Kasai, S. and Kojima, H.: Gain-Scheduled Steering Control Law for Adaptive Skew Pyramid-Type CMGs, *Journal of The Japan Society for Aeronautical and Space Sciences*, **62**(2014), pp.55-62 (in Japanese).

3) Kasai, S. and Kojima, H.: LMI-based Control Law for Variable-Speed Control Moment Gyros in Flexible Spacecraft, *International Journal of Space Science and Engineering*, **3**(2015), pp.246-278.

Proceedings papers

1) Kasai, S., Kojima, H. and Satoh, M.: Spacecraft Attitude Maneuver using Two Single-gimbal Control Moment Gyros, AIAA/AAS Astrodynamics Specialist Conference, Minneapolis, August 13-16, 2012.

2) Kojima, H., and Kasai, S.: Gain-scheduled Steering Control Law for Adaptive Skew Pyramid-type CMGs, 15th Australian International Aerospace Congress, Melbourne, February 25- 28, 2013.

3) Kasai, S., Kojima, H., Sakai, M. and Satoh, M.: Gain-scheduled Steering Control Law of Variable Speed CMG for Spacecraft Attitude Maneuver, 29th International Symposium on Space Technology and Science, Nagoya, June 2-9, 2013.

4) Kasai, S. and Kojima, H.: Gain-scheduled Steering Control Law for Variable Speed Control Moment Gyros, AIAA Guidance, Navigation, and Control Conference, Boston, August 18-21, 2013.

5) Kasai, S. and Kojima, H.: Linear Matrix Inequality-based Steering Control Law of Variable Speed Control Moment Gyros for Flexible Spacecraft, 16th Australian International Aerospace Congress, Melbourne, February 23-26, 2015.

Acknowledgements

I would like to express my gratitude to the supervisor, Professor Kojima, Tokyo Metropolitan University for his helpful and exact comments on this dissertation.

Suggestions and comments provided from Professor Takegahara, Professor Masuda, Tokyo Metropolitan Univerisity, and Professor Shimomura, Osaka Prefecture University, are much appreciated.

I am sincerely grateful to my parents because they have provided me with courage towards finalizing this dissertation.